

## Supporting Information

### Isolation and Oxygen Activation of Electron-Rich Co<sub>4</sub>O Metallic Clusters Having a 3-Fold Symmetry

Maria Francis,<sup>a</sup> Asutosh Patra,<sup>a</sup> Farsana Abdul Salam,<sup>a</sup> Liviu Ungur,<sup>b</sup> Björn Schwarz,<sup>\*c</sup> and Sudipta Roy<sup>\*a</sup>

### Contents:

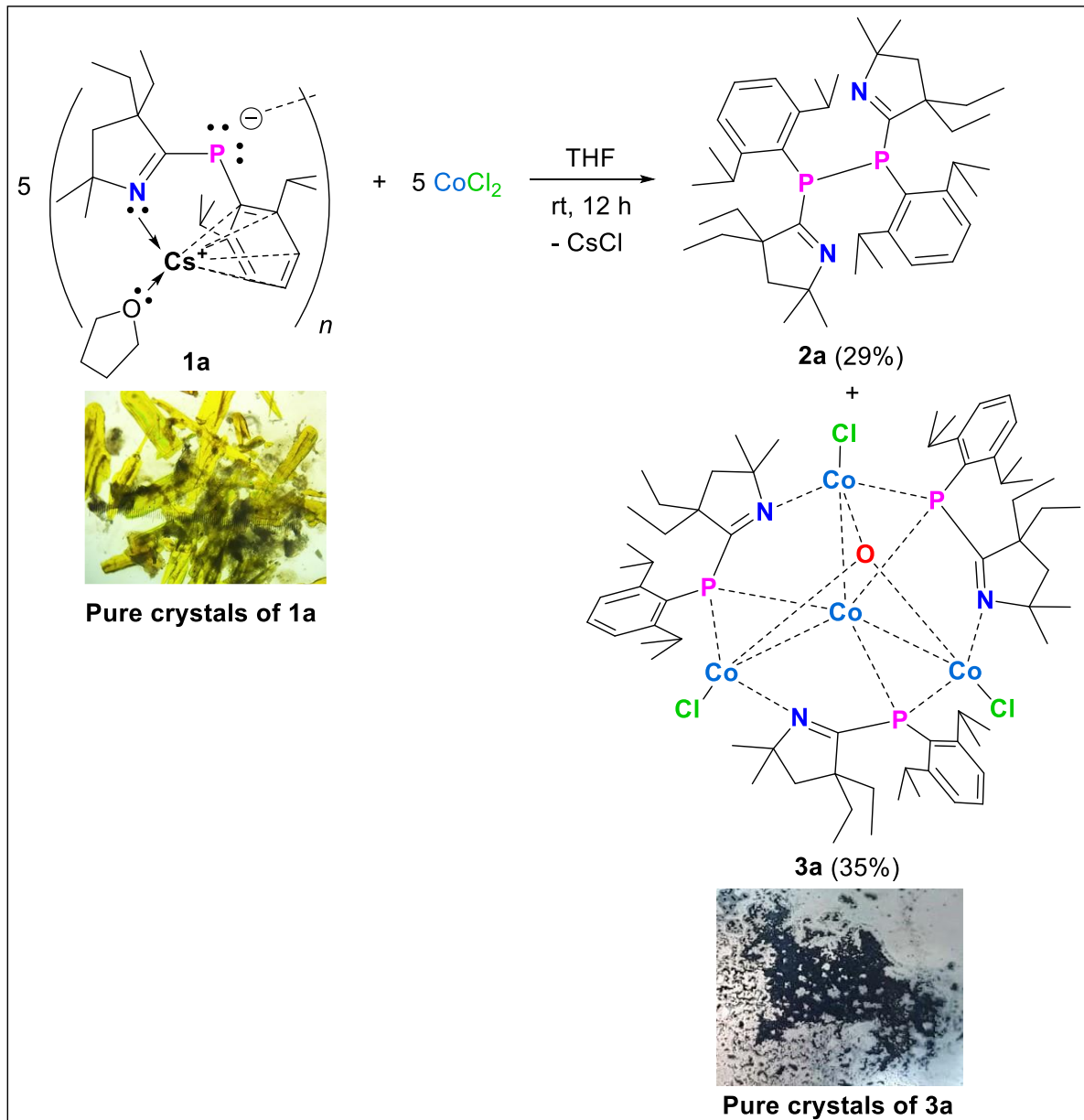
<b>S1.</b> General remarks.....	S2
<b>S2.</b> Detailed Syntheses and characterizations.....	S3-S18
<b>S3.</b> Cyclic voltammetry studies .....	S19-S20
<b>S4.</b> X-ray crystallographic data of compounds <b>2a-2b</b> , complexes <b>3a, 4a-4b</b> ...	S20-S49
<b>S5.</b> Details of magnetic measurements.....	S49-S55
<b>S6</b> Computational studies, and Hirshfeld plots.....	S55-S92
<b>S7.</b> XPS data.....	S92-S93
<b>S8.</b> Spectral data.....	S94-S95
<b>S9.</b> References.....	S96-S97

## S1. General remarks

All manipulations were performed using either standard Schlenk line techniques under inert argon atmosphere or in an argon-filled MBraun Eco Plus glove box, where O<sub>2</sub> and H<sub>2</sub>O levels were always kept below 0.1 ppm. All glassware were oven-dried (150 °C) prior to use. Solvents obtained from an MBraun Solvent Purification System (SPS) were further dried by standard methods of refluxing with Na/K alloy for two days, followed by vacuum distillation over 4 Å molecular sieves under argon. Cyclic alkyl(amino) carbene (cAAC) salts,<sup>1</sup> free cAACs,<sup>1</sup> cAAC=P-Cl,<sup>2</sup> [((Dipp)(Et<sub>2</sub>-cAl)P)<sub>2</sub>Cs<sub>2</sub>(THF)<sub>4</sub>]<sub>n</sub><sup>3</sup> were synthesized according to the literature reported procedures. <sup>1</sup>H, <sup>13</sup>C {<sup>1</sup>H}, and <sup>31</sup>P NMR spectra were recorded on Bruker Neo Avance 400 MHz, spectrometer (<sup>13</sup>C {<sup>1</sup>H} NMR spectrum denotes the respective <sup>13</sup>C NMR spectrum with <sup>1</sup>H decoupling). The chemical shift values were reported in δ (ppm) relative to C<sub>6</sub>D<sub>6</sub> at 7.26 ppm (<sup>1</sup>H NMR) and 128.0 ppm (<sup>13</sup>C {<sup>1</sup>H} NMR). The heteronuclear NMR spectra are referenced to the external standards (<sup>31</sup>P NMR: 85% H<sub>3</sub>PO<sub>4</sub>). The following abbreviations were used to describe the peak multiplicity in <sup>1</sup>H NMR spectra: s (singlet), brs (broad singlet), d (doublet), dd (doublet of doublet), td (triplet of doublet), t (triplet), q (quartet), m (multiplet). Melting points were measured in sealed glass tubes on a Digital Stuart Melting Point Apparatus. Direct current (DC) magnetization was measured with a Physical Property Measurement System (PPMS) DynaCool from Quantum Design equipped with a vibrating sample magnetometry (VSM) option. Alternating current (AC) susceptibility was measured with an ACMS-II option (from Quantum Design) from 10 Hz to 10 kHz at 35 frequencies with log-distribution at 2 K at zero field and at 500 Oe DC field. Single crystal X-Ray diffraction data were collected on a Bruker D8 venture Apex4 HEED diffractometer, with helios optics monochromated Mo-Kα (λ = 0.71073 Å) radiation at 100 K. Elemental analyses were performed on a Thermo scientific flash 2000 elemental analyzer. The data was integrated using SAINT PLUS and absorption correction was done using multi-scan absorption correction method (SADABS).

## S2. Detailed syntheses

### S2.1. Syntheses and isolation $[((\text{Dipp})(\text{Et}_2\text{-cAl})\text{P}(\text{CoCl}))_3\text{CoO}]$ (**3a**)



**Scheme S1.** Synthesis of  $[((\text{Dipp})(\text{Et}_2\text{-cAl})\text{P}(\text{CoCl}))_3\text{CoO}]$  (**3a**).

In an oven-dried Schlenk flask,  $[(\text{Dipp})(\text{Et}_2\text{-cAl})\text{P}(\text{CoCl})]_2\text{Cs}_2(\text{THF})_4$  (**1a**) (100 mg, 0.173 mmol, 1 equiv) and anhydrous  $\text{CoCl}_2$  (45 mg, 0.346 mmol, 2 equiv) were taken. Added freshly distilled THF (15 mL) at room temperature (rt) to obtain a clear dark greenish-blue solution, which was stirred overnight to obtain the black precipitate. The reaction mixture was then filtered using a frit to obtain the dark blueish-black filtrate, which was completely dried under reduced pressure, and further dissolved in anhydrous DCM.

The DCM solution was concentrated up to 3-4 mL, and kept at -40 °C in a freezer for crystallization. The colorless needles of **2a** suitable for X-ray single-crystal diffraction were formed after 4-5 days. Afterwards, the dark bluish-black mother liquor was transferred through a canula to another Schlenk flask, and kept for crystallization at -40 °C in a freezer. The dark bluish-black hexagonal crystals of complex **3a**, suitable for X-ray single-crystal diffraction were formed after 1-2 weeks in 35% isolated yield (17 mg).

**Elemental analysis for C<sub>66</sub>H<sub>105</sub>Cl<sub>3</sub>Co<sub>4</sub>N<sub>3</sub>OP<sub>3</sub> (3a):** Observed in % (Cald. in %): C: 56.83 (56.97); H: 7.58 (7.61); N, 2.94 (3.02). **MP:** 209-210 °C.

The colorless needles of compound **2a** suitable for X-ray single-crystal diffraction were formed after 2-3 days in 29% of isolated yield (7 mg). Afterwards, the dark bluish-black mother liquor was transferred through a canula to another Schlenk flask, and kept for crystallization at -40 °C in a freezer. The dark bluish-black hexagonal crystals of complex **3a**, suitable for X-ray single-crystal diffraction were formed after 1-2 weeks.

**Purification of 2a and 3a:** The compound **2a** and the complex **3a** are isolated in the pure crystalline form by using the fractional crystallization method. The solubility of **2a** in THF is much lower than that of **3a**. Therefore, first **2a** starts crystallizing (within 2-3 days) from the concentrated DCM solution kept at -40 °C from a freezer. Upon isolation of the pure crystals of **2a**, the concentrated DCM solution was kept back at -40 °C in a freezer, from which the bluish-black crystals of **3a** were obtained in the pure form after 1-2 weeks.

## S2.2. NMR spectroscopic analyses of bis-(aryl)(imino)-phosphene (2a)

**<sup>1</sup>H NMR** (400 MHz, 298K, C<sub>6</sub>D<sub>6</sub>) δ: 7.26-7.19 (m, 3H, -ArH), 7.13-7.07 (m, 3H, -ArH), 4.96 (m, 2H, -CH(CH<sub>3</sub>)<sub>2</sub>), 4.82 (br, 2H, -CH(CH<sub>3</sub>)<sub>2</sub>), 1.75 (d, J = 6.8 Hz, 6H, -C(CH<sub>3</sub>)<sub>2</sub>)), 1.61 (d, J = 6.8 Hz, 6H, -C(CH<sub>3</sub>)<sub>2</sub>)), 1.48 (d, J = 7.0 Hz, 6H, -(CH<sub>3</sub>)<sub>2</sub>)), 1.43-1.39 (m, 4H, -CH<sub>2</sub>), 1.32 (s, 6H, -(CH<sub>3</sub>)<sub>2</sub>)), 1.29-1.23 (m, 12H, -(CH<sub>3</sub>)<sub>2</sub>)), 1.08 (q, J = 7.4 Hz, 4H, -CH<sub>2</sub>), 0.81 (s, 4H, -CH<sub>2</sub>), 0.76 (t, J = 7.6 Hz, 6H, -(CH<sub>3</sub>)<sub>2</sub>)), 0.51 (t, J = 7.5 Hz, 6H, -(CH<sub>3</sub>)<sub>2</sub>)) ppm; **<sup>31</sup>P NMR** (162 MHz, 298K, C<sub>6</sub>D<sub>6</sub>) δ: -35.4 ppm. **Elemental analysis for C<sub>44</sub>H<sub>70</sub>N<sub>2</sub>P<sub>2</sub> (2a):** Observed in % (Cald. in %): C: 76.63 (76.70); H: 9.18 (10.24); N: 3.96 (4.07). **MP:** 180-181 °C.

### S2.3. Electron Paramagnetic Resonance (EPR) study of $[(\text{Dipp})(\text{Et}_2\text{-cAl})\text{PO}_2(\text{CoCl})_2]$ (**3a**) in DCM at 77 K

**3a** was found to be EPR active. The EPR spectrum of a diluted DCM solution of complex **3a** at X-band (8.75-9.65 GHz) was recorded using a JEOL Model JES FA200 EPR spectrometer at 77 K, which exhibited a very broad signal. The sample preparation was done under argon atmosphere using a standard glove box technique.

**X-band EPR spectrum of  $[(\text{Dipp})(\text{Et}_2\text{-cAl})\text{P}(\text{CoCl})_3\text{CoO}]$  (**3a**) in DCM at 77 K**

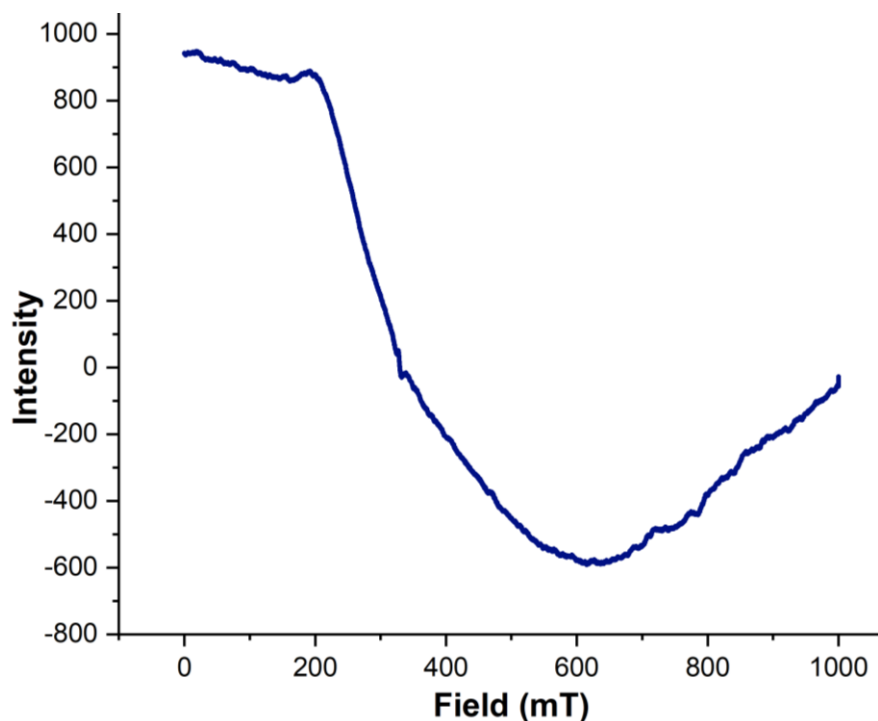


**Figure S1.** X-band EPR spectrum of complex  $[(\text{Dipp})(\text{Et}_2\text{-cAl})\text{P}(\text{CoCl})_3\text{CoO}]$  (**3a**) in DCM at 77 K.

**S2.4. IR Spectrum of  $\text{[((Dipp)(Et}_2\text{-cAl)}\text{P}(\text{CoCl})_3\text{CaO}]$  (3a)**

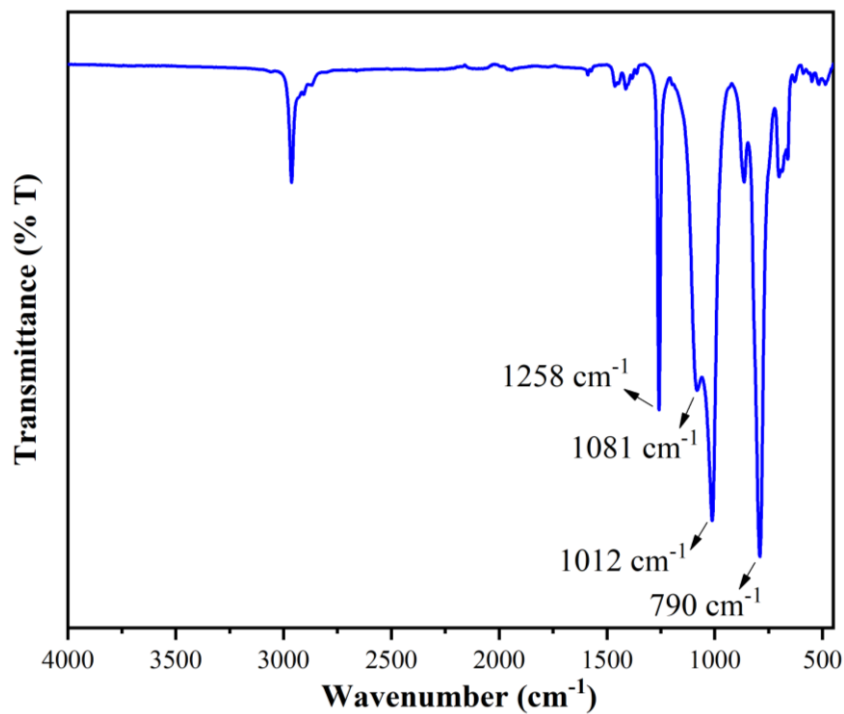


**Figure S2.** IR spectrum of complex  $\text{[((Dipp)(Et}_2\text{-cAl)}\text{P}(\text{CoCl})_3\text{CoO}]$  (3a).

**S2.5. UV-vis absorption spectrum of complex  $\text{[((Dipp)(Et}_2\text{-cAl)}\text{P}(\text{CoCl})_3\text{CoO}]$  (3a)**

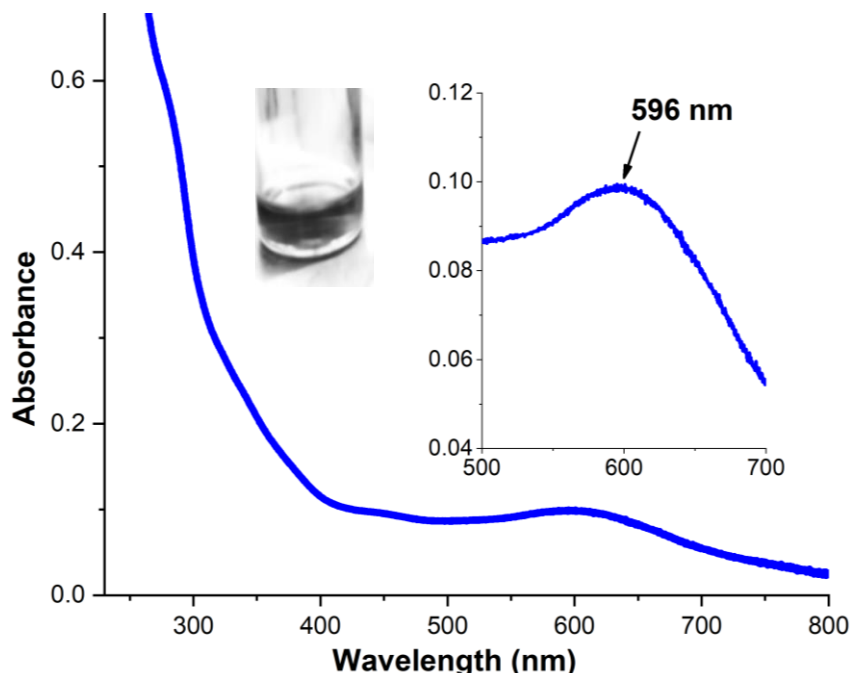


**Figure S3.** UV-vis absorption spectrum of complex  $\text{[((Dipp)(Et}_2\text{-cAl)}\text{P}(\text{CoCl})_3\text{CoO}]$  (3a) in DCM solution at rt.

### Molar Extinction Coefficient ( $\epsilon$ ) of 3a

For the peak at 308 nm:

$$A = \epsilon * c * l$$
$$0.530 = \epsilon * 0.109 * 10^{-3} M * 1 cm$$
$$\epsilon = 4862.38 M^{-1} cm^{-1}$$

For the peak at 596 nm:

$$A = \epsilon * c * l$$
$$0.025 = \epsilon * 0.109 * 10^{-3} M * 1 cm$$
$$\epsilon = 229.35 M^{-1} cm^{-1}$$

**Sample preparation:** The stock solution of  $[(\text{Dipp})(\text{Et}_2\text{-cAl})\text{P}(\text{CoCl})_3\text{CoO}]$  (**3a**) in 1.092 mM concentration was prepared in dry THF, and 200  $\mu\text{L}$  of the stock solution was added to a UV-cuvette and further diluted to 2 mL by adding dry THF. The UV-Vis spectrum was recorded for the 109  $\mu\text{M}$  solution and corresponding  $\lambda_{\max}$  was observed at 308 nm with a shoulder at 598 nm.

$$\text{Concentration} = \frac{\text{Weight taken} * 1000}{\text{Mol. Wt.} * \text{Vol. of solution}}$$
$$= \frac{7.8 \text{ mg} * 1000}{1427.62 \text{ gmol}^{-1} * 5 \text{ mL}}$$
$$\text{Concentration} = 1.092 \text{ mM}$$

It was further diluted using the following equation

$$M_1 V_1 = M_2 V_2$$
$$1.092 \text{ mM} * V_1 = 0.109 \text{ mM} * 2 \text{ mL}$$
$$V_1 = 0.2 \text{ mL}$$

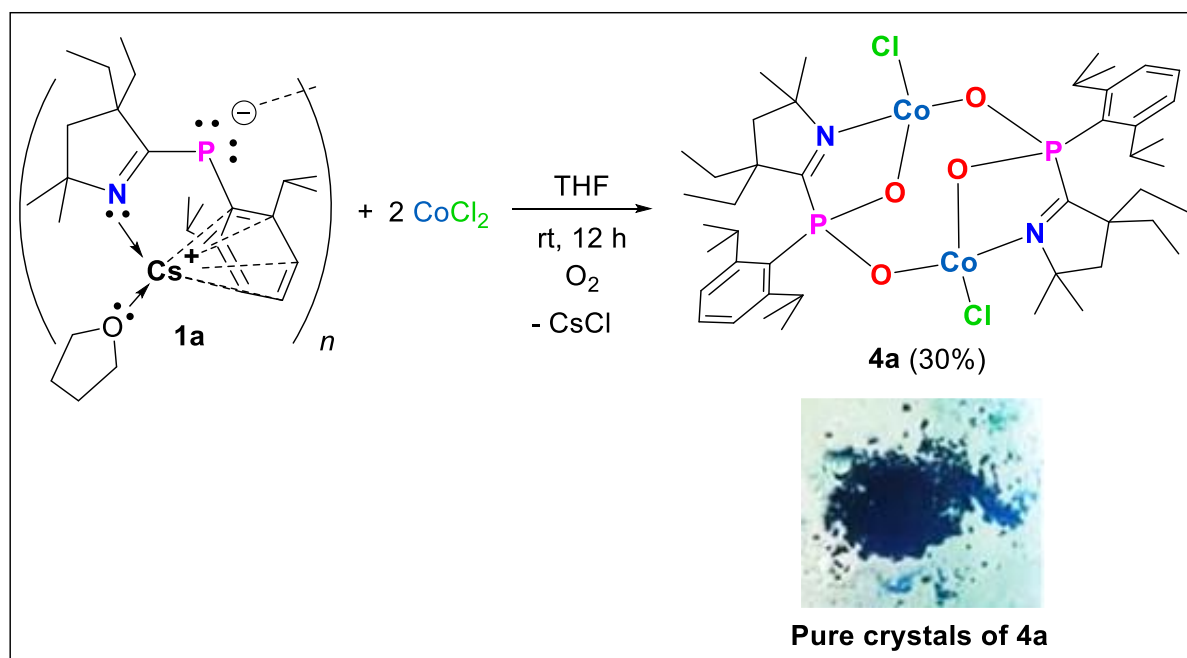
where,  $M_1$  = Concentration of the stock solution

$V_1$  = Vol. of stock solution required for making the diluted solution of 0.109 mM

$M_2$  = Concentration of the diluted solution

$V_2$  = Final volume

## S2.6. Synthesis and isolation of $\left[\text{((Dipp)(Et}_2\text{-cAl})\text{PO}_2\text{(Co}^{\text{II}}\text{Cl})\right)_2$ (4a)



**Scheme S2.** Synthesis of complex  $\left[\text{((Dipp)(Et}_2\text{-cAl})\text{PO}_2\text{(Co}^{\text{II}}\text{Cl})\right)_2$  (4a).

In an oven-dried Schlenk flask,  $\left[\text{((Dipp)(Et}_2\text{-cAl})\text{P)}_2\text{Cs}_2(\text{THF})_4\right]_n$  (**1a**) (100 mg, 0.173 mmol, 1 equiv) and anhydrous  $\text{CoCl}_2$  (45 mg, 0.346 mmol, 2 equiv) were taken. Added freshly distilled THF (15 mL) at rt to obtain a clear dark greenish-blue solution and stirred overnight. The black precipitate formed was filtered using a frit to obtain the dark blueish-black filtrate. The filtrate was then exposed to air for 5-10 min (until the color turns to dark blue), and then concentrated under reduced pressure to 2-3 mL, stored at -40 °C in a freezer. The dark blue block-shaped crystals of complex  $\left[\text{((Dipp)(Et}_2\text{-cAl})\text{PO}_2\text{(Co}^{\text{II}}\text{Cl})\right)_2$  (**4a**) suitable for single crystal X-ray diffraction were obtained after 2-3 days in 30% isolated yield (24 mg). **Elemental analysis for  $\text{C}_{44}\text{H}_{70}\text{Cl}_2\text{Co}_2\text{N}_2\text{O}_4\text{P}_2$  (4a):** Observed in % (Cald. in %): C: 55.61 (56.12); H: 7.18 (7.49); N, 2.79 (2.97). **MP:** 194-196 °C.

## S2.7. Electron Paramagnetic Resonance (EPR) study of $\left[\text{((Dipp)(Et}_2\text{-cAl})\text{PO}_2\text{(Co}^{\text{II}}\text{Cl})\right)_2$ (4a) in DCM at 298 K

Complex **4a** was found to be EPR active. The EPR spectrum of a diluted DCM solution of complex **4a** at X-band (8.75-9.65 GHz) was recorded using a JEOL Model JES FA200 EPR spectrometer at 298 K, which exhibited a characteristic signal. The

sample preparation was done under argon atmosphere using a standard glove box technique.

### **EPR spectrum of [(Dipp)(Et<sub>2</sub>-cAl)PO<sub>2</sub>(CoCl)<sub>2</sub>] (4a) in DCM at 298 K**

**EPR sample preparation:** The pure blue crystals of the [(Dipp)(Et<sub>2</sub>-cAl)PO<sub>2</sub>(Co<sup>II</sup>Cl)<sub>2</sub>] (**4a**) was dissolved in distilled THF under an argon atmosphere, and transferred to an oven dried quartz capillary, which was then sealed adequately using silicon grease and melted wax to maintain the argon atmosphere.

#### **Calculation of Lande factor (g):**

$$g = \frac{h\nu}{\mu_B H}$$

where,

$h$  = Planck's constant,

$\nu$  = Operating frequency

$\mu_B$  = Bohr magneton

$H$  = Magnetic field

$g$  = Lande factor

$$h = 6.626 \times 10^{-34} \text{ JS}$$

$$\nu = 9167.258 \text{ MHz} = 9436.369 \times 10^6 \text{ Hz}$$

$$\mu_B = \text{Bohr's magneton} = 9.2740 \times 10^{-24} \text{ JT}^{-1}$$

$$H = \text{magnetic field} = \text{data on x-axis in mT} = 326.6063 \text{ mT} = 326.6063 \times 10^3 \text{ T}$$

$$g = \frac{6.626 \times 10^{-34} \text{ JS} \times 9167.258 \times 10^6 \text{ S}^{-1}}{9.2740 \times 10^{-24} \text{ JT}^{-1} \times 326.6063 \times 10^{-3} \text{ T}}$$

$$g = 2.0053$$

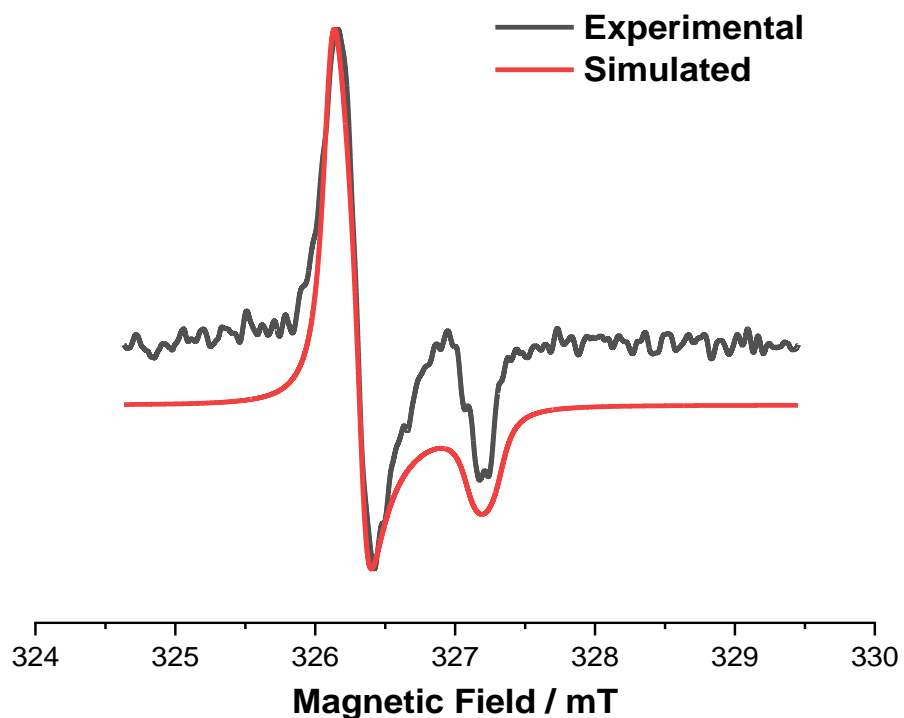


**Figure S4.** X-band EPR spectrum of complex  $[(\text{Dipp})(\text{Et}_2\text{-cAl})\text{PO}_2(\text{Co}^{\text{II}}\text{Cl})_2]$  (**4a**) in DCM at 298 K. Red and black lines represent the simulated and the experimental spectra, respectively for **4a** using the EasySpin program. [ $\mathbf{g}_{\parallel} = 2.00797$ ,  $\mathbf{g}_{\perp} = 2.00192$ , LWPP (Gaussian broadening) = 0.0143971 mT, LWPP (Lorentzian broadening) = 0.0926287 mT,  $\mathbf{A}(\text{Co}) = 0.850778$  MHz, X-band experimental frequency = 9.168133 GHz].

$$g_{iso} = \sqrt{\frac{2g_{\perp}^2 + g_{\parallel}^2}{3}} = \sqrt{\frac{2 \times 2.00192^2 + 2.00797^2}{3}} = 2.003938696$$

This X-band EPR spectrum appears axial with  $g_x = g_y > g_z$ . Here  $g_x = g_y = \mathbf{g}_{\parallel} = 2.00797$  and the  $g_z = \mathbf{g}_{\perp} = 2.00192$ . The modelling assumes all cobalt centres in the low spin +1 oxidation state, giving rise to one unpaired electron in each cobalt centre.

**S2.8. IR Spectrum of  $\text{[((Dipp)(Et}_2\text{-cAl)}\text{PO}_2\text{(Co}^{\text{II}}\text{Cl)})_2]$  (4a)}**

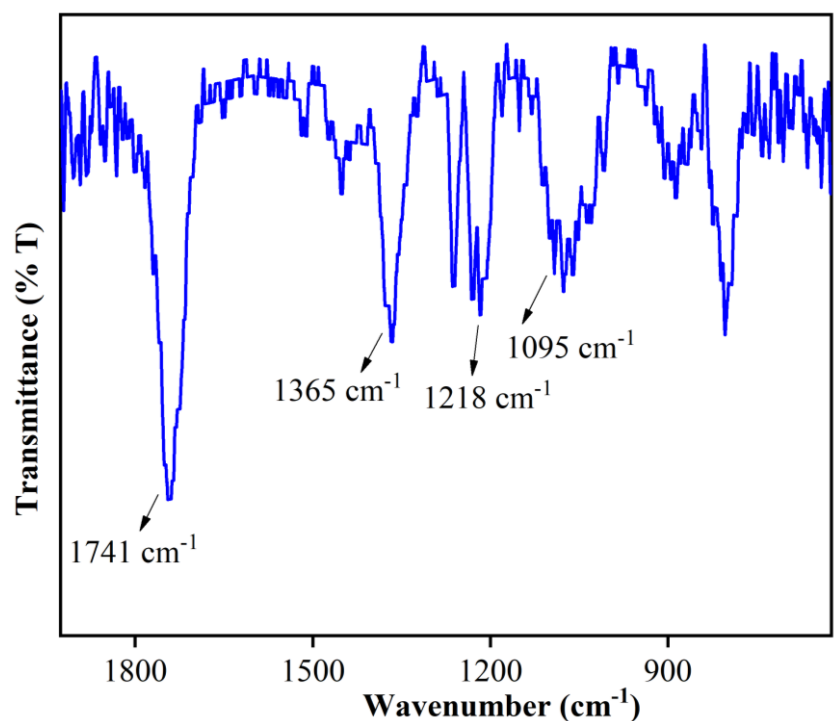


**Figure S5.** IR spectrum of  $\text{[((Dipp)(Et}_2\text{-cAl)}\text{PO}_2\text{(Co}^{\text{II}}\text{Cl)})_2]$  (4a).

**S2.9. UV-vis absorption spectrum of  $\text{[((Dipp)(Et}_2\text{-cAl)}\text{PO}_2\text{(Co}^{\text{II}}\text{Cl)})_2]$  (4a)**

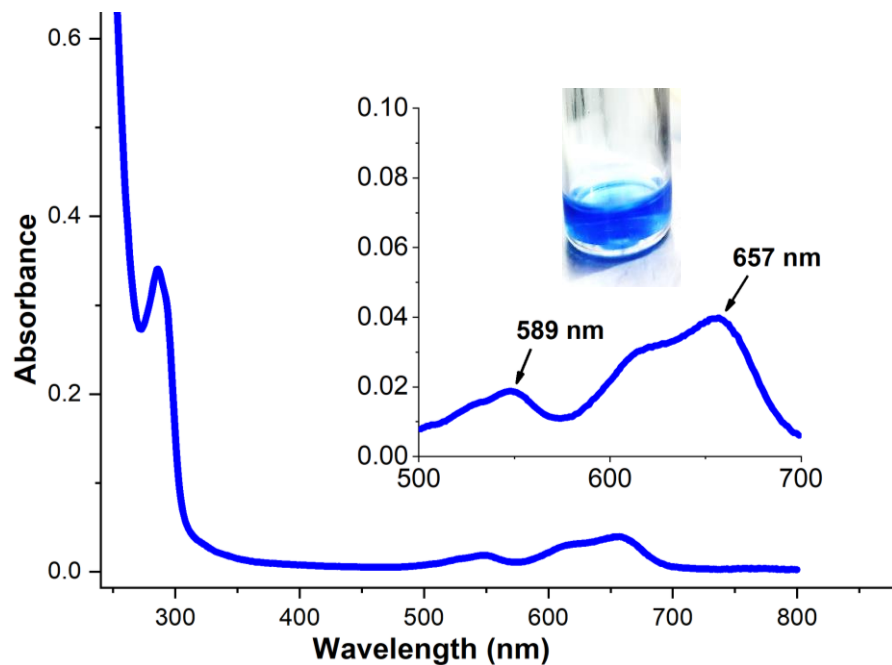


**Figure S6.** UV-vis absorption spectrum of  $\text{[((Dipp)(Et}_2\text{-cAl)}\text{PO}_2\text{(Co}^{\text{II}}\text{Cl)})_2]$  (4a) in DCM solution at rt.

### Molar Extinction Coefficient ( $\epsilon$ ) of 4a

For the peak at 284 nm:

$$\begin{aligned}A &= \epsilon * c * l \\0.348 &= \epsilon * 0.106 * 10^{-3} M * 1 cm \\\epsilon &= 3283.01 M^{-1} cm^{-1}\end{aligned}$$

For the peak at 546 nm:

$$\begin{aligned}A &= \epsilon * c * l \\0.012 &= \epsilon * 0.106 * 10^{-3} M * 1 cm \\\epsilon &= 113.20 M^{-1} cm^{-1}\end{aligned}$$

For the peak at 662 nm:

$$\begin{aligned}A &= \epsilon * c * l \\0.029 &= \epsilon * 0.106 * 10^{-3} M * 1 cm \\\epsilon &= 273.58 M^{-1} cm^{-1}\end{aligned}$$

**Sample preparation:** The stock solution of  $[(\text{Dipp})(\text{Et}_2\text{-cAl})\text{PO}_2(\text{Co}^{\text{II}}\text{Cl})_2]$  (**4a**) in 0.531 mM concentration was prepared in dry THF, and 399  $\mu\text{L}$  of the stock solution was added to a UV-cuvette and further diluted to 2 mL by adding dry THF. The UV-vis spectrum was recorded for the 106  $\mu\text{M}$  solution and corresponding  $\lambda_{\text{max}}$  was observed at 284, 546, and 662 nm.

$$\begin{aligned}\text{Concentration} &= \frac{\text{Weight taken} * 1000}{\text{Mol. Wt.} * \text{Vol. of solution}} \\&= \frac{0.5 \text{ mg} * 1000}{941.77 \text{ gmol}^{-1} * 1 \text{ mL}} \\ \text{Concentration} &= 0.531 \text{ mM}\end{aligned}$$

It was further diluted using the following equation

$$\begin{aligned}M_1 V_1 &= M_2 V_2 \\0.531 \text{ mM} * V_1 &= 0.106 \text{ mM} * 2 \text{ mL} \\V_1 &= 0.399 \text{ mL}\end{aligned}$$

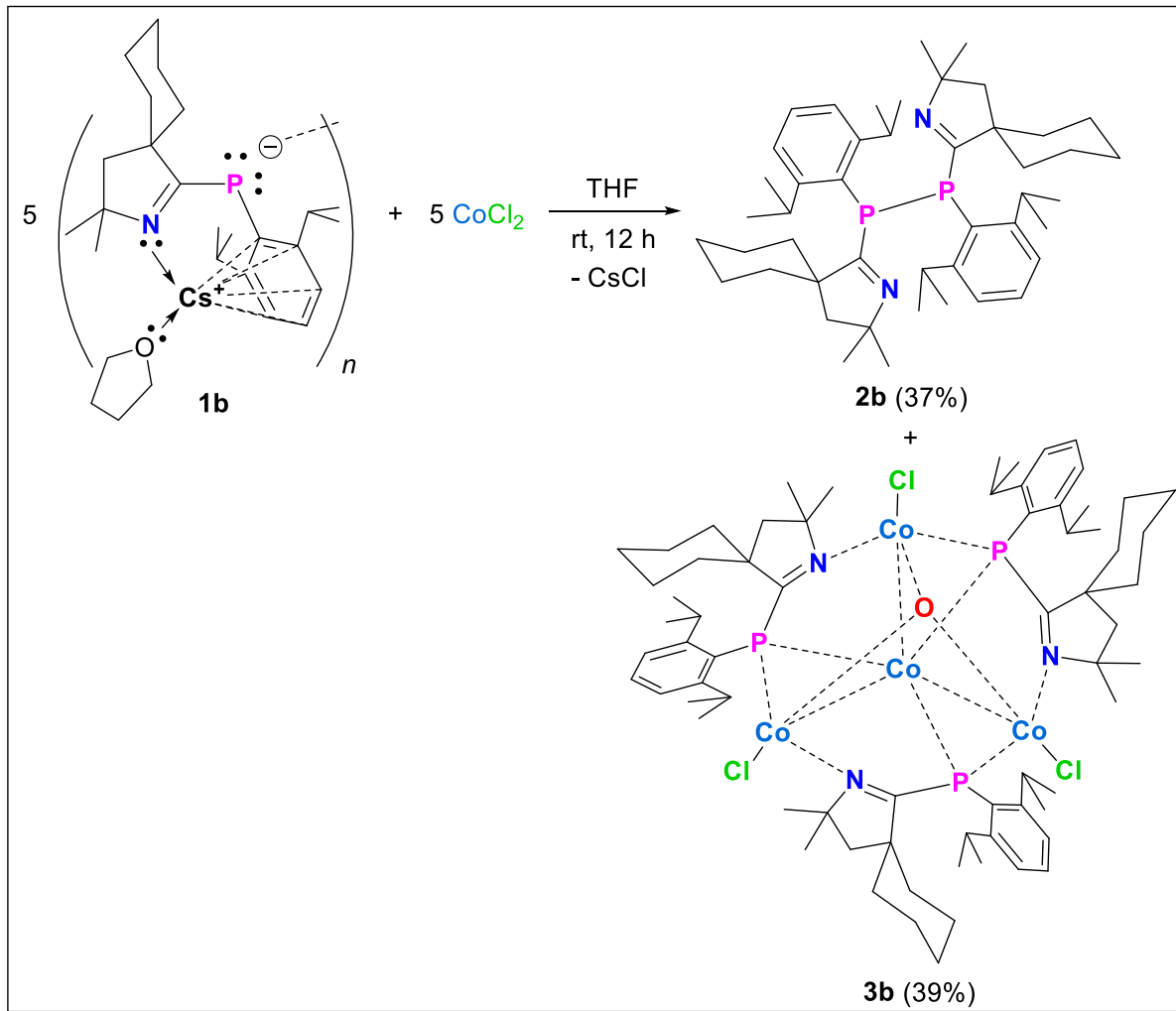
where,  $M_1$  = Concentration of the stock solution

$V_1$  = Vol. of stock solution required for making the diluted solution of 0.109 mM

$M_2$  = Concentration of the diluted solution

$V_2$  = Final volume

### S2.10. Synthesis of $[(\text{Dipp})(\text{Cy-cAl})\text{P}(\text{CoCl})_3\text{CoO}]$ (**3b**)



**Scheme S3.** Synthesis of  $[(\text{Dipp})(\text{Cy-cAl})\text{P}(\text{CoCl})_3\text{CoO}]$  (**3b**).

In an oven-dried Schlenk flask,  $[(\text{Dipp})(\text{Cy-cAl})\text{P}_2\text{Cs}_2(\text{THF})_4]_n$  (**1b**) (100 mg, 0.17 mmol, 1 equiv) and anhydrous  $\text{CoCl}_2$  (44 mg, 0.34 mmol, 2 equiv) were taken. Added freshly distilled THF (15 mL) at rt to obtain a clear dark greenish-blue solution, which was then stirred overnight. The black precipitate formed was filtered using a frit to obtain the blueish-black color filtrate, which was completely dried under reduced pressure and further extracted in anhydrous DCM. The DCM solution was

concentrated up to 3-4 mL, and kept at -40 °C in a freezer for fractional crystallization to obtain **2b** and **3b** in pure crystalline form.

**Elemental analysis for C<sub>69</sub>H<sub>105</sub>Cl<sub>3</sub>Co<sub>4</sub>N<sub>3</sub>OP<sub>3</sub> (3b):** Observed in % (Cald. in %): C: 57.96 (58.05); H: 7.38 (7.41); N, 2.87 (2.94). **MP:** 211-212 °C.

The DCM solution was concentrated up to 3-4 mL, and kept at -40 °C in a freezer for fractional crystallization to obtain **2b** and **3b** in pure crystalline form.

**Crystallization of 2b:** The concentrated DCM solution kept at -40 °C in a freezer afforded the colorless needles of compound **2b** suitable for X-ray single-crystal diffraction after 2-3 days. After the dark bluish-black mother liquor was transferred through a canula to another Schlenk flask; the colorless crystals of **2b** were given a quick *n*-hexane wash, and dried under reduced pressure to obtain the pure crystals of **2b** in 37% isolated yield (9 mg).

**Crystallization of 3b:** The concentrated DCM solution obtained after separating the crystals of **2b** was kept back for crystallization at -40 °C in a freezer. The dark bluish-black crystals of complex **3b** were formed after 4 weeks in 39% of the isolated yield (19 mg). However, after several attempts none of the batches of the crystals of **3b** were diffracted, and therefore the single-crystal X-ray data of **3b** could not be collected.

**Purification of 2b and 3b:** Compound **2b** and complex **3a** are isolated in the pure crystalline form by fractional crystallization. The solubility of **2b** in THF is found to be much lower than that of **3b**. As a result, **2b** starts crystallizing first (2-3 days) from the concentrated DCM solution kept at -40 °C from a freezer. Upon isolation of the pure crystals of **2b**, the concentrated DCM solution was kept back at -40 °C in a freezer, from which the bluish-black crystals of **3b** were obtained in the pure form after 4 weeks.

## S2.11. NMR spectroscopic analyses of 2b

**<sup>1</sup>H NMR** (400 MHz, 298K, CD<sub>2</sub>Cl<sub>2</sub>) δ: 7.24-7.15 (m, 4H, -ArH), 7.00 (br, 2H, -ArH), 4.72 (br, 2H, -CH(CH<sub>3</sub>)<sub>2</sub>), 4.59 (br, 2H, -CH(CH<sub>3</sub>)<sub>2</sub>), 2.04 (s, 2H, -CH<sub>2</sub>), 1.79 (s, 2H, -CH<sub>2</sub>), 1.56 (s, 6H, -(CH<sub>3</sub>)<sub>2</sub>), 1.41 (s, 6H, -(CH<sub>3</sub>)<sub>2</sub>), 1.27-1.21 (br, 18H, -CH<sub>2</sub>), 1.05 (br, 12H, -CH(CH<sub>3</sub>)<sub>2</sub>), 0.84 (br, 8H, -CH<sub>2</sub>, -CH(CH<sub>3</sub>)<sub>2</sub>), 0.57 (br, 6H, -CH(CH<sub>3</sub>)<sub>2</sub>) ppm; **<sup>31</sup>P NMR**

(162 MHz, 298K, CD<sub>2</sub>Cl<sub>2</sub>) δ: -36.51 ppm; <sup>13</sup>C NMR (101 MHz, 298K, CD<sub>2</sub>Cl<sub>2</sub>) δ: 225.44, 181.1, 179.4, 140.7, 124.4, 47.8, 36.5, 33.6, 30.7, 30.0, 25.9, 25.8, 25.4, 24.9, 23.8, 23.7 ppm; **Elemental analysis for C<sub>46</sub>H<sub>70</sub>N<sub>2</sub>P<sub>2</sub> (2b)**: Observed in % (Cald. in %): C: 77.10 (77.49); H: 9.26 (9.90); N: 3.41 (3.93). **MP**: 165-168 °C.

### S2.12. UV-vis absorption spectrum of [(Dipp)(Cy-cAl)P(CoCl)<sub>3</sub>CoO] (3b)

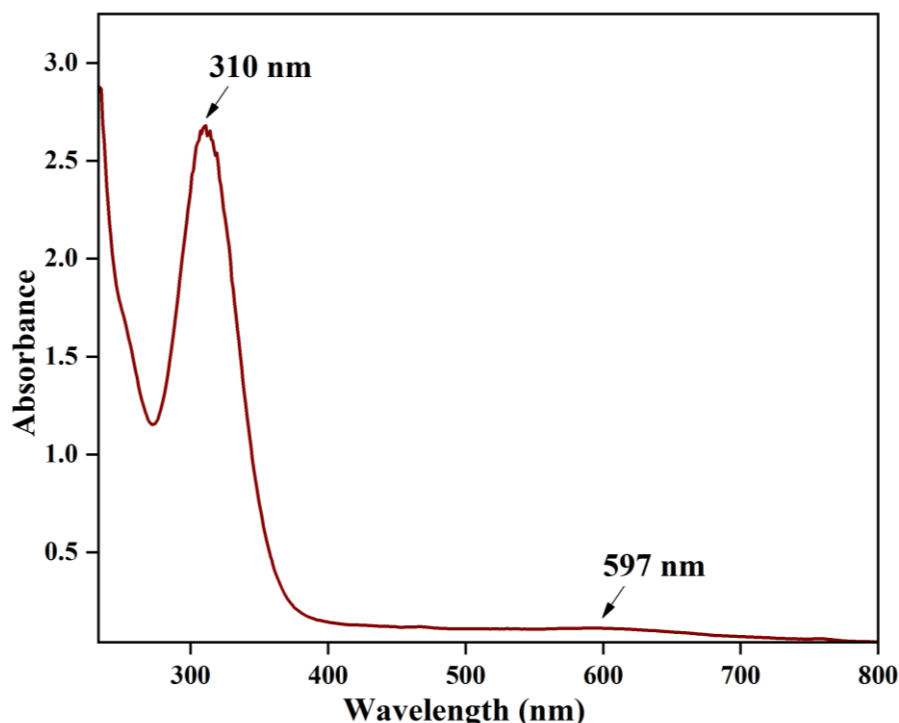
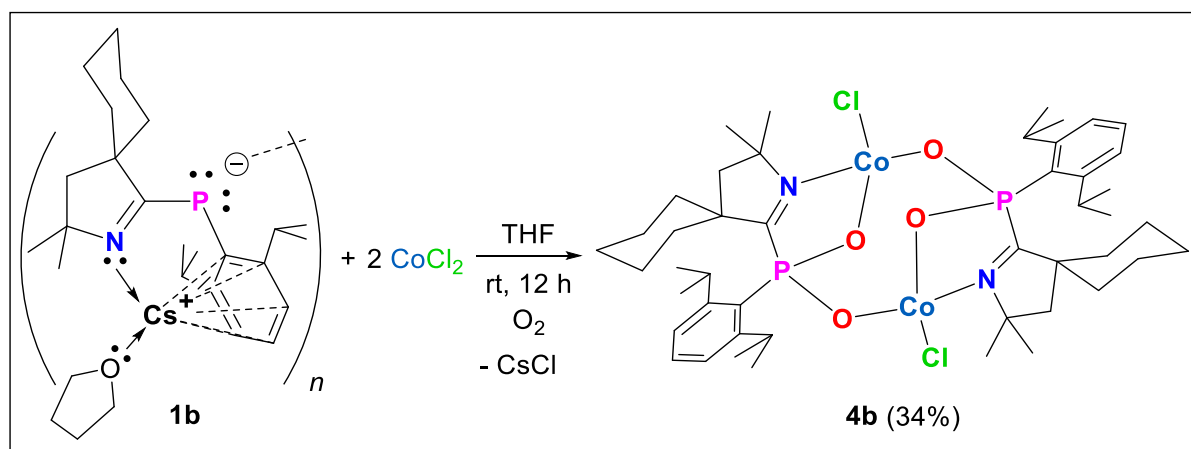


**Figure S7.** UV-vis absorption spectrum of [(Dipp)(Cy-cAl)P(CoCl)<sub>3</sub>CoO] (**3b**) in DCM solution at rt.

### S2.13. Synthesis of $\left[\text{((Dipp)(Cy-cAl)PO}_2\text{Co}^{\text{II}}\text{Cl})_2\right]$ (**4b**)



**Scheme S4.** Synthesis of  $\left[\text{((Dipp)(Cy-cAl)PO}_2\text{Co}^{\text{II}}\text{Cl})_2\right]$  (**4b**).

In an oven-dried Schlenk flask,  $\left[\text{((Dipp)(Cy-cAl)P)}_2\text{Cs}_2(\text{THF})_4\right]_n$  (**1b**) (100 mg, 0.17 mmol, 1 equiv) and anhydrous  $\text{CoCl}_2$  (44 mg, 0.34 mmol, 2 equiv) were taken. Added freshly distilled THF (15 mL) at rt to obtain a clear dark blueish-black solution and stirred overnight. The black colour precipitate formed after overnight stirring was then filtered using a frit to obtain a greenish blue color filtrate, which was then exposed to air until the color turns to bright blue (ca. 5-10 min). Afterwards, the dark blue filtrate was completely dried under a reduced pressure to obtain the dark blue crystalline solid, which was extracted in anhydrous DCM. The concentrated DCM solution (2 mL) was then stored at -40 °C in a freezer. The dark blue colored block-shaped crystals of complex **4b** suitable for single crystal X-ray diffraction were formed after 3 weeks in 34% of isolated yield (28 mg). **Elemental analysis for  $\text{C}_{46}\text{H}_{70}\text{Cl}_2\text{Co}_2\text{N}_2\text{O}_4\text{P}_2$  (**4b**):** Observed in % (Cald. in %): C: 57.32 (57.21); H: 7.26 (7.31); N, 2.81 (2.90). **MP:** 173-175 °C.

### S2.14. Electron Paramagnetic Resonance (EPR) study of complex $\left[\text{((Dipp)(Cy-cAl)PO}_2\text{Co}^{\text{II}}\text{Cl})_2\right]$ (**4b**) in DCM at 298 K

Complex **4b** was found to be EPR active. The EPR spectrum of a diluted DCM solution of complex **4b** at X-band (8.75-9.65 GHz) was recorded using a JEOL Model JES FA200 EPR spectrometer at 298 K, which exhibited a characteristic signal. The sample preparation was done under argon atmosphere using a standard glove box technique.

**EPR spectrum of complex  $\text{[((Dipp)(Cy-cAl)PO}_2\text{(Co}^{\text{II}}\text{Cl})_2\text{)]}$  (4b) in DCM at 298 K**

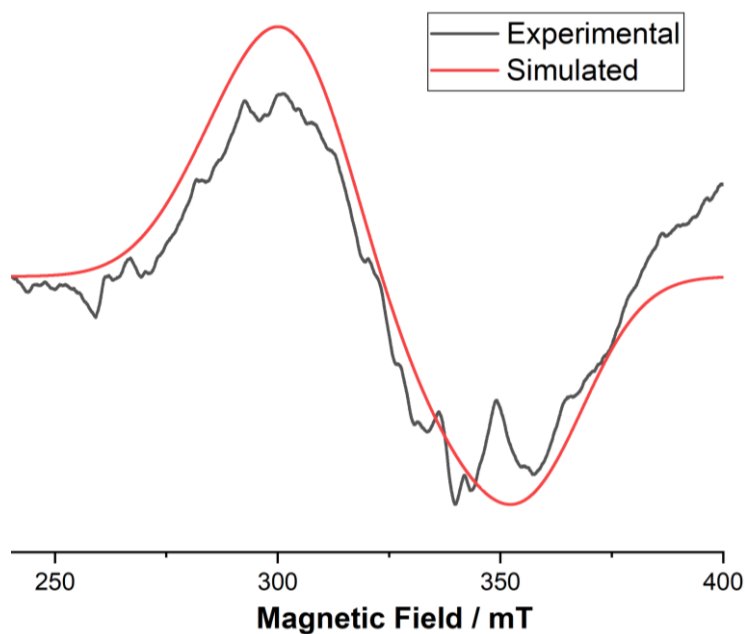


**Figure S8.** X-band EPR spectrum of  $\text{[((Dipp)(Cy-cAl)PO}_2\text{(Co}^{\text{II}}\text{Cl})_2\text{)]}$  (**4b**) in DCM at 298 K. The black line represents the experimental spectrum, and the red line represents the fitted spectrum (using EasySpin program).<sup>[4]</sup> [g<sub>x</sub> = 2.0211, g<sub>y</sub> = 2.0225, g<sub>z</sub> = 2.22672, LWPP = 25.0875 mT, A = 186.043 MHz.]

**Calculation of Lande factor (g):**

$$g = \frac{h\nu}{\mu_B H} \quad \text{where,}$$

h = Planck's constant,

$\nu$  = Operating frequency,

$\mu_B$  = Bohr magneton,

H = Magnetic field

g = Lande factor

$h = 6.626 \times 10^{-34} \text{ JS}$ ,

$\nu = 9449.064 \text{ MHz} = 9449.064 \times 10^6 \text{ Hz}$ ,

$\mu_B = \text{Bohr's magneton} = 9.2740 \times 10^{-24} \text{ JT}^{-1}$ ,

H = magnetic field = data on x-axis in mT = 324.1126 mT =  $324.1126 \times 10^{-3} \text{ T}$

$$g = \frac{6.626 \times 10^{-34} \text{ JS} \times 9449.064 \times 10^6 \text{ S}^{-1}}{9.2740 \times 10^{-24} \text{ JT}^{-1} \times 324.1126 \times 10^{-3} \text{ T}}$$

$$g = 2.0829$$

**S2.15. IR Spectrum of  $\text{[((Dipp)(Cy-cAl)PO}_2\text{(Co}^{\text{II}}\text{Cl})_2]$  (4b)**

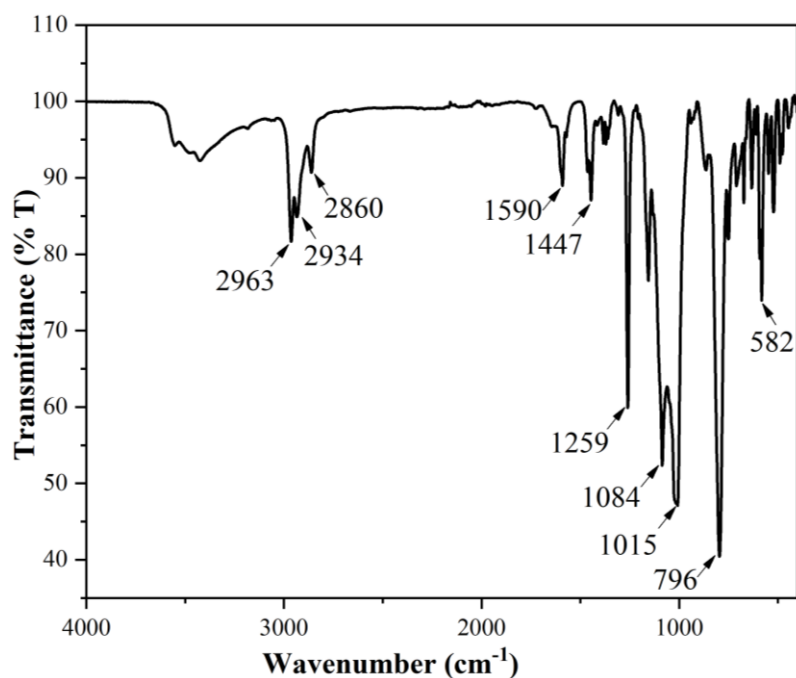


**Figure S9.** IR spectrum of  $\text{[((Dipp)(Cy-cAl)PO}_2\text{(Co}^{\text{II}}\text{Cl})_2]$  (4b).

**S2.16. UV-vis absorption spectrum of  $\text{[((Dipp)(Cy-cAl)PO}_2\text{(Co}^{\text{II}}\text{Cl})_2]$  (4b)**

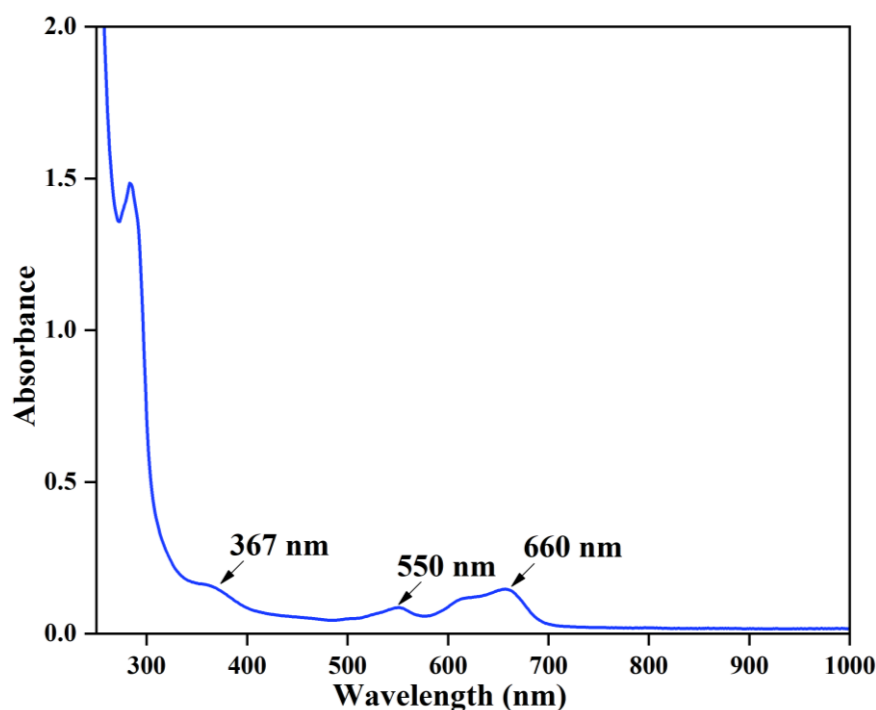


**Figure S10.** UV-vis absorption spectrum of  $\text{[((Dipp)(Cy-cAl)PO}_2\text{(Co}^{\text{II}}\text{Cl})_2]$  (4b) in DCM solution at rt.

### S3. Cyclic voltammetry (CV) studies of complex $\text{[((Dipp)(Et}_2\text{-cAl)}\text{P)}_2\text{Cs}_2(\text{THF})_4]_n$ (**1a**), **3a**, and **4a-4b**

The cyclic voltammetry studies of complex  $\text{[((Dipp)(Et}_2\text{-cAl)}\text{P)}_2\text{Cs}_2(\text{THF})_4]_n$  (**1a**) have been performed at a Metrohm-Autolab204 Potentiostat. All experiments have been performed under argon atmosphere in deoxygenated, and anhydrous THF solution of 0.1 M  $[n\text{-Bu}_4\text{N}]PF_6$  used as the electrolyte. The setup consisted of a glassy carbon (GC) working electrode (WE), a Pt wire as the counter electrode (CE) and Ag wire as the reference electrode (RE). The recorded voltammograms have been referenced to the internal standard  $(Cp)_2Fe/(Cp)_2Fe^+$ , which was added after the measurements.

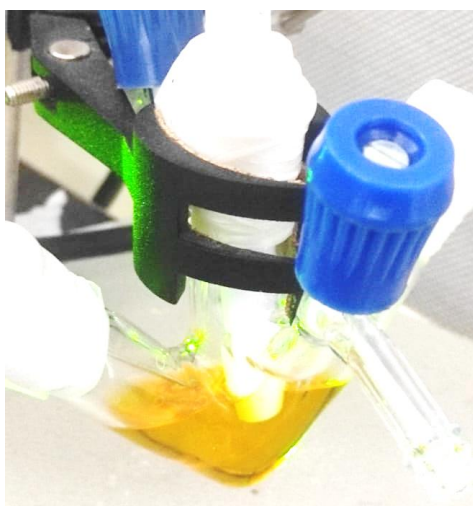
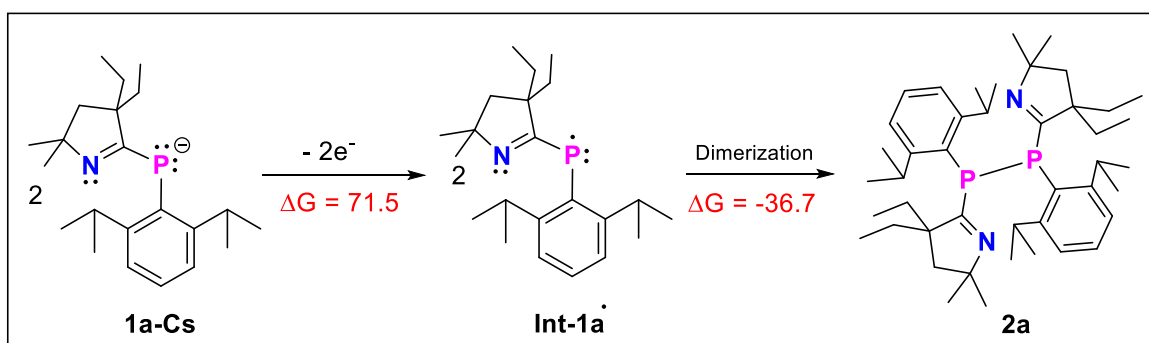


**Figure S11.** The CV setup of  $\text{[((Dipp)(Et}_2\text{-cAl)}\text{P)}_2\text{Cs}_2(\text{THF})_4]_n$  (**1a**) in THF containing 0.1 M  $[n\text{-Bu}_4\text{N}]PF_6$  as the electrolyte. CE (counter electrode): Pt, WE (working electrode): GC, RE (reference electrode): Ag.



**Scheme S5.** Synthetic route for generation of the bis-(aryl)(imino)-phosphene (**2a**).  $\Delta G_{298K}$  values are calculated at B3LYP/def2-SVP level of theory. Energies are in kcal/mol.



**Figure S12.** The CV setup of  $\text{[((Dipp)(Et}_2\text{-cAl)PO}_2\text{(Co}^{\text{II}}\text{Cl})_2]$  (**4a**) in THF containing 0.1 M  $[n\text{-Bu}_4\text{N}]PF_6$  as the electrolyte. CE (counter electrode): Pt, WE (working electrode): GC, RE (reference electrode): Ag.

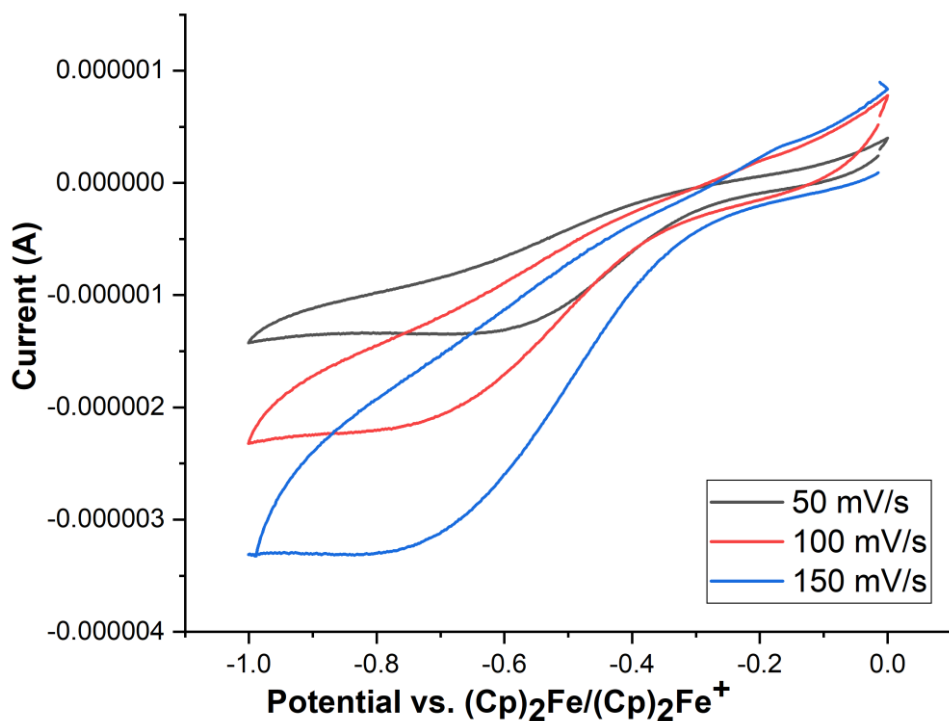


**Figure S13.** Cyclic voltammograms of  $\text{[((Dipp)(Et}_2\text{-cAl)PO}_2\text{(Co}^{\text{II}}\text{Cl})_2]$  (**4a**) in DCM containing 0.1 M  $[n\text{-Bu}_4\text{N}]PF_6$  as the electrolyte (CE: Pt, WE: GC, RE: Ag).

#### S4. Crystallographic details of **2a-2b**, **3a**, and **4a-4b**

The single-crystal X-ray data were collected on a Bruker D8 VENTURE diffractometer equipped with PHOTON III C28 detector using  $I\mu S$  3.0 microfocus sealed X-ray source

with Molybdenum K $\alpha$  ( $\lambda = 0.71073 \text{ \AA}$ ) radiation. Complete data set was collected following the strategies generated using the APEX4<sup>4</sup> module of the Bruker software suite. The data reduction was carried out using SAINTPLUS,<sup>4</sup> and multi-scan absorption correction was performed using the program SADABS.<sup>4</sup> The crystal structures were solved by intrinsic phasing method (SHELXT),<sup>5</sup> and was refined with full-matrix least squares on F<sup>2</sup> using ShelXle<sup>6</sup> plug-in included in APEX4. All non-hydrogen atoms were refined anisotropically. OLEX2 Version 1.3.0 was used for structure solution and refinement.<sup>7</sup> Ortep-3 was used to produce the thermal ellipsoid plots of all the structures.<sup>8</sup>

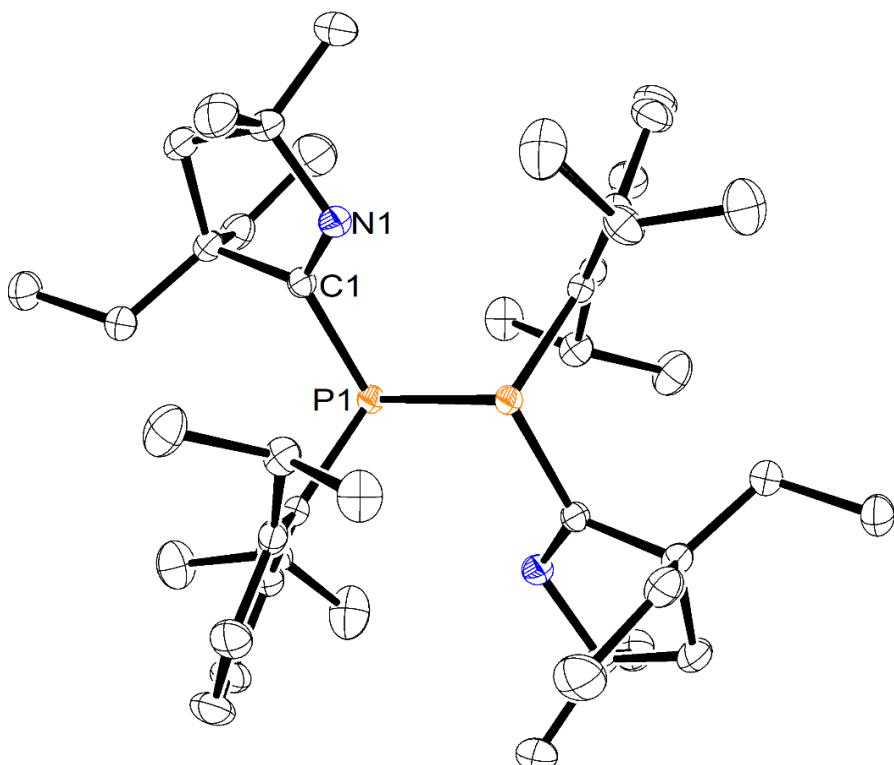


**Figure S14.** Molecular structure of **2a**. The anisotropic displacement parameters are depicted at 50% probability level. Hydrogen atoms are omitted for clarity. Important bond lengths [ $\text{\AA}$ ], and bond angles [°]: P1—P1<sup>i</sup> 2.2237(6) [2.24128], P1—C1 1.8550(12) [1.857], N1—C1 1.2718(16) [1.274]; C1—P1—P1<sup>i</sup> 100.40(4) [99.89], N1—C1—P1 123.11(9) [123.65]

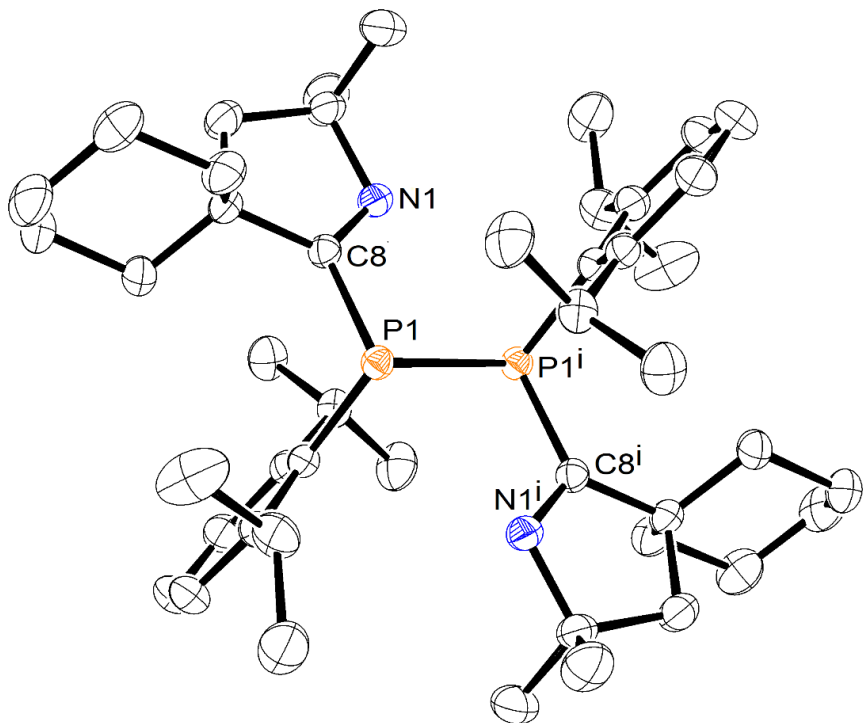


**Figure S15.** Molecular structure of **2b**. The anisotropic displacement parameters are depicted at 50% probability level. Hydrogen atoms are omitted for clarity. Important [calculated at BP86/gen] bond lengths [ $\text{\AA}$ ], and bond angles [ $^\circ$ ] P1—P1<sup>i</sup> 2.2350(8) [2.232], P1—C8 1.8437(14) [1.850], N1—C8 1.2717(18) [1.278]; C8—P1—P1<sup>i</sup> 98.55(5) [95.8], N1—C8—P1 120.41(10) [121.7].

The optimum structure of **2b** was calculated in the singlet state at the B3LYP/gen level of theory where def2-SVP was used for C, H and N atoms and def2-TZVP was used for P atom. The Dipp group on P atom was reduced to Me in to reduce the **2b** computational time. The calculated bond parameters were found to be well in agreement with the experimentally observed values.

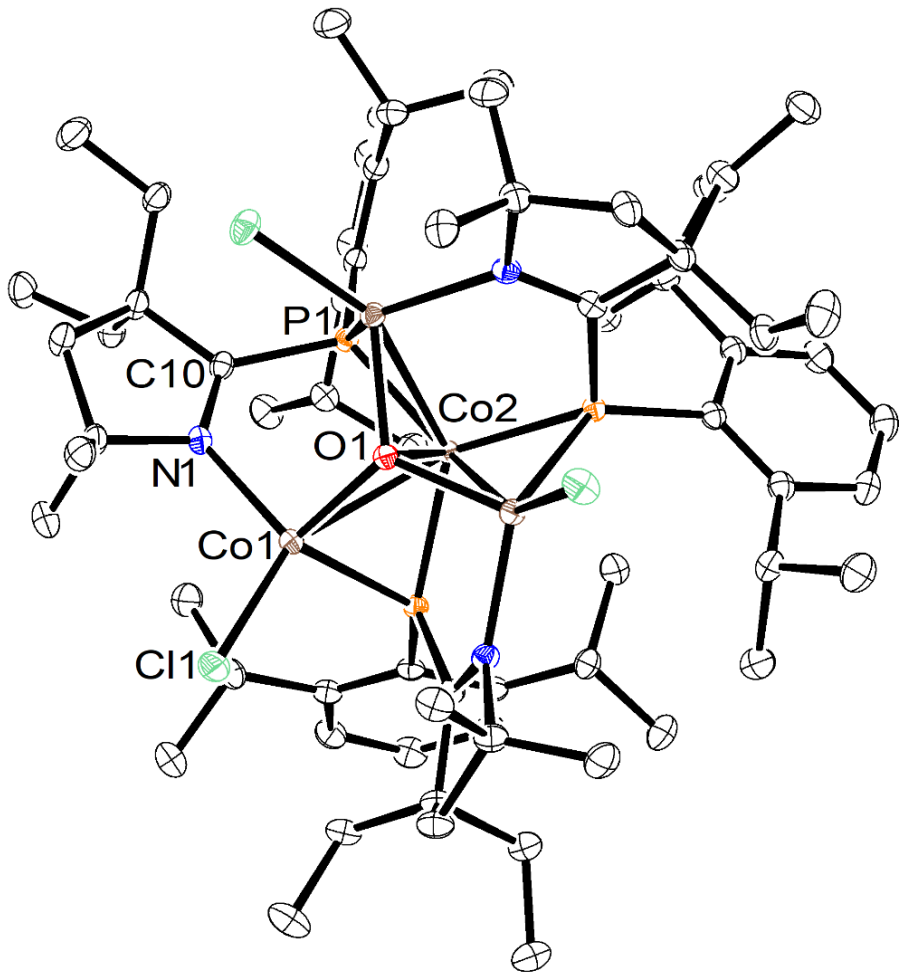


**Figure S16.** Molecular structure of  $\text{Co}^{\text{II}}_4$  metal cluster  $\text{[((Dipp)(Et}_2\text{-cAl})\text{P}(\text{CoCl})_3\text{CoO}]}$  (3a). The anisotropic displacement parameters are depicted at 50% probability level.

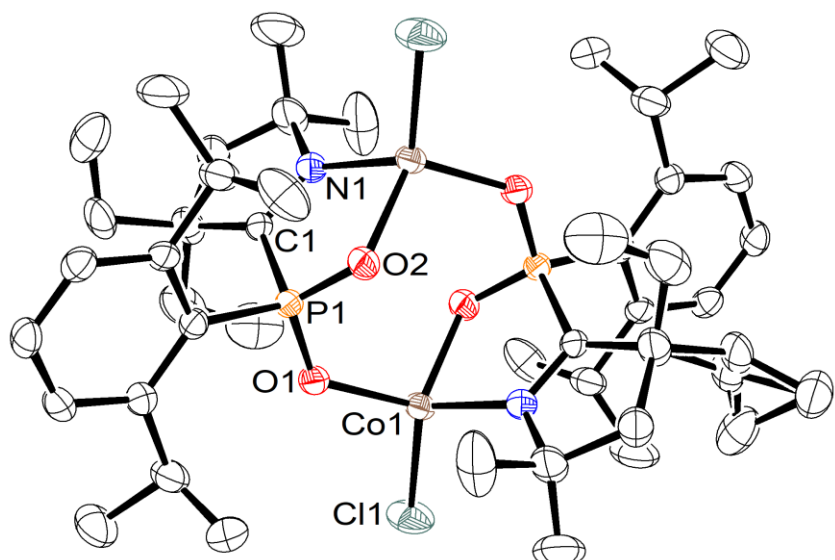


**Figure S17.** Molecular structure of  $\text{[((Dipp)(Et}_2\text{-cAl})\text{PO}_2]_2(\text{Co}^{\text{II}}\text{Cl})_2$  (4a). The anisotropic displacement parameters are depicted at 50% probability level.

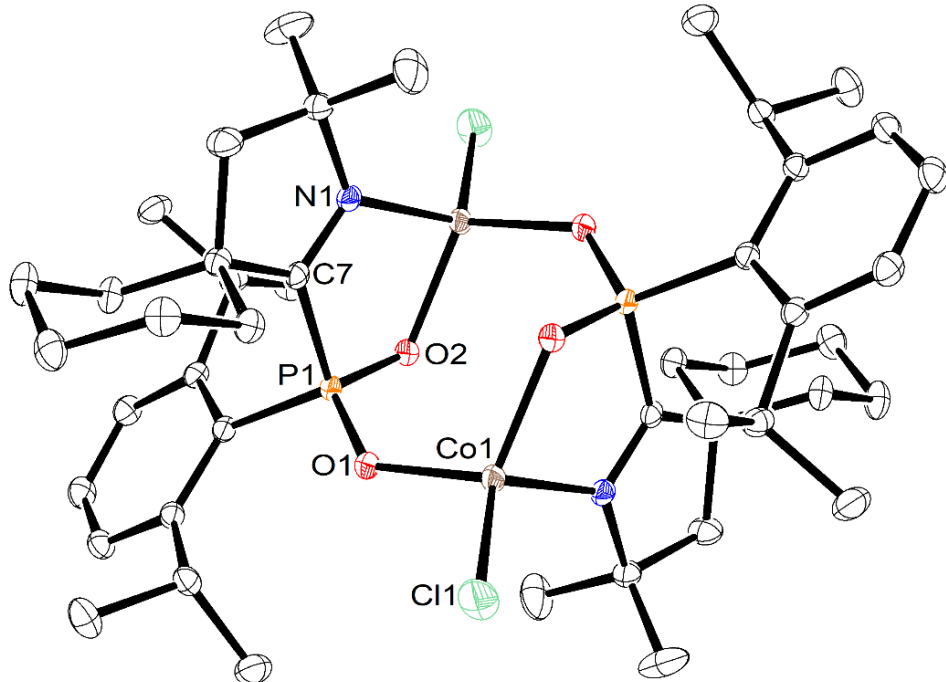


**Figure S18.** Molecular structure of **4b**. The anisotropic displacement parameters are depicted at 50% probability level. Hydrogen atoms and THF (solvent) are omitted for clarity. Important bond lengths [Å], and bond angles [°]: Co1—Cl1 2.1927(5), Co1—O1 1.9529(10), Co1—N1<sup>i</sup> 2.0489(12), P1—O2 1.5188(11), P1—O1 1.5050(11), P1—C7 1.8433(14), N1—C7 1.2820(18); O2—P1—O1 114.43(6), P1—O2—Co1<sup>i</sup> 115.78(6).

The P—C bond lengths observed in complex **4b**, which measure 1.8433(14) Å, align well with the typical distances expected for P—C single bonds, as also demonstrated by the P—C bond distance in the NHC:→PCl<sub>3</sub> adduct measuring 1.871(11) Å.<sup>9</sup> These measurements also closely resemble those found in complex **3a**, which shows a P—C bond length of 1.8397(17) Å. Within the structure of **4b**, the two P—O bond distances, 1.5050(11) Å and 1.5188(11) Å, are nearly identical, indicating the delocalization within the O—P—O moiety. Although these P—O bond lengths are marginally longer than those seen in NHC<sub>2</sub>(PO<sub>2</sub>)<sub>2</sub> (1.470(2), 1.466(3) Å)<sup>10</sup> and the free P—O bond in [(P<sub>2</sub>O<sub>4</sub>)<sup>{Re(PyrPz)(PNP)}<sub>2</sub>](1.484(5) Å),<sup>11</sup> they are shorter than the bridging P—O bond length of 1.685(5) Å found in the same compound. The dimensions of these bonds in **4b** are similar to the computed P—O distances in [Re(PyrPz)(PNP)(PO<sub>2</sub>)], which are 1.508 and 1.511 Å, using the RI-M06L/def2-SVP computational model.<sup>11</sup></sup>

**Table S1.** X-ray crystallographic refinement parameters for compound **2a**, and complexes **3a-4a**.

Crystal formula	$\text{C}_{44}\text{H}_{70}\text{N}_2\text{P}_2$	$\text{C}_{66}\text{H}_{105}\text{Cl}_3\text{Co}_4\text{N}_3\text{OP}_3$	$\text{C}_{44}\text{H}_{70}\text{Cl}_2\text{Co}_2\text{N}_2\text{O}_4\text{P}_2$
<b>Compound</b>	<b>2a</b>	<b>3a</b>	<b>4a</b>
<b><math>M_r</math></b>	688.96	1391.50	941.72
<b>CCDC Number</b>	2324725	2324727	2324726
<b>Crystal system</b>	Triclinic	Trigonal, $R\bar{3}c$	Monoclinic
<b>Space group</b>	$P\bar{1}$	$R\bar{3}c$	$P2_1/n$
<b>Temperature (K)</b>	150	100	100
<b>a (Å)</b>	9.5127 (13)	23.4395 (6)	10.1686 (5)
<b>b (Å)</b>	11.3592 (14)	23.4395 (6)	12.4842 (6)
<b>c (Å)</b>	11.7695 (15)	21.0260 (8)	18.9809 (8)
<b><math>\alpha</math> (°)</b>	113.315 (3)	90	90
<b><math>\beta</math> (°)</b>	102.042 (4)	90	96.897 (2)
<b><math>\gamma</math> (°)</b>	107.947 (4)	90	90
<b><math>V</math> (Å<sup>3</sup>)</b>	1028.5 (2)	10004.2 (6)	2392.13 (19)
<b>Z</b>	1	6	2
<b><math>\lambda</math> (Å)</b>	0.71073	0.71073	0.71073
<b><math>\mu</math> (mm<sup>-1</sup>)</b>	0.14	1.21	0.91
<b><math>R_{\text{int}}</math></b>	0.035	0.033	0.046
<b><math>R_1</math> [<math>I &gt; 2\sigma(I)</math>]</b>	0.033	0.014	0.054
<b>wR(<math>F^2</math>)</b>	0.084	0.037	0.141
<b>No. of measured reflections</b>	24992	184854	27890

<b>Independent reflections</b>	3487	4504	4391
<b>observed [<math>I &gt; 2\sigma(I)</math>] reflections</b>	3366	4479	3919
$\Delta\rho_{\text{max}}$ (e Å <sup>-3</sup> )	0.28	0.22	2.42
$\Delta\rho_{\text{min}}$ (e Å <sup>-3</sup> )	-0.25	-0.13	-0.39
<b>GooF</b>	1.07	1.08	1.07

**Table S2.** X-ray crystallographic refinement parameters for compound **2b** and complexes **3b**, and **4b**.

<b>Crystal formula</b>	C <sub>46</sub> H <sub>70</sub> N <sub>2</sub> P <sub>2</sub>	C <sub>46</sub> H <sub>70</sub> Cl <sub>2</sub> Co <sub>2</sub> N <sub>2</sub> O <sub>4</sub> P <sub>2</sub> ·2(C <sub>4</sub> H <sub>8</sub> O)
<b>Compound</b>	<b>2b</b>	<b>4b</b>
<i>M</i> <sub>r</sub>	712.98	1109.94
CCDC Number	2344451	2344452
Crystal system	Monoclinic	Triclinic
Space group	<i>P</i> 2 <sub>1</sub> /n	<i>P</i> -1
Temperature (K)	300	150
<i>a</i> (Å)	12.005(4)	9.2221(8)
<i>b</i> (Å)	10.958(4)	11.5488(10)
<i>c</i> (Å)	16.343(5)	14.3412(13)
$\alpha$ (°)	90	110.948(3)
$\beta$ (°)	91.104(11)	96.154(4)
$\gamma$ (°)	90	94.802(4)
<i>V</i> (Å <sup>3</sup> )	2149.5(12)	1405.9(2)

$Z$	2	1
$\lambda$ (Å)	0.71073	0.71073
$\mu$ (mm <sup>-1</sup> )	0.13	0.79
$R_{\text{int}}$	0.076	0.064
$R_1$ [ $I > 2\sigma(I)$ ]	0.043	0.036
$wR(F^2)$	0.125	0.095
No. of measured reflections	128049	89969
Independent reflections	5375	8605
observed [ $I > 2\sigma(I)$ ] reflections	4104	6864
$\Delta\rho_{\text{max}}$ (e Å <sup>-3</sup> )	0.23	0.51
$\Delta\rho_{\text{min}}$ (e Å <sup>-3</sup> )	-0.27	-0.36
GooF	1.04	1.05

**Table S3.** Bond length (Å) of **2a**

P1—P1 <sup>i</sup>	2.2237 (6)	C13—H13	0.9500
P1—C11	1.8587 (12)	C13—C14	1.378 (2)
P1—C1	1.8550 (12)	C7—H7A	0.9900
N1—C1	1.2718 (16)	C7—H7B	0.9900
N1—C4	1.4868 (15)	C7—C10	1.5264 (17)
C11—C12	1.4159 (17)	C14—H14	0.9500
C11—C16	1.4154 (17)	C5—H5A	0.9800
C12—C17	1.5236 (17)	C5—H5B	0.9800
C12—C13	1.3945 (18)	C5—H5C	0.9800

C1—C2	1.5386 (16)	C19—H19A	0.9800
C16—C15	1.3918 (18)	C19—H19B	0.9800
C16—C20	1.5282 (17)	C19—H19C	0.9800
C4—C3	1.5480 (18)	C6—H6A	0.9800
C4—C5	1.5265 (18)	C6—H6B	0.9800
C4—C6	1.5266 (18)	C6—H6C	0.9800
C17—H17	1.0000	C21—H21A	0.9800
C17—C19	1.5284 (18)	C21—H21B	0.9800
C17—C18	1.5365 (17)	C21—H21C	0.9800
C15—H15	0.9500	C10—H10A	0.9800
C15—C14	1.376 (2)	C10—H10B	0.9800
C3—H3A	0.9900	C10—H10C	0.9800
C3—H3B	0.9900	C22—H22A	0.9800
C3—C2	1.5455 (16)	C22—H22B	0.9800
C8—H8A	0.9900	C22—H22C	0.9800
C8—H8B	0.9900	C18—H18A	0.9800
C8—C2	1.5394 (17)	C18—H18B	0.9800
C8—C9	1.5238 (19)	C18—H18C	0.9800
C2—C7	1.5425 (17)	C9—H9A	0.9800
C20—H20	1.0000	C9—H9B	0.9800
C20—C21	1.5299 (18)	C9—H9C	0.9800
C20—C22	1.5208 (19)		

**Table S4.** Bond angle ( $^{\circ}$ ) of **2a**

C11—P1—P1 <sup>i</sup>	100.96 (4)	C2—C7—H7A	108.6
C1—P1—P1 <sup>i</sup>	100.40 (4)	C2—C7—H7B	108.6
C1—P1—C11	105.78 (5)	H7A—C7—H7B	107.6
C1—N1—C4	110.43 (10)	C10—C7—C2	114.46 (10)
C12—C11—P1	125.26 (9)	C10—C7—H7A	108.6
C16—C11—P1	114.79 (9)	C10—C7—H7B	108.6
C16—C11—C12	119.66 (10)	C15—C14—C13	119.60 (12)
C11—C12—C17	124.47 (10)	C15—C14—H14	120.2
C13—C12—C11	118.55 (11)	C13—C14—H14	120.2
C13—C12—C17	116.84 (11)	C4—C5—H5A	109.5
N1—C1—P1	123.11 (9)	C4—C5—H5B	109.5
N1—C1—C2	116.59 (10)	C4—C5—H5C	109.5
C2—C1—P1	119.92 (8)	H5A—C5—H5B	109.5
C11—C16—C20	123.95 (11)	H5A—C5—H5C	109.5
C15—C16—C11	118.67 (11)	H5B—C5—H5C	109.5
C15—C16—C20	117.32 (11)	C17—C19—H19A	109.5
N1—C4—C3	105.79 (9)	C17—C19—H19B	109.5
N1—C4—C5	107.94 (10)	C17—C19—H19C	109.5
N1—C4—C6	108.31 (10)	H19A—C19—H19B	109.5
C5—C4—C3	111.21 (11)	H19A—C19—H19C	109.5
C5—C4—C6	109.80 (11)	H19B—C19—H19C	109.5
C6—C4—C3	113.53 (11)	C4—C6—H6A	109.5
C12—C17—H17	108.0	C4—C6—H6B	109.5

C12—C17—C19	113.76 (10)	C4—C6—H6C	109.5
C12—C17—C18	109.81 (11)	H6A—C6—H6B	109.5
C19—C17—H17	108.0	H6A—C6—H6C	109.5
C19—C17—C18	109.20 (10)	H6B—C6—H6C	109.5
C18—C17—H17	108.0	C20—C21—H21A	109.5
C16—C15—H15	119.2	C20—C21—H21B	109.5
C14—C15—C16	121.60 (12)	C20—C21—H21C	109.5
C14—C15—H15	119.2	H21A—C21—H21B	109.5
C4—C3—H3A	110.4	H21A—C21—H21C	109.5
C4—C3—H3B	110.4	H21B—C21—H21C	109.5
H3A—C3—H3B	108.6	C7—C10—H10A	109.5
C2—C3—C4	106.56 (10)	C7—C10—H10B	109.5
C2—C3—H3A	110.4	C7—C10—H10C	109.5
C2—C3—H3B	110.4	H10A—C10—H10B	109.5
H8A—C8—H8B	107.4	H10A—C10—H10C	109.5
C2—C8—H8A	108.3	H10B—C10—H10C	109.5
C2—C8—H8B	108.3	C20—C22—H22A	109.5
C9—C8—H8A	108.3	C20—C22—H22B	109.5
C9—C8—H8B	108.3	C20—C22—H22C	109.5
C9—C8—C2	115.91 (11)	H22A—C22—H22B	109.5
C1—C2—C3	100.49 (9)	H22A—C22—H22C	109.5
C1—C2—C8	111.31 (9)	H22B—C22—H22C	109.5
C1—C2—C7	110.00 (10)	C17—C18—H18A	109.5
C8—C2—C3	113.47 (10)	C17—C18—H18B	109.5

C8—C2—C7	109.77 (10)	C17—C18—H18C	109.5
C7—C2—C3	111.49 (10)	H18A—C18—H18B	109.5
C16—C20—H20	107.6	H18A—C18—H18C	109.5
C16—C20—C21	110.92 (11)	H18B—C18—H18C	109.5
C21—C20—H20	107.6	C8—C9—H9A	109.5
C22—C20—C16	112.49 (11)	C8—C9—H9B	109.5
C22—C20—H20	107.6	C8—C9—H9C	109.5
C22—C20—C21	110.42 (11)	H9A—C9—H9B	109.5
C12—C13—H13	119.2	H9A—C9—H9C	109.5
C14—C13—C12	121.55 (12)	H9B—C9—H9C	109.5
C14—C13—H13	119.2		

Symmetry code: (i)  $-x+1, -y+1, -z$ .

**Table S5.** Bond length ( $\text{\AA}$ ) of **3a**

Co3—Co2	2.7046 (3)	C11—C21	1.535 (3)
Co3—O1	1.9589 (3)	C12—H12A	0.9800
Co3—Cl2	2.2395 (5)	C12—H12B	0.9800
Co3—P2 <sup>i</sup>	2.4171 (5)	C12—H12C	0.9800
Co3—N2	2.0442 (15)	C13—H13	1.0000
Co2—O1	2.036 (2)	C13—C14	1.532 (3)
Co2—P2 <sup>ii</sup>	2.2808 (4)	C13—C3	1.538 (2)
Co2—P2	2.2808 (4)	C14—H14A	0.9800
Co2—P2 <sup>i</sup>	2.2808 (4)	C14—H14B	0.9800
P2—C23	1.8518 (17)	C14—H14C	0.9800

P2—C10	1.8397 (17)	C15—H15A	0.9800
N2—C7	1.508 (2)	C15—H15B	0.9800
N2—C10	1.296 (2)	C15—H15C	0.9800
C23—C2	1.416 (2)	C16—H16A	0.9800
C23—C6	1.425 (2)	C16—H16B	0.9800
C2—C22	1.406 (2)	C16—H16C	0.9800
C2—C11	1.524 (2)	C17—H17A	0.9900
C22—H22	0.9500	C17—H17B	0.9900
C22—C4	1.386 (3)	C17—C18	1.532 (3)
C4—H4	0.9500	C18—H18A	0.9800
C4—C5	1.386 (3)	C18—H18B	0.9800
C5—H5	0.9500	C18—H18C	0.9800
C5—C6	1.400 (2)	C19—H19A	0.9900
C6—C13	1.523 (2)	C19—H19B	0.9900
C7—C8	1.537 (3)	C19—C20	1.531 (3)
C7—C15	1.529 (3)	C20—H20A	0.9800
C7—C16	1.535 (2)	C20—H20B	0.9800
C8—H8A	0.9900	C20—H20C	0.9800
C8—H8B	0.9900	C21—H21A	0.9800
C8—C9	1.546 (2)	C21—H21B	0.9800
C9—C10	1.546 (2)	C21—H21C	0.9800
C9—C17	1.548 (2)	C3—H3A	0.9800
C9—C19	1.556 (3)	C3—H3B	0.9800
C11—H11	1.0000	C3—H3C	0.9800

C11—C12	1.536 (3)		
---------	-----------	--	--

**Table S6.** Bond angle ( $^{\circ}$ ) of **3a**

O1—Co3—Co2	48.61 (6)	C10—C9—C17	112.97 (14)
O1—Co3—Cl2	122.89 (5)	C10—C9—C19	107.56 (14)
O1—Co3—P2 <sup>i</sup>	90.30 (5)	C17—C9—C19	110.76 (15)
O1—Co3—N2	99.28 (4)	N2—C10—P2	117.99 (13)
Cl2—Co3—Co2	152.886 (15)	N2—C10—C9	114.05 (14)
Cl2—Co3—P2 <sup>i</sup>	108.254 (17)	C9—C10—P2	127.55 (12)
P2 <sup>i</sup> —Co3—Co2	52.522 (12)	C2—C11—H11	108.3
N2—Co3—Co2	94.11 (4)	C2—C11—C12	109.97 (15)
N2—Co3—Cl2	113.00 (4)	C2—C11—C21	112.91 (16)
N2—Co3—P2 <sup>i</sup>	122.11 (4)	C12—C11—H11	108.3
Co3—Co2—Co3 <sup>ii</sup>	77.365 (12)	C21—C11—H11	108.3
Co3 <sup>i</sup> —Co2—Co3 <sup>ii</sup>	77.365 (12)	C21—C11—C12	108.96 (15)
Co3 <sup>i</sup> —Co2—Co3	77.366 (12)	C11—C12—H12A	109.5
O1—Co2—Co3 <sup>i</sup>	46.194 (8)	C11—C12—H12B	109.5
O1—Co2—Co3 <sup>ii</sup>	46.194 (8)	C11—C12—H12C	109.5
O1—Co2—Co3	46.196 (8)	H12A—C12—H12B	109.5
O1—Co2—P2 <sup>ii</sup>	92.350 (14)	H12A—C12—H12C	109.5
O1—Co2—P2 <sup>i</sup>	92.350 (14)	H12B—C12—H12C	109.5
O1—Co2—P2	92.350 (14)	C6—C13—H13	107.6
P2 <sup>ii</sup> —Co2—Co3 <sup>i</sup>	57.248 (12)	C6—C13—C14	110.73 (15)
P2 <sup>ii</sup> —Co2—Co3 <sup>ii</sup>	85.980 (13)	C6—C13—C3	113.61 (15)

P2—Co2—Co3	85.979 (13)	C14—C13—H13	107.6
P2 <sup>i</sup> —Co2—Co3 <sup>i</sup>	85.980 (13)	C14—C13—C3	109.34 (15)
P2—Co2—Co3 <sup>i</sup>	134.127 (18)	C3—C13—H13	107.6
P2 <sup>i</sup> —Co2—Co3 <sup>ii</sup>	134.127 (18)	C13—C14—H14A	109.5
P2 <sup>ii</sup> —Co2—Co3	134.128 (18)	C13—C14—H14B	109.5
P2 <sup>i</sup> —Co2—Co3	57.248 (12)	C13—C14—H14C	109.5
P2—Co2—Co3 <sup>ii</sup>	57.248 (12)	H14A—C14—H14B	109.5
P2 <sup>i</sup> —Co2—P2	119.833 (2)	H14A—C14—H14C	109.5
P2 <sup>ii</sup> —Co2—P2 <sup>i</sup>	119.833 (2)	H14B—C14—H14C	109.5
P2 <sup>ii</sup> —Co2—P2	119.833 (2)	C7—C15—H15A	109.5
Co3—O1—Co3 <sup>ii</sup>	119.304 (17)	C7—C15—H15B	109.5
Co3 <sup>i</sup> —O1—Co3	119.306 (17)	C7—C15—H15C	109.5
Co3 <sup>i</sup> —O1—Co3 <sup>ii</sup>	119.305 (17)	H15A—C15—H15B	109.5
Co3—O1—Co2	85.19 (6)	H15A—C15—H15C	109.5
Co3 <sup>ii</sup> —O1—Co2	85.19 (6)	H15B—C15—H15C	109.5
Co3 <sup>i</sup> —O1—Co2	85.19 (6)	C7—C16—H16A	109.5
Co2—P2—Co3 <sup>ii</sup>	70.229 (15)	C7—C16—H16B	109.5
C23—P2—Co3 <sup>ii</sup>	132.09 (6)	C7—C16—H16C	109.5
C23—P2—Co2	131.46 (5)	H16A—C16—H16B	109.5
C10—P2—Co3 <sup>ii</sup>	90.25 (5)	H16A—C16—H16C	109.5
C10—P2—Co2	113.94 (6)	H16B—C16—H16C	109.5
C10—P2—C23	108.80 (8)	C9—C17—H17A	108.2
C7—N2—Co3	120.56 (11)	C9—C17—H17B	108.2
C10—N2—Co3	127.77 (12)	H17A—C17—H17B	107.4

C10—N2—C7	111.10 (14)	C18—C17—C9	116.31 (15)
C2—C23—P2	121.85 (13)	C18—C17—H17A	108.2
C2—C23—C6	119.71 (15)	C18—C17—H17B	108.2
C6—C23—P2	118.38 (12)	C17—C18—H18A	109.5
C23—C2—C11	125.53 (15)	C17—C18—H18B	109.5
C22—C2—C23	118.58 (16)	C17—C18—H18C	109.5
C22—C2—C11	115.89 (16)	H18A—C18—H18B	109.5
C2—C22—H22	119.2	H18A—C18—H18C	109.5
C4—C22—C2	121.64 (18)	H18B—C18—H18C	109.5
C4—C22—H22	119.2	C9—C19—H19A	108.5
C22—C4—H4	120.1	C9—C19—H19B	108.5
C22—C4—C5	119.76 (18)	H19A—C19—H19B	107.5
C5—C4—H4	120.1	C20—C19—C9	114.91 (15)
C4—C5—H5	119.5	C20—C19—H19A	108.5
C4—C5—C6	121.02 (17)	C20—C19—H19B	108.5
C6—C5—H5	119.5	C19—C20—H20A	109.5
C23—C6—C13	122.84 (15)	C19—C20—H20B	109.5
C5—C6—C23	119.28 (16)	C19—C20—H20C	109.5
C5—C6—C13	117.86 (16)	H20A—C20—H20B	109.5
N2—C7—C8	103.30 (13)	H20A—C20—H20C	109.5
N2—C7—C15	109.00 (14)	H20B—C20—H20C	109.5
N2—C7—C16	110.14 (14)	C11—C21—H21A	109.5
C15—C7—C8	113.91 (15)	C11—C21—H21B	109.5
C15—C7—C16	110.36 (15)	C11—C21—H21C	109.5

C16—C7—C8	109.90 (15)	H21A—C21—H21B	109.5
C7—C8—H8A	110.4	H21A—C21—H21C	109.5
C7—C8—H8B	110.4	H21B—C21—H21C	109.5
C7—C8—C9	106.71 (14)	C13—C3—H3A	109.5
H8A—C8—H8B	108.6	C13—C3—H3B	109.5
C9—C8—H8A	110.4	C13—C3—H3C	109.5
C9—C8—H8B	110.4	H3A—C3—H3B	109.5
C8—C9—C17	113.04 (14)	H3A—C3—H3C	109.5
C8—C9—C19	112.67 (15)	H3B—C3—H3C	109.5
C10—C9—C8	99.26 (13)		

Symmetry codes: (i)  $-x+y, -x+1, z$ ; (ii)  $-y+1, x-y+1, z$ .

**Table S7.** Bond length ( $\text{\AA}$ ) of **4a**

Co1—Cl03	2.2034 (11)	C22—H22C	0.9800
Co1—O2 <sup>i</sup>	1.993 (3)	C4—C5	1.540 (7)
Co1—O1	1.941 (2)	C4—C6	1.503 (8)
Co1—N1 <sup>i</sup>	2.042 (3)	C7—H7A	0.9900
P1—O2	1.512 (3)	C7—H7B	0.9900
P1—O1	1.514 (3)	C7—C8	1.501 (8)
P1—C11	1.813 (3)	C9A—H9AA	0.9900
P1—C1	1.843 (4)	C9A—H9AB	0.9900
N1—C1	1.282 (5)	C9A—C10A	1.46 (3)
N1—C4	1.501 (5)	C21—H21A	0.9800
C11—C12	1.425 (5)	C21—H21B	0.9800

C11—C16	1.424 (5)	C21—H21C	0.9800
C1—C2	1.522 (5)	C19—H19A	0.9800
C14—H14	0.9500	C19—H19B	0.9800
C14—C13	1.375 (6)	C19—H19C	0.9800
C14—C15	1.372 (6)	C18—H18A	0.9800
C12—C13	1.385 (5)	C18—H18B	0.9800
C12—C20	1.537 (5)	C18—H18C	0.9800
C16—C17	1.523 (5)	C8—H8A	0.9800
C16—C15	1.391 (5)	C8—H8B	0.9800
C13—H13	0.9500	C8—H8C	0.9800
C17—H17	1.0000	C5—H5A	0.9800
C17—C19	1.536 (7)	C5—H5B	0.9800
C17—C18	1.529 (6)	C5—H5C	0.9800
C15—H15	0.9500	C6—H6A	0.9800
C2—C3	1.558 (5)	C6—H6B	0.9800
C2—C7	1.521 (7)	C6—H6C	0.9800
C2—C9A	1.587 (13)	C10A—H10A	0.9800
C2—C9	1.575 (12)	C10A—H10B	0.9800
C20—H20	1.0000	C10A—H10C	0.9800
C20—C22	1.524 (6)	C9—H9A	0.9900
C20—C21	1.511 (7)	C9—H9B	0.9900
C3—H3A	0.9900	C9—C10	1.46 (2)
C3—H3B	0.9900	C10—H10D	0.9800
C3—C4	1.531 (6)	C10—H10E	0.9800

C22—H22A	0.9800	C10—H10F	0.9800
C22—H22B	0.9800		

**Table S8.** Bond angle ( $^{\circ}$ ) of **4a**

O2 <sup>i</sup> —Co1—Cl03	121.24 (8)	N1—C4—C5	106.7 (4)
O2 <sup>i</sup> —Co1—N1 <sup>i</sup>	86.90 (11)	N1—C4—C6	108.1 (4)
O1—Co1—Cl03	111.15 (8)	C3—C4—C5	111.9 (5)
O1—Co1—O2 <sup>i</sup>	108.00 (10)	C6—C4—C3	113.3 (4)
O1—Co1—N1 <sup>i</sup>	113.67 (12)	C6—C4—C5	111.8 (5)
N1 <sup>i</sup> —Co1—Cl03	113.93 (10)	C2—C7—H7A	108.4
O2—P1—O1	113.39 (15)	C2—C7—H7B	108.4
O2—P1—C11	113.51 (16)	H7A—C7—H7B	107.4
O2—P1—C1	104.95 (15)	C8—C7—C2	115.7 (4)
O1—P1—C11	111.61 (15)	C8—C7—H7A	108.4
O1—P1—C1	105.18 (16)	C8—C7—H7B	108.4
C11—P1—C1	107.44 (15)	C2—C9A—H9AA	107.2
P1—O2—Co1 <sup>i</sup>	115.66 (15)	C2—C9A—H9AB	107.2
P1—O1—Co1	129.07 (16)	H9AA—C9A—H9AB	106.8
C1—N1—Co1 <sup>i</sup>	117.6 (3)	C10A—C9A—C2	121 (2)
C1—N1—C4	111.8 (3)	C10A—C9A—H9AA	107.2
C4—N1—Co1 <sup>i</sup>	130.5 (3)	C10A—C9A—H9AB	107.2
C12—C11—P1	122.0 (3)	C20—C21—H21A	109.5
C16—C11—P1	117.9 (3)	C20—C21—H21B	109.5
C16—C11—C12	119.7 (3)	C20—C21—H21C	109.5

N1—C1—P1	113.7 (3)	H21A—C21—H21B	109.5
N1—C1—C2	115.2 (3)	H21A—C21—H21C	109.5
C2—C1—P1	131.0 (3)	H21B—C21—H21C	109.5
C13—C14—H14	120.0	C17—C19—H19A	109.5
C15—C14—H14	120.0	C17—C19—H19B	109.5
C15—C14—C13	119.9 (3)	C17—C19—H19C	109.5
C11—C12—C20	124.7 (3)	H19A—C19—H19B	109.5
C13—C12—C11	118.0 (3)	H19A—C19—H19C	109.5
C13—C12—C20	117.2 (3)	H19B—C19—H19C	109.5
C11—C16—C17	124.0 (3)	C17—C18—H18A	109.5
C15—C16—C11	118.7 (3)	C17—C18—H18B	109.5
C15—C16—C17	117.2 (3)	C17—C18—H18C	109.5
C14—C13—C12	122.2 (4)	H18A—C18—H18B	109.5
C14—C13—H13	118.9	H18A—C18—H18C	109.5
C12—C13—H13	118.9	H18B—C18—H18C	109.5
C16—C17—H17	107.6	C7—C8—H8A	109.5
C16—C17—C19	110.0 (3)	C7—C8—H8B	109.5
C16—C17—C18	113.6 (4)	C7—C8—H8C	109.5
C19—C17—H17	107.6	H8A—C8—H8B	109.5
C18—C17—H17	107.6	H8A—C8—H8C	109.5
C18—C17—C19	110.2 (4)	H8B—C8—H8C	109.5
C14—C15—C16	121.3 (3)	C4—C5—H5A	109.5
C14—C15—H15	119.3	C4—C5—H5B	109.5
C16—C15—H15	119.3	C4—C5—H5C	109.5

C1—C2—C3	100.9 (3)	H5A—C5—H5B	109.5
C1—C2—C9A	105.7 (13)	H5A—C5—H5C	109.5
C1—C2—C9	112.4 (12)	H5B—C5—H5C	109.5
C3—C2—C9A	107.8 (10)	C4—C6—H6A	109.5
C3—C2—C9	115.8 (8)	C4—C6—H6B	109.5
C7—C2—C1	111.2 (4)	C4—C6—H6C	109.5
C7—C2—C3	114.0 (4)	H6A—C6—H6B	109.5
C7—C2—C9A	115.8 (11)	H6A—C6—H6C	109.5
C7—C2—C9	102.8 (10)	H6B—C6—H6C	109.5
C12—C20—H20	107.9	C9A—C10A—H10A	109.5
C22—C20—C12	114.0 (3)	C9A—C10A—H10B	109.5
C22—C20—H20	107.9	C9A—C10A—H10C	109.5
C21—C20—C12	108.9 (4)	H10A—C10A—H10B	109.5
C21—C20—H20	107.9	H10A—C10A—H10C	109.5
C21—C20—C22	110.2 (4)	H10B—C10A—H10C	109.5
C2—C3—H3A	110.2	C2—C9—H9A	109.6
C2—C3—H3B	110.2	C2—C9—H9B	109.6
H3A—C3—H3B	108.5	H9A—C9—H9B	108.2
C4—C3—C2	107.4 (3)	C10—C9—C2	110.1 (14)
C4—C3—H3A	110.2	C10—C9—H9A	109.6
C4—C3—H3B	110.2	C10—C9—H9B	109.6
C20—C22—H22A	109.5	C9—C10—H10D	109.5
C20—C22—H22B	109.5	C9—C10—H10E	109.5
C20—C22—H22C	109.5	C9—C10—H10F	109.5

H22A—C22—H22B	109.5	H10D—C10—H10E	109.5
H22A—C22—H22C	109.5	H10D—C10—H10F	109.5
H22B—C22—H22C	109.5	H10E—C10—H10F	109.5

Symmetry code: (i)  $-x+1, -y+1, -z+1$ .

**Table S9.** Bond length ( $\text{\AA}$ ) of **2b**

P1—P1 <sup>i</sup>	2.2350(8)	C12—H12	0.9300
P1—C8	1.8437(14)	C12—C13	1.367(3)
P1—C10	1.8527(14)	C13—H13	0.9300
N1—C8	1.2717(18)	C13—C14	1.365(3)
N1—C9	1.4880(18)	C14—H14	0.9300
C1—H1A	0.9700	C14—C15	1.393(2)
C1—H1B	0.9700	C15—C20	1.518(2)
C1—C2	1.535(2)	C16—H16A	0.9600
C1—C7	1.526(2)	C16—H16B	0.9600
C2—C3	1.540(2)	C16—H16C	0.9600
C2—C4	1.537(2)	C17—H17A	0.9600
C2—C8	1.5404(18)	C17—H17B	0.9600
C3—H3A	0.9700	C17—H17C	0.9600
C3—H3B	0.9700	C18—H18	0.9800
C3—C9	1.533(2)	C18—C19	1.526(2)
C4—H4A	0.9700	C18—C22	1.525(2)
C4—H4B	0.9700	C19—H19A	0.9600
C4—C5	1.534(2)	C19—H19B	0.9600
C5—H5A	0.9700	C19—H19C	0.9600
C5—H5B	0.9700	C20—H20	0.9800
C5—C6	1.519(3)	C20—C21	1.515(3)
C6—H6A	0.9700	C20—C23	1.520(3)

C6—H6B	0.9700	C21—H21A	0.9600
C6—C7	1.509(3)	C21—H21B	0.9600
C7—H7A	0.9700	C21—H21C	0.9600
C7—H7B	0.9700	C22—H22A	0.9600
C9—C16	1.518(3)	C22—H22B	0.9600
C9—C17	1.523(3)	C22—H22C	0.9600
C10—C11	1.409(2)	C23—H23A	0.9600
C10—C15	1.4189(19)	C23—H23B	0.9600
C11—C12	1.395(2)	C23—H23C	0.9600
C11—C18	1.515(2)		

**Table S10.** Bond angle ( $^{\circ}$ ) of **2b**

C8—P1—P1 <sup>i</sup>	98.55(5)	C11—C12—H12	119.2
C8—P1—C10	103.52(6)	C13—C12—C11	121.56(17)
C10—P1—P1 <sup>i</sup>	105.70(5)	C13—C12—H12	119.2
C8—N1—C9	110.19(11)	C12—C13—H13	120.0
H1A—C1—H1B	107.9	C14—C13—C12	119.98(16)
C2—C1—H1A	109.2	C14—C13—H13	120.0
C2—C1—H1B	109.2	C13—C14—H14	119.1
C7—C1—H1A	109.2	C13—C14—C15	121.78(16)
C7—C1—H1B	109.2	C15—C14—H14	119.1
C7—C1—C2	112.11(13)	C10—C15—C20	123.60(14)
C1—C2—C3	111.45(13)	C14—C15—C10	118.15(15)
C1—C2—C4	109.03(12)	C14—C15—C20	118.25(14)
C1—C2—C8	112.65(11)	C9—C16—H16A	109.5
C3—C2—C8	99.68(11)	C9—C16—H16B	109.5
C4—C2—C3	112.71(13)	C9—C16—H16C	109.5
C4—C2—C8	111.14(12)	H16A—C16—H16B	109.5

C2—C3—H3A	110.5	H16A—C16—H16C	109.5
C2—C3—H3B	110.5	H16B—C16—H16C	109.5
H3A—C3—H3B	108.7	C9—C17—H17A	109.5
C9—C3—C2	106.20(12)	C9—C17—H17B	109.5
C9—C3—H3A	110.5	C9—C17—H17C	109.5
C9—C3—H3B	110.5	H17A—C17—H17B	109.5
C2—C4—H4A	109.1	H17A—C17—H17C	109.5
C2—C4—H4B	109.1	H17B—C17—H17C	109.5
H4A—C4—H4B	107.8	C11—C18—H18	107.6
C5—C4—C2	112.52(15)	C11—C18—C19	110.69(14)
C5—C4—H4A	109.1	C11—C18—C22	112.46(13)
C5—C4—H4B	109.1	C19—C18—H18	107.6
C4—C5—H5A	109.3	C22—C18—H18	107.6
C4—C5—H5B	109.3	C22—C18—C19	110.76(14)
H5A—C5—H5B	107.9	C18—C19—H19A	109.5
C6—C5—C4	111.77(15)	C18—C19—H19B	109.5
C6—C5—H5A	109.3	C18—C19—H19C	109.5
C6—C5—H5B	109.3	H19A—C19—H19B	109.5
C5—C6—H6A	109.4	H19A—C19—H19C	109.5
C5—C6—H6B	109.4	H19B—C19—H19C	109.5
H6A—C6—H6B	108.0	C15—C20—H20	107.4
C7—C6—C5	111.11(16)	C15—C20—C23	113.66(17)
C7—C6—H6A	109.4	C21—C20—C15	111.75(17)
C7—C6—H6B	109.4	C21—C20—H20	107.4
C1—C7—H7A	109.5	C21—C20—C23	108.82(16)
C1—C7—H7B	109.5	C23—C20—H20	107.4
C6—C7—C1	110.91(16)	C20—C21—H21A	109.5
C6—C7—H7A	109.5	C20—C21—H21B	109.5

C6—C7—H7B	109.5	C20—C21—H21C	109.5
H7A—C7—H7B	108.0	H21A—C21—H21B	109.5
N1—C8—P1	120.41(10)	H21A—C21—H21C	109.5
N1—C8—C2	115.90(12)	H21B—C21—H21C	109.5
C2—C8—P1	122.64(9)	C18—C22—H22A	109.5
N1—C9—C3	104.92(12)	C18—C22—H22B	109.5
N1—C9—C16	107.13(14)	C18—C22—H22C	109.5
N1—C9—C17	109.0(14)	H22A—C22—H22B	109.5
C16—C9—C3	113.39(15)	H22A—C22—H22C	109.5
C16—C9—C17	110.33(16)	H22B—C22—H22C	109.5
C17—C9—C3	111.68(15)	C20—C23—H23A	109.5
C11—C10—P1	124.74(10)	C20—C23—H23B	109.5
C11—C10—C15	119.90(13)	C20—C23—H23C	109.5
C15—C10—P1	115.17(11)	H23A—C23—H23B	109.5
C10—C11—C18	124.24(12)	H23A—C23—H23C	109.5
C12—C11—C10	118.48(14)	H23B—C23—H23C	109.5
C12—C11—C18	117.24(14)		

Symmetry code: (i)  $-x+1, -y+1, -z+1$ .

**Table S11.** Bond length ( $\text{\AA}$ ) of **4b**

Co1—Cl1	2.1927(5)	C14—H14A	0.9800
Co1—O1	1.9529(10)	C14—H14B	0.9800
Co1—O2 <sup>i</sup>	1.9954(10)	C14—H14C	0.9800
Co1—N1 <sup>i</sup>	2.0489(12)	C15—H15A	0.9900
P1—O1	1.5050(11)	C15—H15B	0.9900
P1—O2	1.5188(11)	C15—C19	1.525(2)
P1—C1	1.8129(14)	C16—H16A	0.9900
P1—C7	1.8433(14)	C16—H16B	0.9900

O3—C24	1.420(3)	C16—C17	1.528(2)
O3—C27	1.417(3)	C17—H17A	0.9900
N1—C7	1.2820(18)	C17—H17B	0.9900
N1—C10	1.4906(19)	C17—C18	1.519(2)
C1—C2	1.4212(19)	C18—H18A	0.9900
C1—C6	1.425(2)	C18—H18B	0.9900
C2—C3	1.396(2)	C18—C19	1.523(3)
C2—C11	1.525(2)	C19—H19A	0.9900
C3—H3	0.9500	C19—H19B	0.9900
C3—C4	1.378(2)	C20—H20A	0.9800
C4—H4	0.9500	C20—H20B	0.9800
C4—C5	1.377(2)	C20—H20C	0.9800
C5—H5	0.9500	C21—H21A	0.9800
C5—C6	1.396(2)	C21—H21B	0.9800
C6—C13	1.525(2)	C21—H21C	0.9800
C7—C8	1.5154(19)	C22—H22A	0.9800
C8—C9	1.546 (2)	C22—H22B	0.9800
C8—C15	1.537 (2)	C22—H22C	0.9800
C8—C16	1.541(2)	C23—H23A	0.9800
C9—H9A	0.9900	C23—H23B	0.9800
C9—H9B	0.9900	C23—H23C	0.9800
C9—C10	1.539(2)	C24—H24A	0.9900
C10—C20	1.512(2)	C24—H24B	0.9900
C10—C21	1.520(2)	C24—C25	1.505(3)
C11—H11	1.0000	C25—H25A	0.9900
C11—C12	1.529(2)	C25—H25B	0.9900
C11—C22	1.533(2)	C25—C26	1.513(3)
C12—H12A	0.9800	C26—H26A	0.9900

C12—H12B	0.9800	C26—H26B	0.9900
C12—H12C	0.9800	C26—C27	1.494(4)
C13—H13	1.0000	C27—H27A	0.9900
C13—C14	1.528(2)	C27—H27B	0.9900
C13—C23	1.535(2)		

**Table S12.** Bond angle ( $^{\circ}$ ) of **4b**

O1—Co1—Cl1	110.71(3)	H14B—C14—H14C	109.5
O1—Co1—O2 <sup>i</sup>	109.79(4)	C8—C15—H15A	109.3
O1—Co1—N1 <sup>i</sup>	106.18(5)	C8—C15—H15B	109.3
O2 <sup>i</sup> —Co1—Cl1	120.75(4)	H15A—C15—H15B	108.0
O2 <sup>i</sup> —Co1—N1 <sup>i</sup>	86.84(4)	C19—C15—C8	111.57(13)
N1 <sup>i</sup> —Co1—Cl1	119.93(4)	C19—C15—H15A	109.3
O1—P1—O2	114.43(6)	C19—C15—H15B	109.3
O1—P1—C1	111.03(6)	C8—C16—H16A	109.3
O1—P1—C7	106.71(6)	C8—C16—H16B	109.3
O2—P1—C1	111.40(6)	H16A—C16—H16B	108.0
O2—P1—C7	104.17(6)	C17—C16—C8	111.58(12)
C1—P1—C7	108.61(6)	C17—C16—H16A	109.3
P1—O1—Co1	132.62(6)	C17—C16—H16B	109.3
P1—O2—Co1 <sup>i</sup>	115.78(6)	C16—C17—H17A	109.4
C27—O3—C24	104.50(18)	C16—C17—H17B	109.4
C7—N1—Co1 <sup>i</sup>	116.42(10)	H17A—C17—H17B	108.0
C7—N1—C10	111.47(12)	C18—C17—C16	111.26(13)
C10—N1—Co1 <sup>i</sup>	131.73(9)	C18—C17—H17A	109.4
C2—C1—P1	117.79(11)	C18—C17—H17B	109.4
C2—C1—C6	119.96(12)	C17—C18—H18A	109.4
C6—C1—P1	122.25(11)	C17—C18—H18B	109.4

C1—C2—C11	124.85(13)	C17—C18—C19	110.98(14)
C3—C2—C1	118.72(14)	H18A—C18—H18B	108.0
C3—C2—C11	116.38(13)	C19—C18—H18A	109.4
C2—C3—H3	119.5	C19—C18—H18B	109.4
C4—C3—C2	120.98(14)	C15—C19—H19A	109.5
C4—C3—H3	119.5	C15—C19—H19B	109.5
C3—C4—H4	119.9	C18—C19—C15	110.65(13)
C5—C4—C3	120.29(14)	C18—C19—H19A	109.5
C5—C4—H4	119.9	C18—C19—H19B	109.5
C4—C5—H5	119.1	H19A—C19—H19B	108.1
C4—C5—C6	121.78(15)	C10—C20—H20A	109.5
C6—C5—H5	119.1	C10—C20—H20B	109.5
C1—C6—C13	125.46(12)	C10—C20—H20C	109.5
C5—C6—C1	117.91(13)	H20A—C20—H20B	109.5
C5—C6—C13	116.62(13)	H20A—C20—H20C	109.5
N1—C7—P1	115.20(11)	H20B—C20—H20C	109.5
N1—C7—C8	115.71(12)	C10—C21—H21A	109.5
C8—C7—P1	128.99(10)	C10—C21—H21B	109.5
C7—C8—C9	100.61(12)	C10—C21—H21C	109.5
C7—C8—C15	111.90(11)	H21A—C21—H21B	109.5
C7—C8—C16	109.88(11)	H21A—C21—H21C	109.5
C15—C8—C9	112.51(13)	H21B—C21—H21C	109.5
C15—C8—C16	109.27(12)	C11—C22—H22A	109.5
C16—C8—C9	112.45(12)	C11—C22—H22B	109.5
C8—C9—H9A	110.2	C11—C22—H22C	109.5
C8—C9—H9B	110.2	H22A—C22—H22B	109.5
H9A—C9—H9B	108.5	H22A—C22—H22C	109.5
C10—C9—C8	107.33(12)	H22B—C22—H22C	109.5

C10—C9—H9A	110.2	C13—C23—H23A	109.5
C10—C9—H9B	110.2	C13—C23—H23B	109.5
N1—C10—C9	104.11(12)	C13—C23—H23C	109.5
N1—C10—C20	107.93(14)	H23A—C23—H23B	109.5
N1—C10—C21	108.00(13)	H23A—C23—H23C	109.5
C20—C10—C9	112.24(15)	H23B—C23—H23C	109.5
C20—C10—C21	111.66(18)	O3—C24—H24A	110.5
C21—C10—C9	112.42(16)	O3—C24—H24B	110.5
C2—C11—H11	107.8	O3—C24—C25	106.07(18)
C2—C11—C12	111.69(13)	H24A—C24—H24B	108.7
C2—C11—C22	110.86(13)	C25—C24—H24A	110.5
C12—C11—H11	107.8	C25—C24—H24B	110.5
C12—C11—C22	110.64(14)	C24—C25—H25A	111.1
C22—C11—H11	107.8	C24—C25—H25B	111.1
C11—C12—H12A	109.5	C24—C25—C26	103.32(19)
C11—C12—H12B	109.5	H25A—C25—H25B	109.1
C11—C12—H12C	109.5	C26—C25—H25A	111.1
H12A—C12—H12B	109.5	C26—C25—H25B	111.1
H12A—C12—H12C	109.5	C25—C26—H26A	110.8
H12B—C12—H12C	109.5	C25—C26—H26B	110.8
C6—C13—H13	107.7	H26A—C26—H26B	108.8
C6—C13—C14	110.89(13)	C27—C26—C25	104.88(19)
C6—C13—C23	112.32(13)	C27—C26—H26A	110.8
C14—C13—H13	107.7	C27—C26—H26B	110.8
C14—C13—C23	110.45(14)	O3—C27—C26	106.2(2)
C23—C13—H13	107.7	O3—C27—H27A	110.5
C13—C14—H14A	109.5	O3—C27—H27B	110.5
C13—C14—H14B	109.5	C26—C27—H27A	110.5

C13—C14—H14C	109.5	C26—C27—H27B	110.5
H14A—C14—H14B	109.5	H27A—C27—H27B	108.7
H14A—C14—H14C	109.5		

Symmetry code: (i)  $-x+1, -y+1, -z+1$ .

## S5. Details of Magnetic Measurements

### S5.1. Magnetic measurements of 3a

#### S5.1.1. Experimental set-up

7.3 mg of the powdered compound **3a** (molar mass  $M_m = 1391.5 \text{ g mol}^{-1}$ ) was pressed into a polypropylene capsule (QDS-4096-388 from Quantum Design) and attached to the brass half-tube sample holder (QDS-4096-391). The direct current (DC) magnetization vs temperature was measured at a magnetic field of 2500 Oe from 2 K to 50 K in settle mode and from 51 K to 300 K in sweep mode with a 1 K/min heating rate. The temperature step size for signal acquisition was 1 K with a signal averaging time of 10 seconds. Magnetization vs. field was measured at 2, 3, 4, 6, 10, 15, 25, 50, and 300 K up to 7 T with a field step size of 2500 Oe (0.25 T), a signal averaging time of 10 seconds and a two-fold redundancy per measuring point. At each temperature, the magnetic field was first increased to 7 T and then the field was decreased to zero field again. The superimposed curves for all field scans verified that no reorientation of the sample's powder particles has been induced by the magnetic field. Additionally, at 2, 3, and 4 K, full hysteresis loops have been measured up to 2000 Oe (0.2 T) with a field step size of 250 Oe.

For the alternative current (AC) measurements, the polypropylene sample capsule was attached to the polymer straw sample holder (QDS-8000-001 from Quantum Design) with the help of some polyimide tape. The AC excitation field was 5 Oe with an averaging time per measuring point of 10 seconds. The AC raw data sets have not been corrected for diamagnetic contributions.

### S5.1.2. Results and discussion

The magnetization vs magnetic field scan at 300 K of compound **3a** reveals the existence of a very small amount of an additional ferro-/ferrimagnetic impurity phase that can easily be saturated at low magnetic fields (see Figure S19; (a) and (b)). A linear fit to the experimental data from 70 down to 5 kOe returns a spontaneous magnetization  $M_s = 52.3(2)$  emu mol $^{-1}$  (zero field extrapolation). Only about 0.05 wt.% of a metallic Co impurity phase (with a saturation magnetization of about 80 emu g $^{-1}$ ), for instance, could explain such a feature. As a consequence, the inverse susceptibility vs temperature curve is strongly affected by this ferromagnetic impurity phase that contributes approximately with a temperature independent magnetization signal (see Figure S19 (c)). A fit according to a modified Curie-Weiss law  $\chi = C/(T - \theta) + \chi_0$ , with the Curie constant  $C$ , temperature  $T$ , Weiss constant  $\theta$ , is applied to determine the temperature independent susceptibility  $\chi_0 = 0.0166(1)$  cm $^3$  mol $^{-1}$ . This value is close to  $\chi_0^{MS} = M_s / H_0 = 52.3/2500$  cm $^3$  mol $^{-1} = 0.0209(1)$  cm $^3$  mol $^{-1}$  determined from the field scan at 300 K, with the magnetic field  $H_0$  applied for the susceptibility measurement. Figure S19 (d) shows the susceptibility vs temperature plot that has been corrected for the temperature independent  $\chi_0$ , that contains contributions from the ferromagnetic impurity phase as well as diamagnetic contributions from the closed atomic shells and bindings (the sample holder contributions can be neglected here). A Curie-Weiss fit  $\chi = C/(T - \theta)$  to the  $\chi_0$ -corrected susceptibility data from 200 to 300 K (red line in Figure S19 (d)) returns an effective paramagnetic moment of  $\mu_{eff} = 3.92(1)$   $\mu_B$  per Co ion and a small positive Weiss constant  $\theta = 2.7(2)$  K.  $\mu_{eff}$  is only slightly larger than the spin-only paramagnetic moment for a spin  $S = 3/2$  of  $3.87 \mu_B$  that is expected to be present for a Co(II) with a  $(e)^4(t)^3$  orbital occupation in a tetrahedral ligand field. The Figure 4 in main article shows the  $\chi T$  vs temperature plot of compound **3a** that has been derived from the  $\chi_0$ -corrected susceptibility data. The red dashed line indicates the calculated molar Curie constant  $C_{4Co(II)} = 7.50$  cm $^3$  K mol $^{-1}$  for four free Co(II) ions within a formula unit (f.u.), each with spin  $S = 3/2$ . The good agreement over a broad temperature region from 300 down to approximately 50 K of the experimentally observed  $\chi T$  value with the calculated Curie constant  $C_{4Co(II)}$  verifies the existence of 4 Co(II) in compound **3a**. Figure S19 (e) shows the magnetization vs field plots at various temperatures. Even at 2 K and at  $\mu_0 H = 7$  T the magnetization has not saturated and is still far below the theoretical saturation value of  $12 \mu_B$  for 4

magnetic Co(II) centres each with  $S = 3/2$ . This indicates that significant local single-ion anisotropies and/or antiferromagnetic exchange interactions are present that prevents the magnetic moments to be aligned along the magnetic field at low temperature. However, as shown in Figure S19 (f), compound **3a** exhibits magnetic hysteresis that is most strongly realized at 2 K, but is still slightly present at 4 K. Presumably, the ferromagnetic impurity phase that has already been observed at 300 K, exhibits hysteresis at very low temperature. As a consequence, the  $\chi T$  vs temperature data that has been obtained at small fields of 2500 Oe should not be considered below 50 K in this case. As shown in Figure S20, compound **3a** does not exhibit slow spin-lattice relaxation at 2 K within the limitations of the applied method with a maximum excitation frequency of 10 kHz.

### S5.1.3. Quantum mechanical magnetic model

The program package PHI has been used to set up a quantum mechanical magnetic model based on angular momentum basis states that has been refined to the experimental data sets. Within the framework of PHI, the CF Hamiltonian is also used in to model Zero Field Splittings (ZFS) of effective spins. The second order CF operators are intimately related to those of the standard ZFS Spin Hamiltonian and using the definitions of the CF operators, the relationships between the ZFS parameters and the CFPs are therefore expressed as  $D = 3 \cdot B_2^0$  and  $E = B_2^2$  (with the operator equivalent factors are included into the CFPs as explained below).

$$\hat{H} = \hat{H}_{\text{SO}} + \hat{H}_{\text{CF}} + \hat{H}_{\text{EX}} + \hat{H}_{\text{ZEE}} \quad (\text{S } 1)$$

with Hamilton operator for spin-orbit coupling (SO), crystal-field interaction (CF), exchange interaction (EX), and Zeeman effect (ZEE).

$$\hat{H}_{\text{SO}} = \sum_{i=1}^N \lambda_i \left( \sigma_{\text{SO},i} \vec{\hat{L}}_i \cdot \vec{\hat{S}}_i \right)$$

with spin-orbit coupling constants  $\lambda_i$ , orbital-reduction parameters  $\sigma_{\text{SO},i}$ , vector operator of total orbital momentum  $\vec{\hat{L}}_i$ , vector operator of total spin orbital momentum  $\vec{\hat{S}}_i$ .

$$\hat{H}_{\text{CF}} = \sum_{i=1}^N \sum_{k=2,4,6} \sum_{q=-k}^k \sigma_i^k B_{ki}^q \theta_k \hat{\theta}_{ki}^q$$

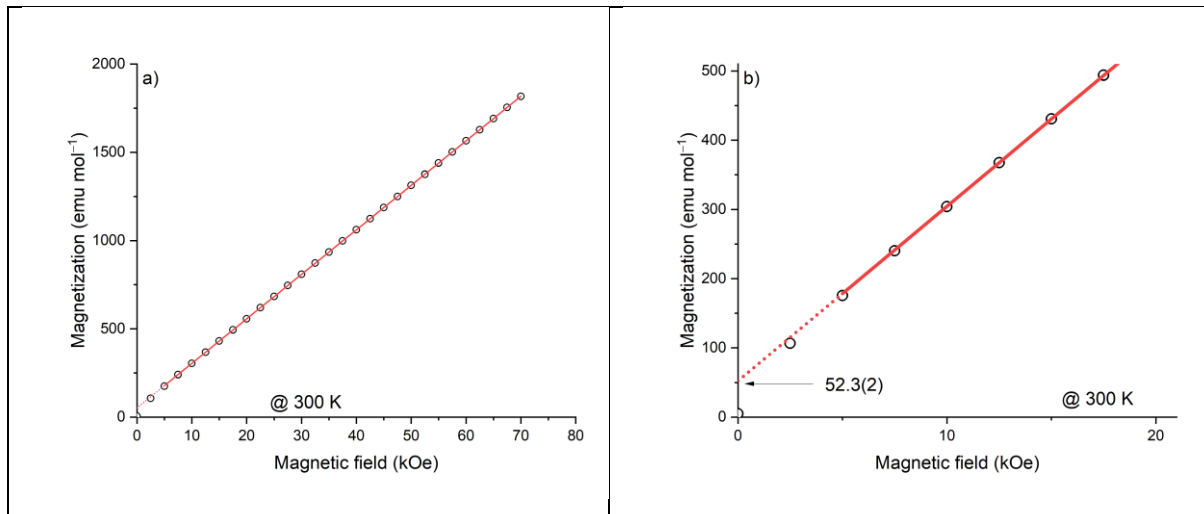
with crystal-field parameters  $B_{ki}^q$  ( $A_{ki}^q \langle r^k \rangle_i$  in Steven's notation), operator equivalent factors  $\theta_k$  and operator equivalents  $\hat{\theta}_{ki}^q$ . In this work, the operator equivalent factors are included into the CFPs by setting  $B_{ki}^q = B'_{ki}^q \theta_k$ .

$$\hat{H}_{\text{EX}} = -2 \sum_{i \neq j}^{i,j \in N} \vec{\hat{S}}_i \cdot J_{iso} \cdot \vec{\hat{S}}_j$$

with scalar isotropic exchange parameter  $J_{iso}$ .

$$\hat{H}_{\text{ZEE}} = \mu_B \sum_{i=1}^N \left( \sigma_i \vec{L}_i \cdot \bar{\vec{I}} + \vec{\hat{S}}_i \cdot \bar{\vec{g}}_i \right) \cdot \vec{B}$$

with Bohr magneton  $\mu_B$ , identity matrix  $\bar{\vec{I}}$ ,  $g$ -tensor  $\bar{\vec{g}}_i$  and magnetic induction  $\vec{B}$ .



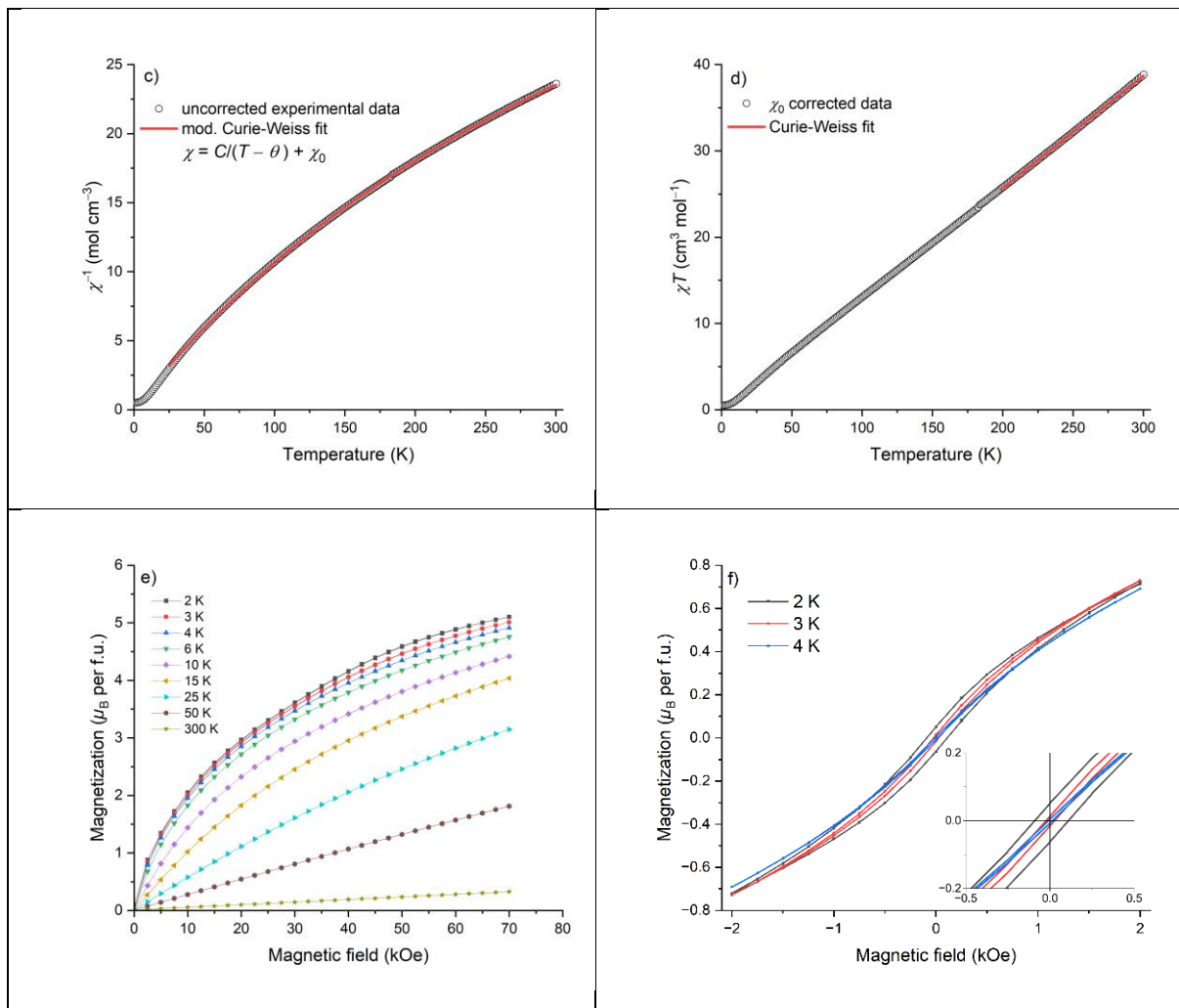


**Figure S19.** (a), (b), (e), (f): Magnetization vs magnetic field plots for **3a** at various temperatures. (c):  $\chi^{-1}$  vs T plot of **3a**; (d):  $\chi T$  vs T plot of **3a**.

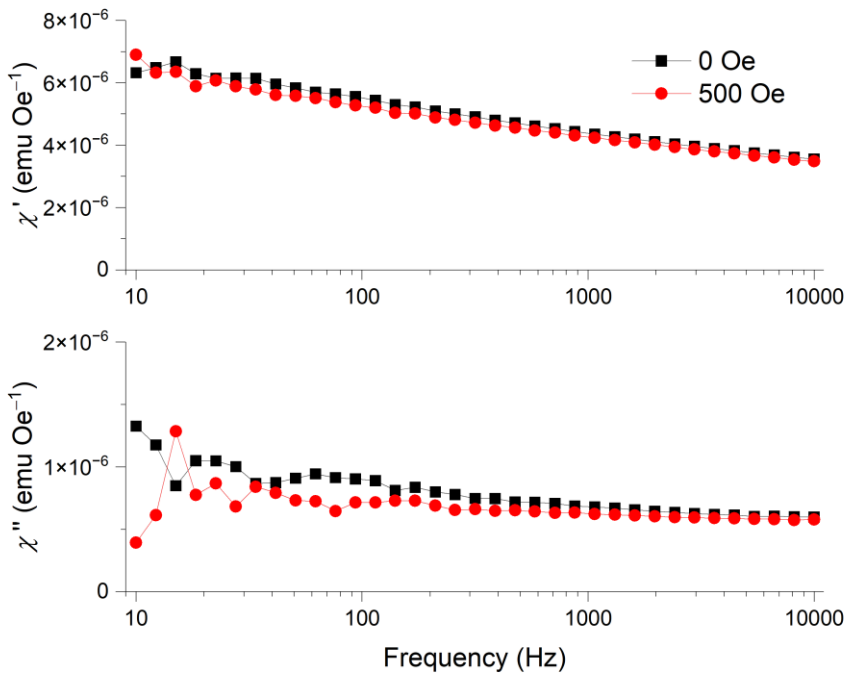


**Figure S20. Top:** In-phase susceptibility vs frequency plot of **3a**. **Bottom:** Out-of-phase susceptibility vs frequency plot of **3a**.

The magnetization at 2 K and 70 kOe (= 7 T) does not reach its theoretical maximum of  $12 \mu\text{B}$  per f.u. for four free  $S = 3/2$  Co centers without any interactions, but is limited to a value of  $5.1 \mu\text{B}$  per f.u. due to the zero-field splitting (ZFS) and exchange interactions.

### S5.2. Magnetic measurements of **4b**

The DC magnetic susceptibility measurements of **4b** have been performed, which gave the  $\chi T$  product as  $7.65 \text{ cm}^3 \text{ K mol}^{-1}$  at 300 K, which slowly decreases to  $6.77 \text{ cm}^3 \text{ K mol}^{-1}$  at 28 K (Figure S21).

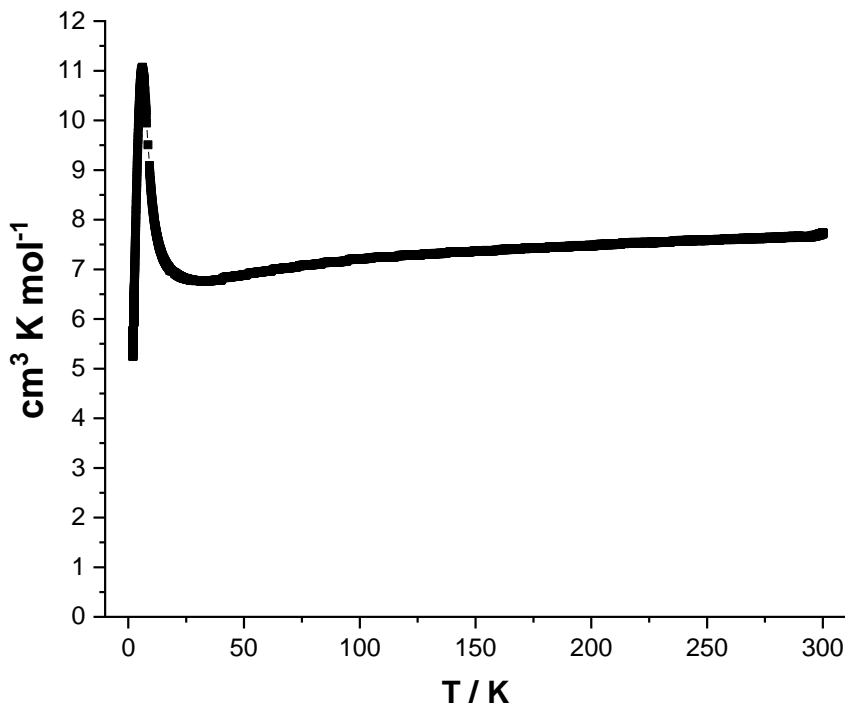


**Figure S21.** Experimental  $\chi T$  vs T plot of complex **4b**.  $H = 0.25$  T.

The  $\chi T$  product slowly raised to  $11.05 \text{ cm}^3 \text{ K mol}^{-1}$  at  $6 \text{ K}$ , below which it falls to  $5.25 \text{ cm}^3 \text{ K mol}^{-1}$  at  $2 \text{ K}$ , which can be rationalized due to the dominant FM interactions between two high-spin  $\text{Co}^{II}$  ions, and ZFS of  $S = 3$  spin ground state, respectively. The M vs H plot at  $3 \text{ K}$  showed that maximum M value is  $5.25 \mu_B$  per f.u. for  $S = 3$  without reaching a true saturation at  $9 \text{ T}$ , which may be due to the stronger magnetic anisotropy.

## S6. Computational details

We have performed Natural Bond Orbital (NBO) analysis to understand the electron densities distribution and bonding of, **3a** at UB3LYP/def2-TZVP on the coordinates optimized at UB3LYP/gen in septet state (Figure S34), where def2-SVP was used for C, H and N atoms, and def2-TZVP was used for Co, P, Cl and O atoms (Figure S35, Table S19). The Dipp (Dipp = 2,6-diisopropylphenyl) groups on P atom was reduced to Me (**3a'**) to reduce the computational time. Similarly, we have performed the calculations at ROB3LYP/gen<sup>12</sup> level of theory in the septet state for the dimeric cobalt complex **4b**, where def2-SVP was used for C, H and N atoms, and def2-TZVP was used for Co, P, Cl and O atoms. The model molecule **4b'** has been chosen for the computation, where the bulky Dipp groups are replaced by the Me groups to reduce the computational time

(Figure S37, bottom). Similarly, for the bis-(aryl)(imino)-phosphene **2b'**, calculation have been performed at B3LYP/gen level of theory in the singlet state, where def2-SVP was used for C, H and N atoms, and def2-TZVP was used for P atoms (Figure S37, top). The model molecule **2b'** has been chosen for the computation, where the bulky Dipp (Dipp = 2,6-diisopropylphenyl) groups are replaced by the Me groups to reduce the computational time.

The presence of a stable minimum on the potential energy surface has been confirmed through the absence of imaginary frequency. Experimental observations of bond parameters align well with the calculated values at ROB3LYP/gen. The NBO 6.0 software was employed to perform natural bond orbital (NBO) analyses, yielding partial charges and Wiberg bond indices.<sup>13</sup> All calculations were executed using the Gaussian 9.0 package.<sup>14</sup>

**The following oxides of P, and N are considered for our studies to compare their electron densities distributions (Figure S22).**

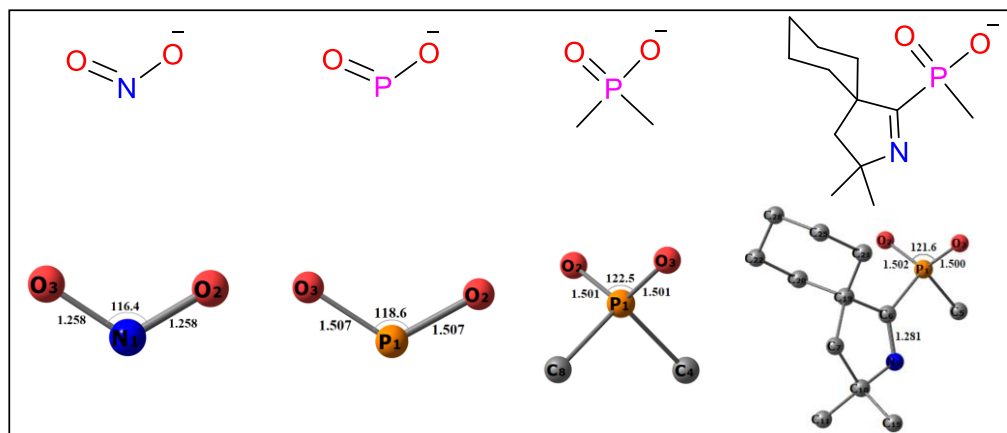


**Figure S22.** NO<sub>2</sub><sup>-</sup>, and various oxo-anions of phosphorus considered for the computational analyses of the respective electronic structures in the monomeric form.

### S6.1. Optimization, NBO, and Atoms in Molecules (AIM) analyses of the ligands PO<sub>2</sub><sup>-</sup> and NO<sub>2</sub><sup>-</sup>



**Figure S23.** Optimized structure of PO<sub>2</sub><sup>-</sup> (left) and NO<sub>2</sub><sup>-</sup> (right) in singlet state at B3LYP/def2-TZVP level of theory.

The molecular structure of  $\text{PO}_2^-$  and  $\text{NO}_2^-$  optimized by applying the density functional theory (DFT) method B3LYP/def2-TZVP (Figure S23), which was followed by natural bond orbital (NBO) analysis. The outcomes of the NBO analysis for  $\text{PO}_2^-$  and  $\text{NO}_2^-$  were discovered to be quite similar. One of the P–O/N–O bonds was found to have two bonding occupancies, while the other was discovered to have a single bond occupancy. The WBI of both P–O bonds were found to be 1.29, indicating a partial double nature and electron delocalization over the O–P–O fragment. This can be seen in the HOMO-3 of  $\text{PO}_2^-$ . On the other hand, the N–O bonds had a greater WBI (1.54) than the P–O bonds due to the optimal size of the N and O bonds, which allowed for better orbital overlap (Table S13). The HOMO-2 of  $\text{PO}_2^-$  and  $\text{NO}_2^-$  represents the lone pair on the P/N and O atoms. There is a slight extension of the lone pairs of O towards the P/N atom in HOMO-1 and HOMO-2 (Figure S24).

**Table S13.** NBO results of  $\text{PO}_2^-$  and  $\text{NO}_2^-$  ligands at the B3LYP/def2-TZVP level of theory. Occupation number (ON), polarization and hybridization of the P–O and N–O bonds

Complex	Bond	ON	Polarization and Hybridization (%)		WBI
$\text{PO}_2^-$	P1-O3	1.99	P: 17.9; s(0), p(96.4), d(3.57)	O:82.1; s(0), p(99.6)	1.29
		1.99	P: 21.9; s(18.3), p(79.7), d(1.93)	O:78.1; s(36.0), p(63.2)	
	P1-O2	1.99	P: 21.9; s(18.3), p(79.7), d(1.93)	O:78.1; s(36.0), p(63.2)	1.29
	P1 Lone pair	1.99	s(71.0), p(28.4)		
$\text{NO}_2^-$	N1-O2	1.99	N: 30.8; s(0), p(99.5)	O:69.2; s(0.00), p(99.8)	1.53

	1.99	N: 44.8; s(26.4), p(73.5)	O:55.2; s(24.9), p(74.8)	
N1-O3	1.99	N: 44.8; s(26.4), p(73.5)	O:55.2; s(24.9), p(74.8)	1.53
N1 Lone pair	1.99	s(51.3), p(48.6)		

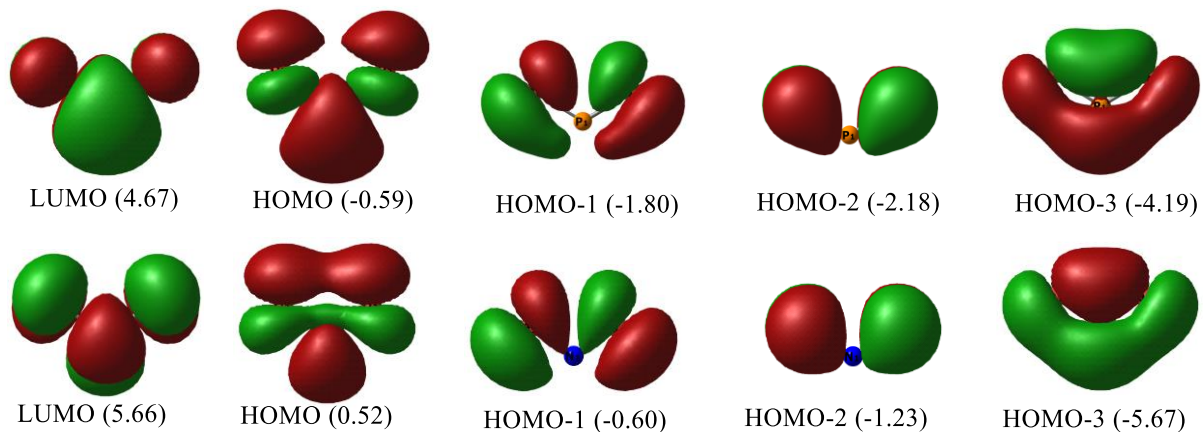


**Figure S24.** Selected orbitals of  $\text{PO}_2^-$  (top) and  $\text{NO}_2^-$  (bottom) calculated at B3LYP/def2-TZVP level of theory (energies given in parentheses are in eV).

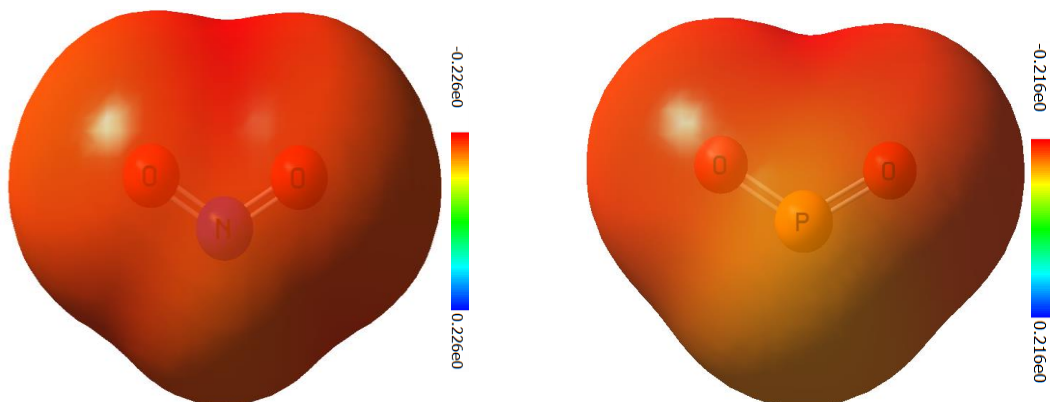


**Figure S25.** MEP plots (computed at iso-density surface value of 0.0004 a.u) of  $\text{PO}_2^-$  (left) and  $\text{NO}_2^-$  (right) calculated at B3LYP/def2-TZVP.

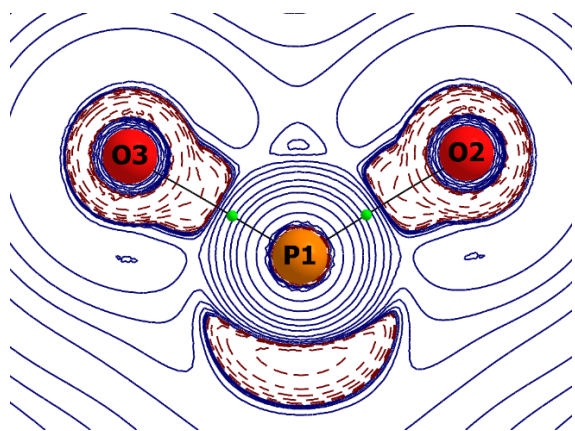


**Figure S26.** Contour plot of Laplacian distribution  $[\nabla^2\rho(r)]$  in the O-P-O plane of  $\text{PO}_2^-$ . Solid blue lines indicate the areas of charge concentration ( $\nabla^2\rho(r) < 0$ ) while dotted purple lines denotes charge depletion ( $\nabla^2\rho(r) > 0$ ). Solid lines connecting atomic nuclei (black) are the bond paths and green spheres on bond path indicates the BCP.

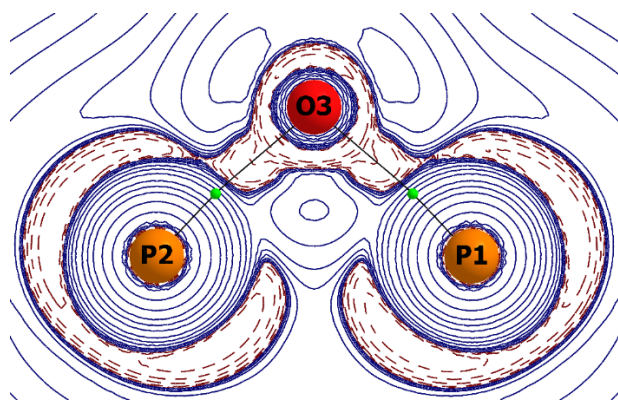


**Figure S27.** Contour plot of Laplacian distribution  $[\nabla^2\rho(r)]$  in the P-O-P plane of POP. Solid blue lines indicate the areas of charge concentration ( $\nabla^2\rho(r) < 0$ ) while dotted purple lines denotes charge depletion ( $\nabla^2\rho(r) > 0$ ). Solid lines connecting atomic nuclei (black) are the bond paths and green spheres on bond path indicates the BCP.

The important topological parameters at the (3, -1) bond critical points like the electron density  $[\rho(r)]$  and along with the respective Laplacian  $[\nabla^2\rho(r)]$  indicate the nature of the bond. The electron density  $[\rho(r)]$  at the BCP of P-O [0.212 ( $\text{PO}_2^-$ )], bond along with the respective Laplacian  $[\nabla^2\rho(r); 01.458 ( $\text{PO}_2^-$ )]$  indicates closed-shell interaction.<sup>13,14</sup>

**Table S14.** AIM results of the P–O bonds of fragments  $\text{PO}_2^-$  at B3LYP/def2-TZVP level of theory. The values are in a.u.

Fragment	Bond	$\rho(r)$	$\nabla^2\rho(r)$	Ellipticity
$\text{PO}_2^-$	P1 - O2	+0.212	+1.089	+0.094
	P1 - O3	+0.212	+1.089	+0.094

## S6.2. Optimization, NBO, and AIM analyses of the ligand $(\text{Me}_2\text{PO})_2^-$

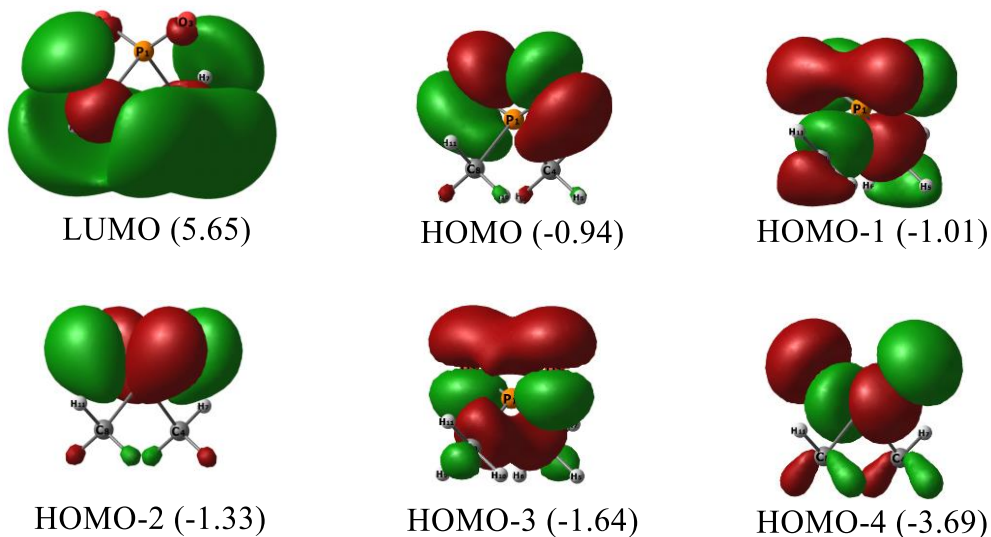


**Figure S28.** Relevant molecular orbitals of  $(\text{Me}_2\text{PO})_2^-$ .

**Table S15.** NBO results of  $(\text{Me}_2\text{PO})_2^-$  at the B3LYP/def2-TZVP level of theory. Occupation number (ON), polarization and hybridization of the P–O bond.

Complex	Bond	ON	Polarization and Hybridization (%)		WBI
$(\text{Me}_2\text{PO})_2^-$	P1-O2	1.99	P: 24.8; s(28.3), p(70.1), d(1.6)	O:75.2; s(36.9), p(62.5)	1.15

	P1-O3	1.99	P: 24.8; s(28.3), p(70.1), d(1.6)	O:75.2; s(36.9), p(62.5)	1.15
--	-------	------	--------------------------------------	-----------------------------	------

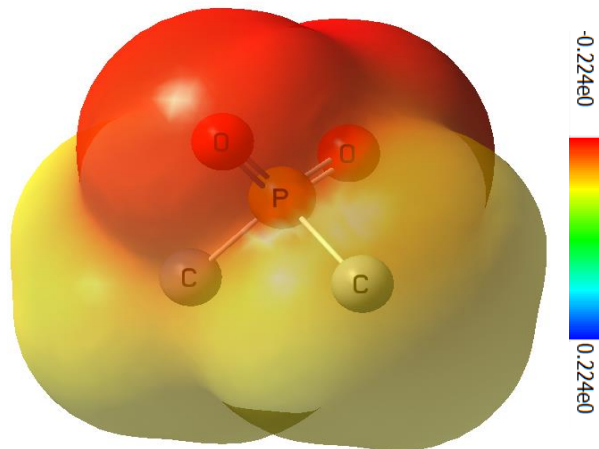


**Figure S29.** MEP plots (computed at iso-density surface value of 0.0004 a.u) of (Me)<sub>2</sub>PO<sub>2</sub><sup>-</sup> calculated at B3LYP/def2-TZVP.

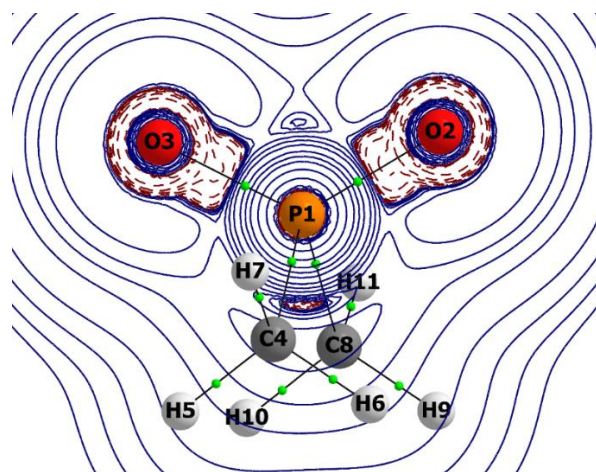


**Figure S30.** Contour plot of Laplacian distribution [ $\nabla^2\rho(r)$ ] in O-P-O of (Me)<sub>2</sub>PO<sub>2</sub><sup>-</sup>. Solid blue lines indicate the areas of charge concentration ( $\nabla^2\rho(r) < 0$ ) while dotted purple lines denotes charge depletion ( $\nabla^2\rho(r) > 0$ ). Solid lines connecting atomic nuclei (black) are the bond paths and green spheres on bond path indicates the BCP.

The important topological parameters at the (3, -1) bond critical points like the electron density [ $\rho(r)$ ] and along with the respective Laplacian [ $\nabla^2\rho(r)$ ] indicate the nature of the

bond. The electron density [ $\rho(r)$ ] at the BCP of P-O [0.229], bond along with the respective Laplacian [ $\nabla^2\rho(r)$ ; 01.177] indicates closed-shell interaction.

**Table S16.** AIM results of the P-O bonds of fragments  $\text{Me}_2\text{PO}_2^-$  at B3LYP/def2-TZVP level of theory. The values in a.u.

Fragment	Bond	$\rho(r)$	$\nabla^2\rho(r)$	Ellipticity
$(\text{Me})_2\text{PO}_2^-$	P1 - O2	+0.229	+1.177	+0.031
	P1 - O3	+0.229	+1.177	+0.031

### S6.3. Optimization, NBO, and AIM analyses of the ligand $(\text{Me})(\text{Cy}-\text{cAl})\text{PO}_2^-$

To study the electronic distribution of  $(\text{Me})(\text{Cy}-\text{cAl})\text{PO}_2^-$ , we conducted NBO analysis of the  $(\text{Me})(\text{Cy}-\text{cAl})\text{PO}_2^-$  ligand. The P–O bonds, were found to have single bond occupancy, with the WBI of both P–O bonds to be 1.10, having a partial double nature. HOMO of  $\text{PO}_2^-$  represents the lone pair on P and O atoms. There is slight extension of the lone pairs of O towards the P atom in HOMO-1 and HOMO-2. Secondary interaction of p orbitals of O atoms can be seen in HOMO-3. HOMO-6 represents the  $\sigma$  type lone pair on N, which further aids the coordination with Co.

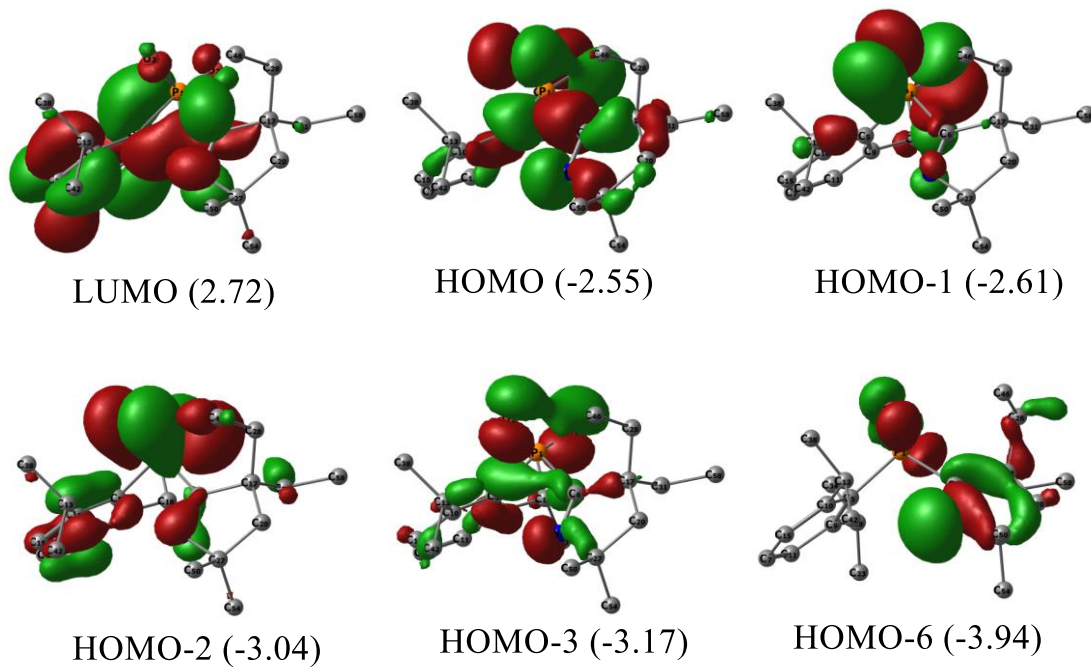


**Figure S31.** Relevant molecular orbitals of the ligand  $(\text{Me})(\text{Cy-cAl})\text{PO}_2^-$ .

**Table S17.** NBO results of the ligand  $(\text{Me})(\text{Cy-cAl})\text{PO}_2^-$  at the B3LYP/def2-TZVP level of theory. Occupation number (ON), polarization and hybridization of the P–O bond.

Ligand	Bond	ON	Polarization and Hybridization (%)		WBI
<b>(Me)(Cy-cAl)PO<sub>2</sub><sup>-</sup></b>	P1-O2	1.99	P: 24.7; s(27.9), p(70.5), d(1.6)	O: 75.3; s(36.4), p(63.5)	1.10
	P1-O3	1.99	P: 24.8; s(28.0), p(70.4), d(1.6)	O: 75.1; s(36.9), p(62.5)	1.10

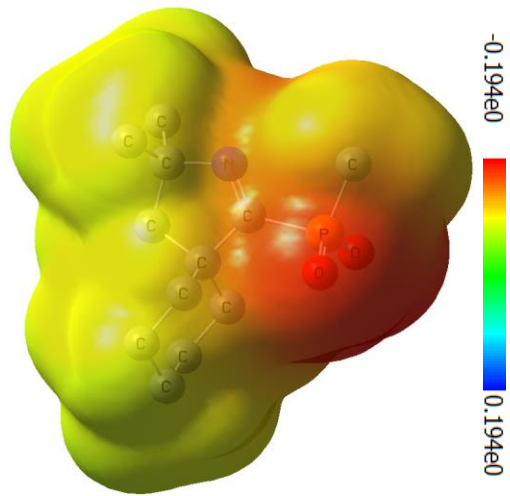


**Figure S32.** MEP plots (computed at iso-density surface value of 0.0004 a.u) of  $(\text{Me})(\text{Cy}-\text{cAl})\text{PO}_2^-$  calculated at B3LYP/def2-TZVP.

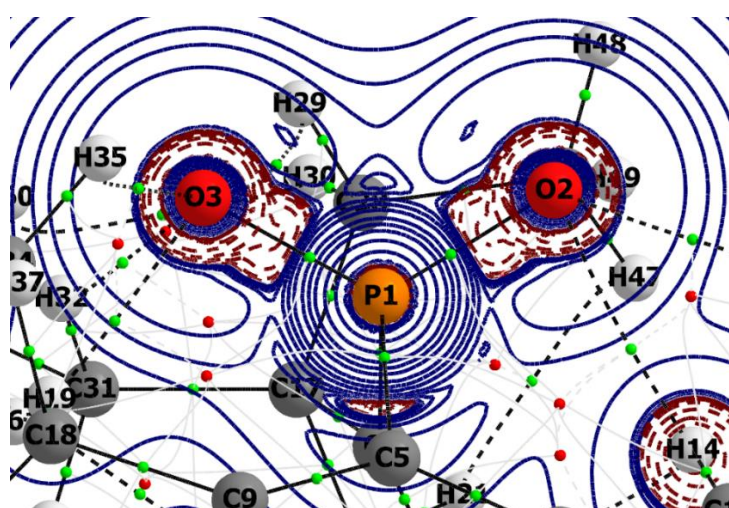


**Figure S33.** Contour plot of Laplacian distribution [ $\nabla^2\rho(r)$ ] in O-P-O of  $(\text{Dipp})(\text{Et}_2-\text{cAl})\text{PO}_2^-$ . Solid blue lines indicate the areas of charge concentration ( $\nabla^2\rho(r) < 0$ ) while dotted purple lines denotes charge depletion ( $\nabla^2\rho(r) > 0$ ). Solid lines connecting atomic nuclei (black) are the bond paths and green spheres on bond path indicates the BCP.

The important topological parameters at the (3, -1) bond critical points like the electron density [ $\rho(r)$ ] and along with the respective Laplacian [ $\nabla^2\rho(r)$ ] indicate the nature of the bond. The electron density [ $\rho(r)$ ] at the BCP of P-O [0.203, 0.202], bond along with the respective Laplacian [ $\nabla^2\rho(r)$ ; 01.42, 1.41] indicates closed-shell interaction.

**Table S18.** AIM results of the P-O bonds of (Me)(Cy-cAl)PO<sub>2</sub><sup>-</sup> at B3LYP/def2-TZVP level of theory. The values are in a.u.

Ligand	Bond	$\rho(r)$	$\nabla^2\rho(r)$	Ellipticity
(Me)(Cy-cAl)PO <sub>2</sub> <sup>-</sup>	P1 – O3	+0.228	+1.169	+0.034
	P1 – O2	+0.229	+1.184	+0.034

#### S6.4. Geometry optimization of 3a'

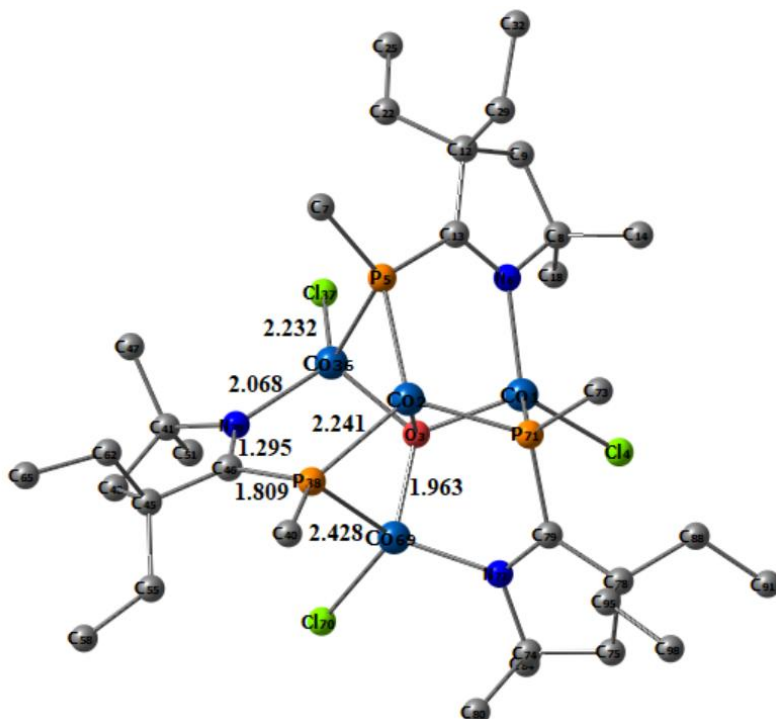


**Figure S34.** Optimized geometry of **3a'** in the septet state at UB3LYP/gen level of theory.

The geometry optimization for **3a** was carried out using the UB3LYP/gen functional for the septet spin state. In these calculations, the def2-SVP basis set was applied to the C, H, and N atoms, while the def2-TZVP basis set was employed for the Co, P, Cl, and O atoms. To reduce computational time, the bulky Dipp group on the P atom was replaced with a Me group, resulting in simplified model complex **3a'**.

**S6.5. Natural bond orbital (NBO) analyses of 3a' (Dipp groups on P atoms of 3a are replaced by the Me groups)**

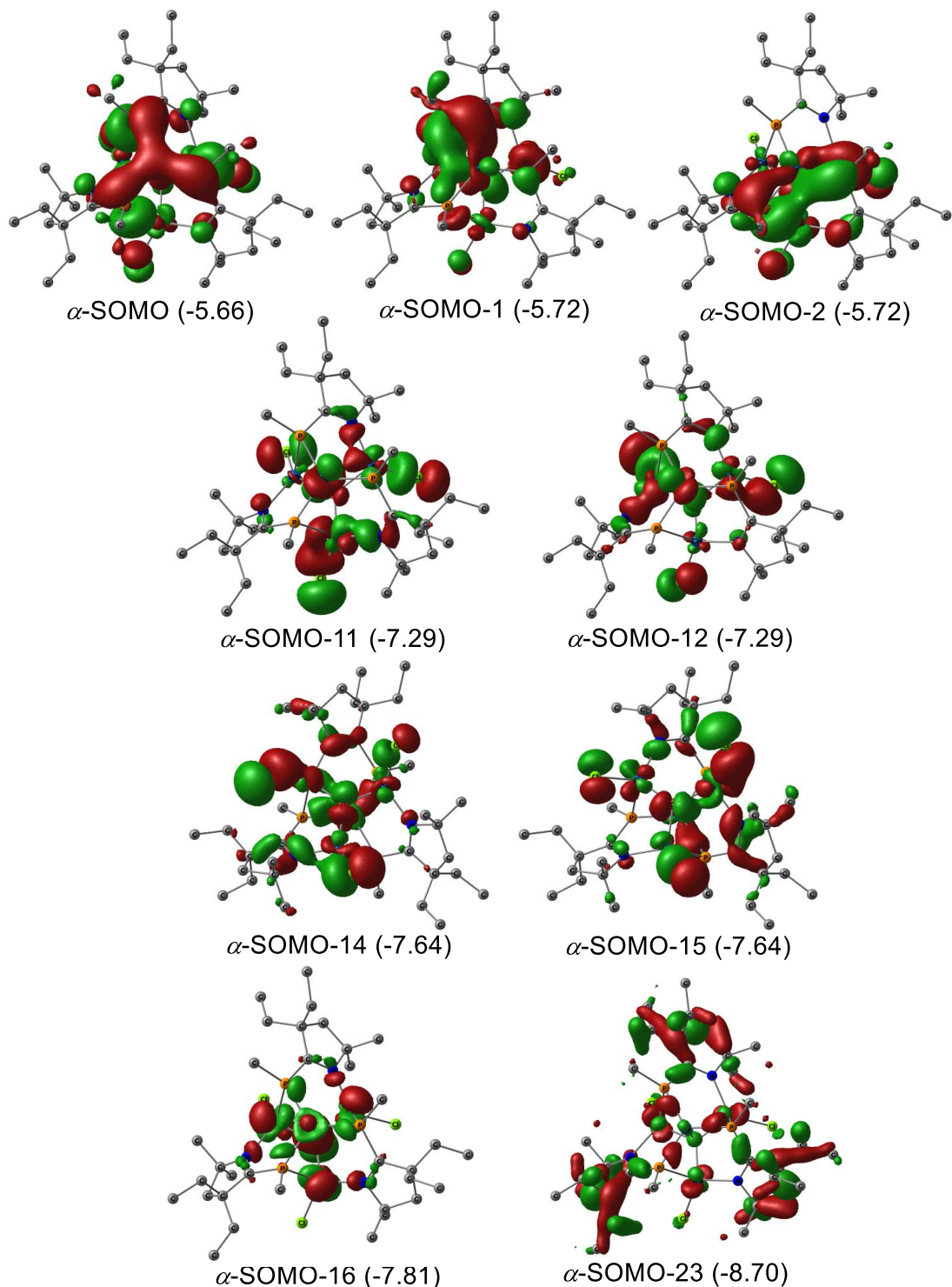


**Figure S35.** Selected Kohn-Sham orbitals of the model complex **3a'** at UB3LYP-D3(BJ)/def2TZVP level of theory.

We have performed natural Bond Orbital (NBO) analysis to understand the electron densities distribution in the model complex **3a'** (where the Dipp groups on P atoms were reduced to Me groups to reduce the computational time) at UB3LYP/def2-TZVP on the coordinates optimized at UB3LYP/gen in septet state where def2-SVP was used for C, H and N atoms and def2-TZVP was used for Co, P, Cl and O atoms.

The representative Kohn-Sham orbitals revealed that the  $\alpha$ -SOMO corresponds to the delocalization of electrons over the Co ions, and the bridging O atom at the axial position along with the P atoms on the periphery. The  $\mu_4$ -O atom was clearly seen to show orbital overlap between the three peripheral Co(II) ions, and the central Co(II) ion, presumably exhibiting a magnetic super-exchange pathway. The Co-P interactions exhibit a significant 3-center bonding character, where the electron density is found to be delocalized between the cobalt atoms at the periphery (Co<sub>periphery</sub>) and the phosphorus atom (P), extending towards the axial cobalt center (Co<sub>axial</sub>). The  $\alpha$ -SOMO-1 and  $\alpha$ -SOMO-2 orbitals confirm this Co<sub>periphery</sub>-P-Co<sub>axial</sub> delocalization, with the major electron contribution arising from the P p-orbital (75.6%), indicating a strong  $\pi$ -type interaction with cobalt. This highlights the ligand-centered electronic contribution, where phosphorus serves as the primary electron reservoir, coordinating with cobalt through a highly polarized bonding framework. Additionally, the absence of direct Co-Co bonding interactions is evident from the NBO analysis, where the computed orbitals do not show any significant overlap or delocalization between the Co centers. This suggests that the metal-metal interactions are negligible, and the structural stability of the Co<sub>4</sub> cluster (**3a**) is largely driven by the strong Co-P bonding, rather than the Co-Co interactions.

The C-P bond in complex **3a'** exhibits  $\sigma$ -type bonding characteristics, as reflected in  $\alpha$ -SOMO-23, and the bond is more polarized towards C (61.5%).

The  $\alpha$ -SOMO-11 and  $\alpha$ -SOMO-12 show the  $\sigma$ -type interaction between Co and the p-type lone pair on N atom, where the bond is more polarized towards N (92.4). The  $\alpha$ -SOMO-16 corresponds to the  $\sigma$ -type interaction between the p orbitals of O atom (83.5%) and the d orbital of Co atom in the axial position.  $\alpha$ -SOMO-23 shows the  $\sigma$ -type interaction between the C and P atoms.

In addition, the  $\alpha$ -SOMO-14 and  $\alpha$ -SOMO-15 exhibit  $\sigma$ -type interactions between the d-orbitals of the peripheral Co atoms and the p-orbitals of oxygen, further stabilizing the coordination environment.

**Table S19.** NBO results of the complex **3a'** at UB3LYP-D3(BJ)/def2-TZVP level of theory, Occupation Number (ON)

Bond	ON	Polarization and Hybridization (%)		
Co <sub>1</sub> -Co <sub>2</sub> -P <sub>71</sub>	0.92	Co: 10.8 s(22.6), p(77.3)	Co:13.6 s(0.3), p(52.2), s (10.1), p(89.7) d(47.5)	P: 75.6
Co <sub>2</sub> -O <sub>3</sub>	0.96	Co:16.5 s (15.3) p (21.8), d(62.9)		O:83.5 s(41.6) p (58.4)
Co <sub>1</sub> -N <sub>6</sub>	0.97	Co:7.6 s (29.2) p (70.1)		N:92.4 s (31.8) p (68.1)
Co <sub>2</sub> -P <sub>71</sub>	0.94	Co: 30.0 s (28.0) p (40.1)		P:70.0 s (34.6) p (65.1)
P <sub>5</sub> -C <sub>13</sub>	0.98	P:38.5 s (27.1) p (72.6)	C:61.5 s (31.8) p (67.9)	

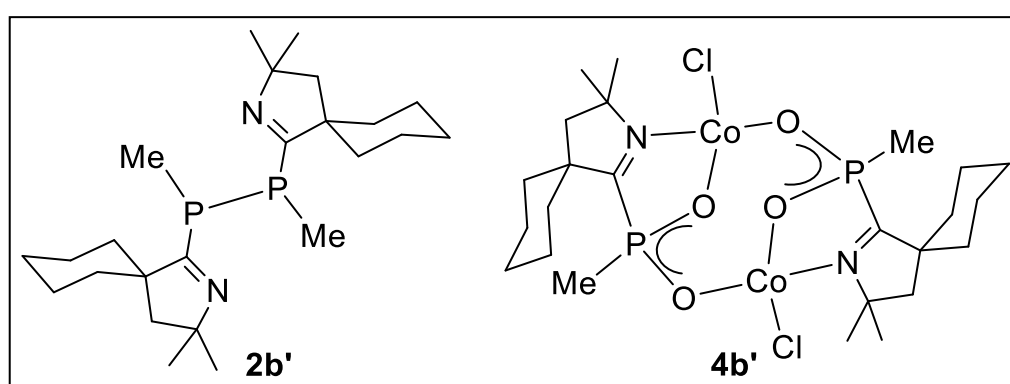


**Figure S36.** Molecular structures of the model molecules **2b'**, **4b'**. Dipp groups (Dipp = 2,6-diisopropylphenyl) of the experimental molecules **2b**, **4b** are replaced by Me.

## S6.6. Geometry optimization of compound 2, and complex 4

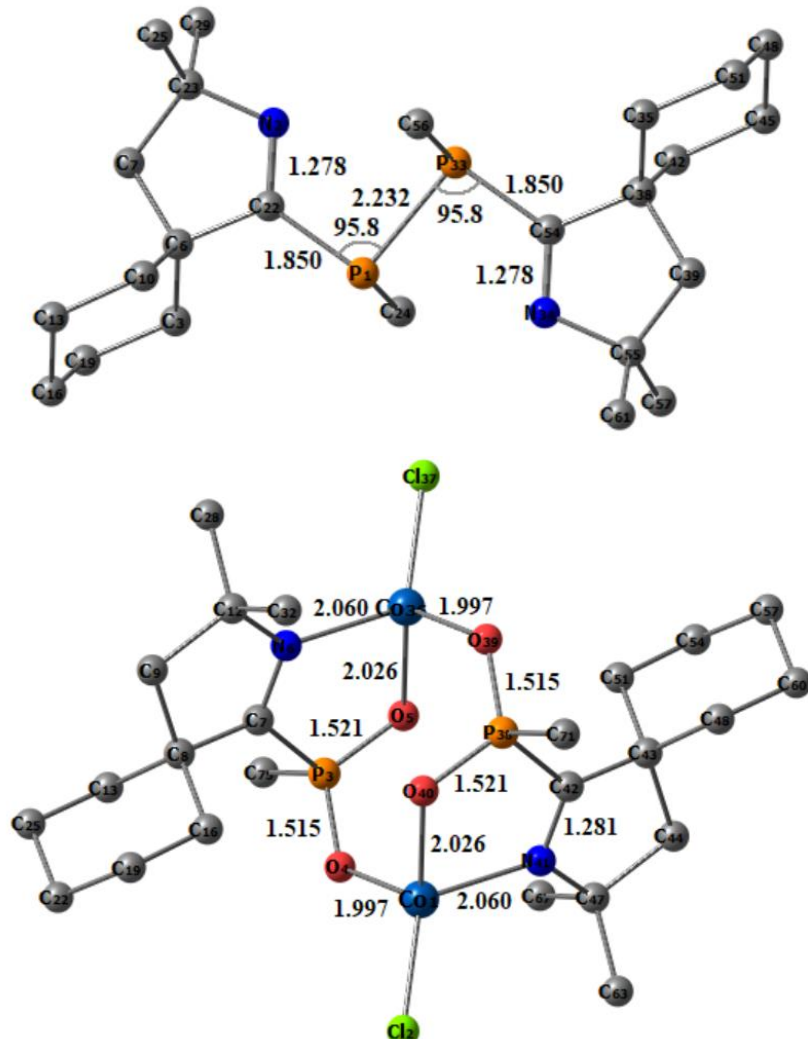


**Figure S37.** Optimized geometries of compound **2'** (at B3LYP/gen level of theory), and complex **4b'** (at ROB3LYP/gen level of theory) in the singlet state, and in the septet state, respectively.

To understand the electron densities distribution, and bonding situation, we first performed the geometry optimization of the model molecules **2b'**, and **4b'** at B3LYP/gen, and ROB3LYP/gen levels of theories, respectively; where def2-SVP was used for C, H and N atoms and def2-TZVP was used for Co, P, Cl and O atoms establishing the septet spin for both the species. The Dipp group on P atom was reduced to Me (**2b'** and **4b'**) to reduce the computational time. The calculated bond parameters were found to be well in agreement with the experimentally observed values. The calculated bond parameters were in well agreement with the experimentally observed structures. The bond between C-P is 1.850 Å which in the range of C-P single bond. This observation is in contract with the bond length of C-P

observed in cAAC<sub>2</sub>P<sub>2</sub> (1.719(7) Å),<sup>15</sup> which is significantly shorter in comparison with **2b**. The P atoms exhibits a trigonal pyramidal geometry indicating the presence of lone pair on the atom. This can be visualized in the HOMO of **2b'** (Figure S37). The bond length of P-P bond is 2.232 Å which slightly longer than P-P bond observed in cAAC<sub>2</sub>P<sub>2</sub> (2.184(3) Å). The bond between C-P in complex **4b'** is 1.843 Å which slightly shorter than the **2** (1.850 Å). The bond length of Co-N and Co-O are 2.060 Å and 1.997/2.026 Å respectively. Co-N bond length is in well agreement with the bond lengths overserved in the reported N-Heterocyclic carbene bonded cobalt porphyrin complexes (1.918(2), 1.914(3), 1.923(3) and 1.911(3) Å).<sup>16</sup>

### S6.7. NBO analyses of compound **2b'**, and complex **4b'**

**Table S20.** NBO results of compound **2b'** at the B3LYP/def2-TZVP level of theory. Occupation number (ON), polarization and hybridization of the C–P, P–O and Co–O bonds.

Complex	Bond	ON	Polarization and Hybridization (%)		WBI
<b>2b'</b>	P1-C22	1.96	P: 37.1; s(15.6), p(83.7)	C: 62.9; s(30.8), p(68.9)	0.94
	P1-P33	1.94	P: 50; s(12.1), p(87.1)	P: 50; s(12.1), p(87.1)	0.94
	P1/P33 Lone pair	1.91	s(55.9), p(43.9)		

The NBO analysis conducted on bis-phosphene **2b'** reveals the absence of two bonding occupancies for C-P bond as observed in cAAC<sub>2</sub>P<sub>2</sub>. The C-P bond is singly occupied and is polarized towards C (62.9%) with a WBI of 0.94 which indicates the single bond nature of C-P bond. The bond between P-P has a single bond character with a WBI of 0.94, which is composed of a majorly π character (Figure S38, HOMO-1). The LUMO of **2b'** is the π\* of C=N. The presence of lone pair on the P atom can also be visualized on both P atoms (Figure S38, HOMO).

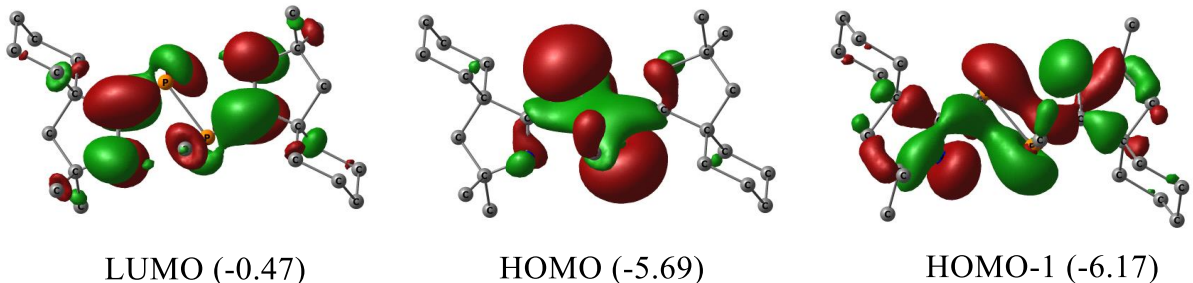


**Figure S38.** Relevant molecular orbitals of compound **2b'**, calculated at B3LYP/def2-TZVP level of theory (energies given in the parenthesis are in eV).

The NBO analysis was conducted on the model system **4b'** (all Dipp groups are replaced by the Me groups to save the computational time) at UB3LYP/def2-TZVP at level of theory. It was observed that two of the 3d orbitals on Co are doubly occupied, while three d orbitals are singly occupied. The  $\beta$ -LUMO can be viewed as the interaction involving the donation of the 3d electrons from Co to the vacant C=N  $\pi^*$ -MO, resulting in the slight elongation of the C-N bond compared to **2b'**. On the other hand, the  $\alpha$ -LUMO is found to be localized on the C=N bond. Additionally,  $\alpha$ -SOMO-4,  $\alpha$ -SOMO-5, and  $\alpha$ -SOMO-7 represent the  $\sigma$  type interaction between Cl, N, O atoms, and Co atoms, respectively. Furthermore, the  $\pi$ -type interaction existing between the C=N bond can be visualized in  $\alpha$ -SOMO-9. The unpaired d orbital electrons are represented in  $\alpha$ -SOMO,  $\alpha$ -SOMO-1,  $\alpha$ -SOMO-2, and  $\alpha$ -SOMO-3 (Figure S39).

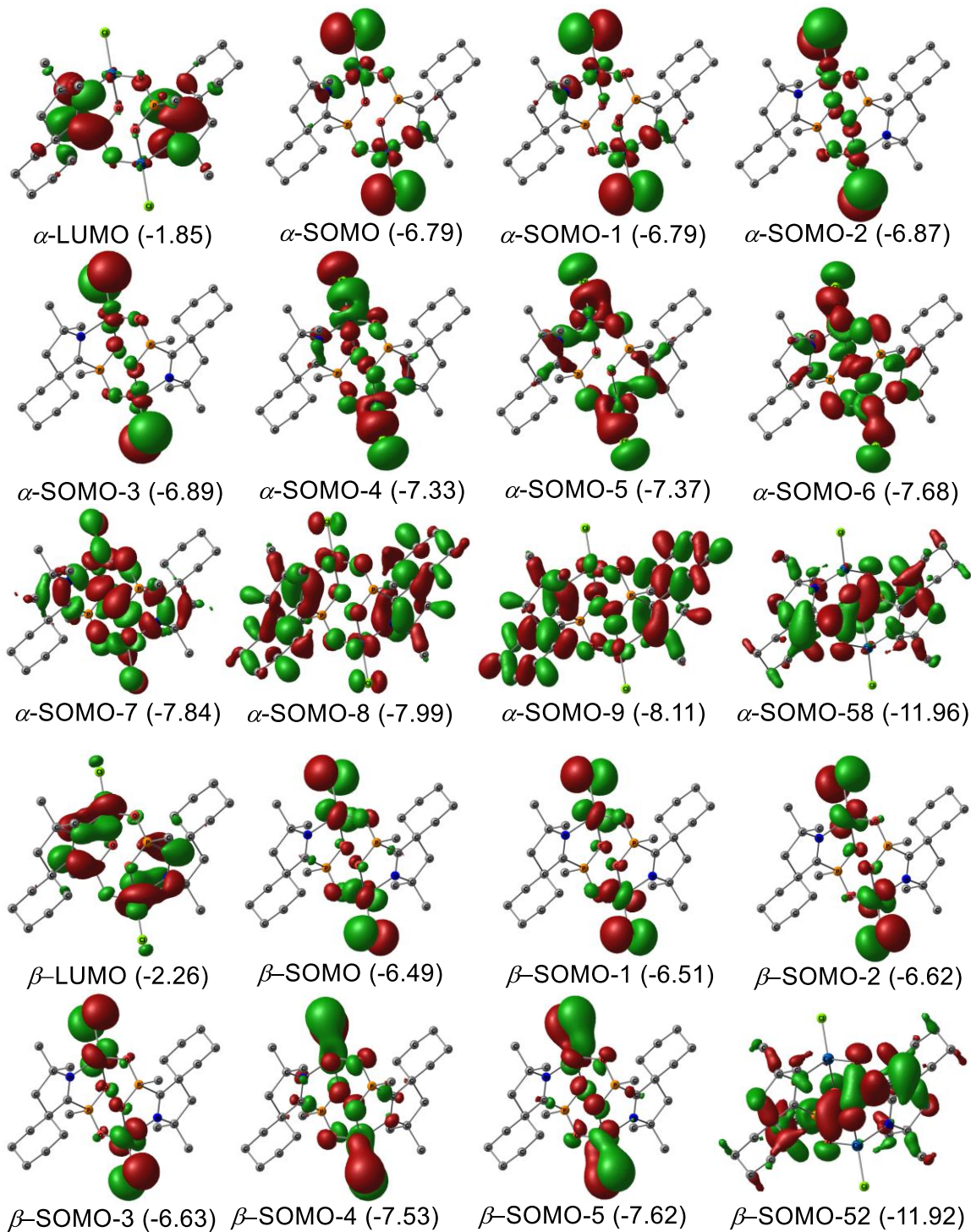


**Figure S39.** Plot of important Kohn-Sham orbitals of complex **4b'** at UB3LYP/def2-TZVP at level of theory.

## S6.8. QTAIM analyses of complexes 3a' and 4b'

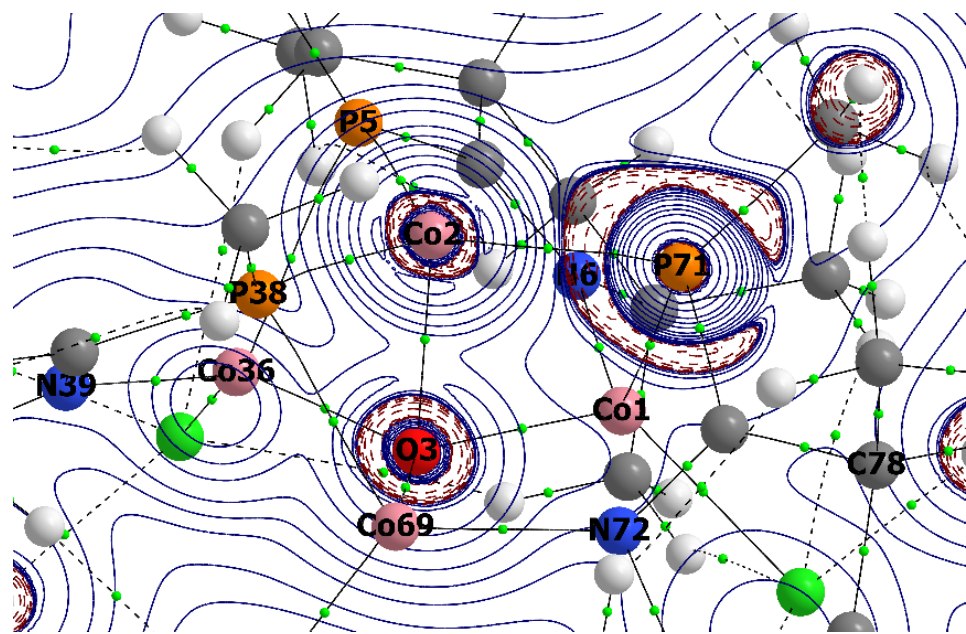


**Figure S40.** Contour plot of Laplacian distribution [ $\nabla^2\rho(r)$ ] in the O3–Co2–P71 plane of **3a'**. Solid blue lines indicate the areas of charge concentration ( $\nabla^2\rho(r) < 0$ ) while dotted purple lines denotes charge depletion ( $\nabla^2\rho(r) > 0$ ). Solid lines connecting atomic nuclei (black) are the bond paths and green spheres on bond path indicates the BCP.

**Table S21.** AIM results of **3a'** at UB3LYP/def2-TZVP level of theory. The values are in a.u.

Bond	$\rho(r)$	$\nabla^2\rho(r)$	$V_b$	$G_b$
Co2-O3	0.072	0.302	-0.108	0.092
Co1-O3	0.087	0.438	-0.147	0.128
Co2-P71	0.084	0.148	-0.099	0.068
Co1-P71	0.062	0.110	-0.060	0.044

In the QTAIM analysis<sup>17</sup> of the model system **3a'** (all Dipp groups of **3a** have been replaced by the Me groups to save the computational time), distinct bond critical points (BCPs) were identified for each Co–O and Co–P interaction, and their topological parameters highlight differences in bond strength and character. The Co1–O3 BCP

exhibits the highest electron density ( $\rho \approx 0.087$  a.u.) and the most negative potential energy density ( $V_b \approx -0.147$  a.u.), indicating a relatively stronger, more stabilized bond, whereas the Co1–P71 BCP has the lowest  $\rho$  ( $\approx 0.062$  a.u.) and a less negative  $V_b$  ( $\approx -0.060$  a.u.), consistent with a weaker interaction. All the bonds show a positive Laplacian ( $\nabla^2\rho > 0$ ) at the BCP, signifying that electron density is locally depleted in the bonding region – a hallmark of predominantly closed-shell (ionic or dative) interactions. The Laplacian contour plot of the  $\text{Co}_4$  system (Figure S39) visually reinforces these findings by showing regions of charge concentration ( $\nabla^2\rho < 0$ , solid blue contours) along the Co–O and Co–P bond paths and charge depletion ( $\nabla^2\rho > 0$ , dotted purple contours) elsewhere, highlighting the polar nature of the bonding. Furthermore, the QTAIM molecular graph displays bond paths (black lines) connecting the Co atoms with the O and P ligands, each terminating in a BCP (green sphere), thereby confirming the presence and connectivity of these bonding interactions in the molecule. However, the presence of bond path is not observed for Co–Co bond (Figure S40).

**Table S22.** AIM results of the selected bonds of **4b'** at UB3LYP/def2-TZVP level of theory. The values are in a.u.

Bond	$\rho(r)$	$\nabla^2\rho(r)$	Ellipticity
Co1 - O40	+0.071	+0.366	+0.331
Co1 - Cl2	+0.082	+0.272	+0.023
Co1 - O4	+0.075	+0.407	+0.209
P3 - O4	+0.221	+1.085	+0.043
P3 - O5	+0.219	+1.049	+0.023

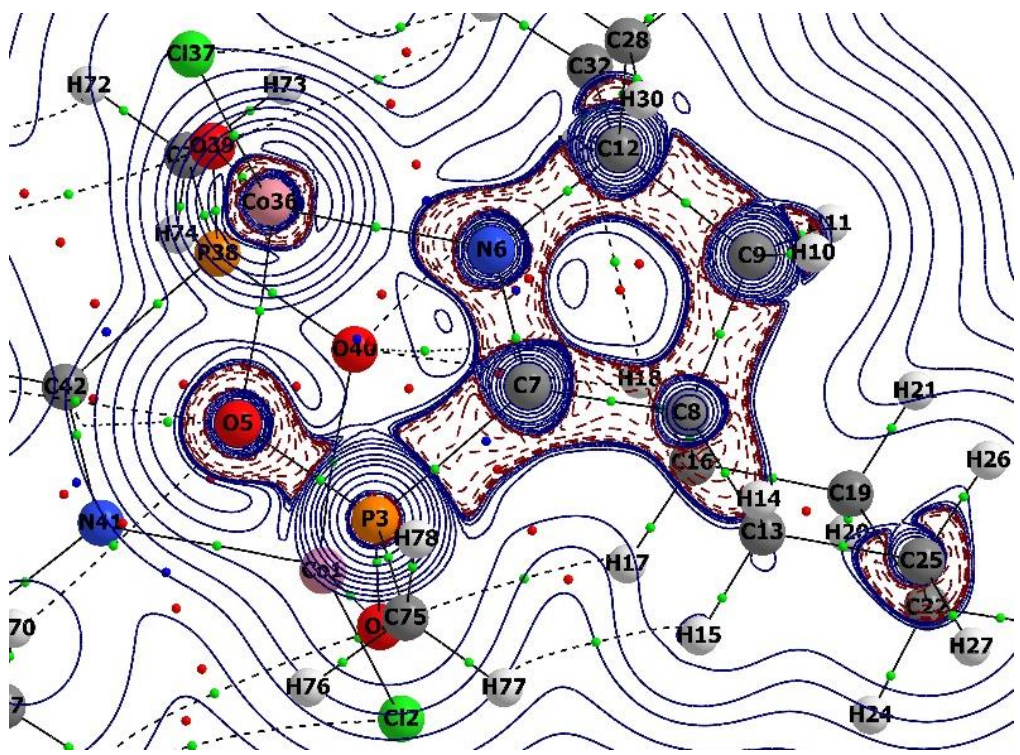


**Figure S41.** Contour plot of Laplacian distribution  $[\nabla^2\rho(r)]$  in Co-O-P of **4b'**. Solid blue lines indicate the areas of charge concentration ( $\nabla^2\rho(r) < 0$ ) while dotted purple lines denotes charge depletion ( $\nabla^2\rho(r) > 0$ ). Solid lines connecting atomic nuclei (black) are the bond paths and green spheres on bond path indicates the BCP.

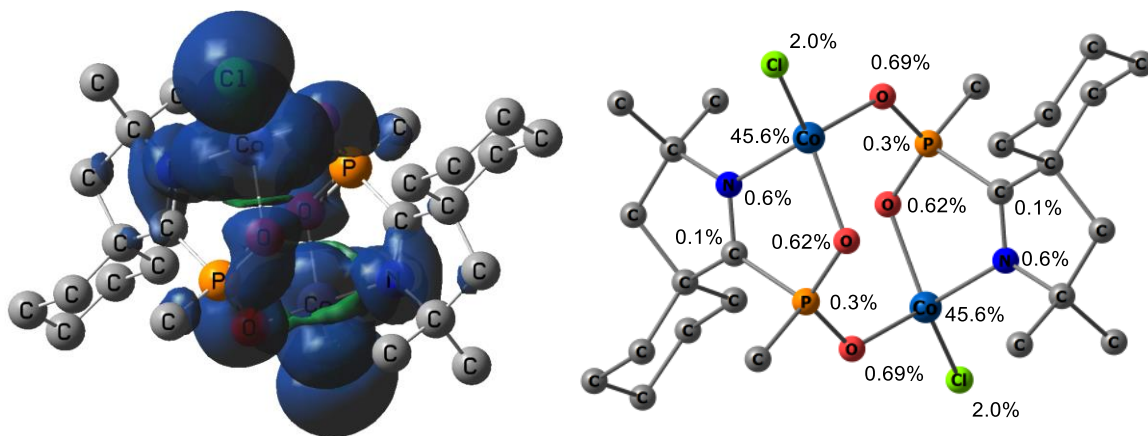


**Figure S42.** Mulliken  $\alpha$ - (blue),  $\beta$ -spin (green) densities of  $[(\text{Dipp})(\text{Et}_2\text{cAl})\text{P}(\text{CoCl})_3]\text{CoO}$  (**4b'**) at  $S = 3$  (computed at UB3LYP-D3(BJ)/def2-TZVP level of theory).

The  $\alpha$ -spin density plot exhibits the strong delocalization of the positive spin density (blue) over the Cl, Co, N and O-P-O atoms.

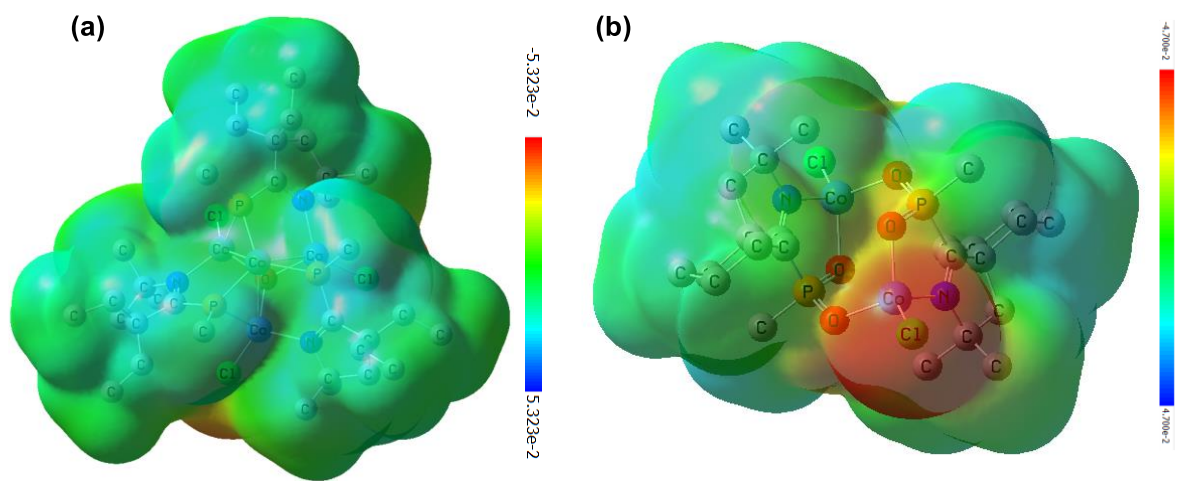


**Figure S43.** Molecular Electrostatic Potential (MEP) plot of complexes **3a'** (a), and **4b'** (b) at UB3LYP-D3(BJ)/def2TZVP level of theory.

#### Coordinates:

##### **PO<sub>2</sub><sup>-</sup>**

15	0.000000000	0.000000000	0.397236000
8	0.000000000	1.295786000	-0.372408000
8	0.000000000	-1.295786000	-0.372408000

##### **NO<sub>2</sub><sup>-</sup>**

N	0.000000000	0.000000000	0.461310000
O	0.000000000	1.068701000	-0.201823000
O	0.000000000	-1.068701000	-0.201823000

##### **(Me)<sub>2</sub>PO<sub>2</sub><sup>-</sup>**

15	0.000000000	0.000000000	0.221127000
8	0.000000000	1.315465000	0.943540000
8	0.000000000	-1.315465000	0.943540000
6	1.434572000	0.000000000	-0.949616000
1	1.432042000	-0.893274000	-1.579612000
1	1.432042000	0.893274000	-1.579612000
1	2.347502000	0.000000000	-0.349847000
6	-1.434572000	0.000000000	-0.949616000
1	-1.432042000	0.893274000	-1.579612000

1	-1.432042000	-0.893274000	-1.579612000
1	-2.347502000	0.000000000	-0.349847000

**(Me)(Cy-cAl)PO<sub>2</sub><sup>-</sup>**

15	-1.800579000	-1.415239000	-0.007523000
8	-1.306212000	-2.220873000	-1.175329000
8	-1.779662000	-1.962703000	1.389082000
7	-1.293276000	1.306397000	-0.006440000
6	-3.466905000	-0.759784000	-0.380296000
6	-0.781681000	0.132489000	0.033102000
6	1.075126000	1.580838000	0.382749000
1	1.922622000	1.956274000	-0.211163000
1	1.341789000	1.719084000	1.443080000
6	-0.243793000	2.340934000	0.065091000
6	-0.191248000	3.063821000	-1.289714000
1	-1.185410000	3.465950000	-1.540570000
1	0.533503000	3.895617000	-1.270317000
1	0.101005000	2.367782000	-2.090246000
6	-0.621184000	3.335502000	1.168711000
1	-0.716672000	2.812670000	2.133087000
1	0.141525000	4.126586000	1.272686000
1	-1.590856000	3.807331000	0.943875000
6	0.752722000	0.088182000	0.106656000
6	1.313152000	-0.403049000	-1.253505000
6	1.251044000	-0.852111000	1.223772000
6	2.836256000	-0.563501000	-1.246908000
1	1.007511000	0.296309000	-2.049033000
1	0.822696000	-1.361945000	-1.483555000
6	2.776545000	-0.983461000	1.238817000
1	0.875843000	-0.492181000	2.195000000
1	0.791655000	-1.842034000	1.080351000
6	3.299244000	-1.481905000	-0.111955000
1	3.323561000	0.423260000	-1.130188000
1	3.173236000	-0.959060000	-2.221316000

1	3.087335000	-1.669316000	2.046354000
1	3.239408000	-0.004410000	1.467379000
1	4.401401000	-1.561071000	-0.100804000
1	2.906977000	-2.498997000	-0.291654000
1	-3.483994000	-0.274458000	-1.366849000
1	-4.166313000	-1.610736000	-0.380795000
1	-3.773883000	-0.031972000	0.383456000

### 3a'

Co	-1.456687084	1.308840618	-0.684844061
Co	-0.000052026	0.000021980	1.248696088
O	-0.000080084	-0.000129009	-0.822505067
Cl	-1.672533817	3.028347519	-2.091959164
P	-1.699242789	-1.459357810	1.318949094
N	-3.111750860	0.125535769	-0.313848030
C	-2.035968248	-2.771395531	2.549222188
C	-4.380930410	0.362038607	-1.059462087
C	-5.269627258	-0.839818206	-0.659295055
H	-5.290457776	-1.550835247	-1.493265123
H	-6.307490489	-0.538066993	-0.462303041
C	-4.604096357	-1.500986200	0.570547035
C	-3.198550825	-0.893700748	0.480443031
C	-4.956420405	1.719705814	-0.637999052
H	-5.894850400	1.913704480	-1.179542094
H	-4.250376144	2.527852344	-0.879593073
H	-5.169398457	1.748040346	0.441388028
C	-4.084353889	0.342623682	-2.563517203

H	-5.031533057	0.396755718	-3.123302244
H	-3.566985950	-0.589363938	-2.835676221
H	-3.459384239	1.195670639	-2.860648222
C	-4.582473773	-3.053050815	0.498664032
H	-3.696854556	-3.359941033	-0.079540012
H	-4.448809182	-3.446424667	1.517757107
C	-5.807483501	-3.725387227	-0.127572016
H	-5.727685953	-4.818269318	-0.017630007
H	-5.880834400	-3.518703775	-1.204913101
H	-6.753004445	-3.412624798	0.337787020
C	-5.206742856	-0.983317598	1.908488142
H	-4.535414659	-1.279854780	2.731156200
H	-5.183848055	0.118099697	1.889409137
C	-6.622530767	-1.452210059	2.238379165
H	-6.981282937	-0.959617966	3.155675233
H	-6.666495395	-2.537732184	2.409750179
H	-7.334597758	-1.209293095	1.434382104
Co	-0.405279588	-1.916130287	-0.684532058
Cl	-1.786258426	-2.962926320	-2.091777164
P	2.113368829	-0.741832074	1.318886095
N	1.447177568	-2.757753236	-0.313583030
C	3.418225483	-0.376782646	2.548656191
C	1.876937848	-3.975274947	-1.058997089
C	3.362181776	-4.143783499	-0.658997054

H	3.988228550	-3.806541040	-1.493145121
H	3.619851090	-5.193412505	-0.461743041
C	3.602112370	-3.236528336	0.570618040
C	2.373304123	-2.323123038	0.480549031
C	0.989076549	-5.152480084	-0.637142055
H	1.290099086	-6.062198842	-1.178762098
H	-0.063914263	-4.945133023	-0.878364075
H	1.071429611	-5.351073045	0.442222027
C	1.745276971	-3.709093891	-2.563101201
H	2.171963652	-4.556544357	-3.122746242
H	2.293665228	-2.795094247	-2.835512224
H	0.693998224	-3.594479507	-2.860137222
C	4.935343609	-2.441582837	0.498483032
H	4.758011312	-1.520980982	-0.079323012
H	5.209610594	-2.129473063	1.517577108
C	6.129890085	-3.166034825	-0.128482016
H	7.036622601	-2.550809090	-0.018123007
H	5.987425726	-3.331998649	-1.205941096
H	6.331548051	-4.141693117	0.336077020
C	3.455496860	-4.017144642	1.908687139
H	3.376737616	-3.287417010	2.731300205
H	2.490246961	-4.548128687	1.889856139
C	4.569696836	-5.008620539	2.238322167
H	4.322989063	-5.565375014	3.155893233

H	5.531800623	-4.503776273	2.409057179
H	4.715046760	-5.746951974	1.434454104
Co	1.861798468	0.607021614	-0.684759059
Cl	3.458948144	-0.065404379	-2.091945168
P	-0.414439134	2.201216888	1.318859097
N	1.664632100	2.631984319	-0.313548030
C	-1.382890041	3.148945300	2.548577190
C	2.504413306	3.612839058	-1.058784089
C	1.907879307	4.983414419	-0.658789056
H	1.302949002	5.357057881	-1.493010123
H	2.688101222	5.731281183	-0.461413042
C	1.001997941	4.737654408	0.570671037
C	0.825198584	3.216794687	0.480568031
C	3.967734516	3.432167996	-0.636704055
H	4.605314909	4.147782047	-1.177947096
H	4.314523036	2.416587467	-0.878187071
H	4.098345489	3.602361412	0.442749028
C	2.339976598	3.365915740	-2.562951200
H	2.860854041	4.159116019	-3.122375247
H	1.274307484	3.384107685	-2.835645222
H	2.766198646	2.398116435	-2.860020227
C	-0.352973814	5.494958562	0.498312032
H	-1.061667793	4.881090092	-0.079405012
H	-0.760417213	5.576669456	1.517376110

C	-0.322576623	6.891584007	-0.128861016
H	-1.308643605	7.369446144	-0.018574008
H	-0.107619322	6.850985687	-1.206313097
H	0.421684158	7.553959720	0.335616019
C	1.751122078	5.000943162	1.908854142
H	1.158330220	4.567992805	2.731383201
H	2.693540138	4.430406895	1.890254138
C	2.052773113	6.461587486	2.238493165
H	2.657881275	6.526275013	3.156338234
H	1.134530092	7.042537426	2.408765179
H	2.619977970	6.956487808	1.434863105
H	3.540709246	-1.177446229	3.290911247
H	4.385463110	-0.163928414	2.077399154
H	3.080138319	0.528750499	3.073290231
H	-2.335435167	-3.715603634	2.078338153
H	-1.082899109	-2.931410868	3.074180228
H	-2.790681137	-2.476622038	3.291198247
H	-1.997700986	2.403508423	3.073798231
H	-0.750606526	3.655840371	3.290382245
H	-2.051127933	3.879809350	2.077153150

## 2b'

15	-0.779046000	-0.798853000	-0.009670000
7	-2.071907000	1.616984000	-0.200678000
6	-3.984325000	-1.267513000	-1.129029000

6	-3.675860000	-0.143065000	-0.121555000
6	-4.425838000	1.176747000	-0.436492000
6	-3.970785000	-0.669368000	1.308047000
6	-5.396126000	-1.210966000	1.455736000
6	-5.702650000	-2.288706000	0.411796000
6	-5.421772000	-1.780730000	-1.005520000
6	-2.220436000	0.347860000	-0.186173000
6	-3.377966000	2.305547000	-0.223095000
6	-0.572732000	-1.337493000	-1.774385000
6	-3.557135000	3.034707000	1.116329000
6	-3.369618000	3.317114000	-1.372664000
15	0.779028000	0.798837000	0.009909000
7	2.071940000	-1.616926000	0.201558000
6	3.984570000	1.267950000	1.128319000
6	3.675876000	0.143097000	0.121371000
6	4.425930000	-1.176584000	0.436653000
6	3.970488000	0.668826000	-1.308508000
6	5.395802000	1.210351000	-1.456724000
6	5.702558000	2.288520000	-0.413296000
6	5.421989000	1.781121000	1.004288000
6	2.220465000	-0.347802000	0.186509000
6	3.378006000	-2.305466000	0.223938000
6	0.572758000	1.337604000	1.774567000
6	3.556857000	-3.035144000	-1.115245000
6	3.369932000	-3.316596000	1.373896000

#### 4b'

27	0.144915000	-2.277544000	-0.257427000
17	0.713007000	-4.324612000	-0.828225000
15	1.064392984	-0.084249486	1.716193893
8	1.015358016	-1.563136514	1.391337107
8	-0.219365000	0.711598000	1.540604000
7	1.842424000	1.795716000	0.004885000
6	2.262982000	0.728068000	0.575362000

6	3.635827000	0.261860000	0.129341000
6	4.108425000	1.513951000	-0.663983000
6	2.834513000	2.352492000	-0.948914000
6	4.560056000	-0.086790000	1.314717000
6	3.484429000	-0.999969000	-0.767785000
6	4.837943000	-1.539367000	-1.237089000
6	5.770096000	-1.827587000	-0.057140000
6	5.924416000	-0.597771000	0.842691000
6	3.014750000	3.841155000	-0.646768000
6	2.287731000	2.149411000	-2.368882000
27	-0.144849000	2.277618000	0.257546000
17	-0.712905000	4.324700000	0.828330000
15	-1.064331000	0.084323000	-1.716074000
8	-1.015307000	1.563210000	-1.391210000
8	0.219434000	-0.711514000	-1.540477000
7	-1.842373000	-1.795671000	-0.004803000
6	-2.262934000	-0.728020000	-0.575275000
6	-3.635863000	-0.261912000	-0.129400000
6	-4.108425000	-1.514004000	0.663944000
6	-2.834491000	-2.352493000	0.948940000
6	-4.560004000	0.086586000	-1.314892000
6	-3.484680000	0.999986000	0.767671000
6	-4.838292000	1.539293000	1.236795000
6	-5.770342000	1.827365000	0.056727000
6	-5.924459000	0.597481000	-0.843044000
6	-3.014655000	-3.841157000	0.646759000
6	-2.287805000	-2.149425000	2.368949000
6	-1.680132000	-0.135539000	-3.387516000
6	1.680202984	0.135620514	3.387632893

## S6.9. *Ab initio* calculations on Co<sub>4</sub> cluster 3a

### S6.9.1. Description of the computational study

The structure of **3a** was taken from the corresponding CIF file.

We calculated the entire Co<sub>4</sub>, as it is in the CIF file, labelled **Co4-R0** as well as a reduced version **Co4-R1**, in which the large substituents (*i*Pr = -CH(CH<sub>3</sub>)<sub>2</sub>) of the benzene rings are replaced by H.

1) **Co4-R0** = Co<sub>4</sub>P<sub>3</sub>N<sub>3</sub>O<sub>1</sub>C<sub>66</sub>H<sub>105</sub>, 185 atoms

2) **Co4-R1** = Co<sub>4</sub>P<sub>3</sub>N<sub>3</sub>O<sub>1</sub>C<sub>30</sub>H<sub>33</sub>, 77 atoms

All DFT calculations were carried out using ORCA 5.0.4 and used the following common options:

Def2-SVP basis on all atoms

UKS VeryTightSCF DEFGRID3

FrozenCore = FC\_NONE

FiniteNuc = true

Picturechange = true

The following DFT functionals were used:

B3LYP PBE wB97 TPSS0

### S6.9.2. Ground state optimization for the Co<sub>4</sub> molecule

**Table S23.** Ground state total energy for different spin multiplicities (a.u.) for **Co<sub>4</sub>-R1**.

DFT	Spin	Absolute Energy (a.u.)	Relative Energy (a.u.)	Relative Energy (cm <sup>-1</sup> )
B3LYP	S=0	-9334.42962575	0.10014258	21978.76
	S=1	-9334.46592832	0.06384002	14011.27
	S=2	-9334.49811198	0.03165636	6947.77
	S=3	-9334.52976834	0.00000000	0.00
	S=4	-9334.49742180	0.03234654	7099.25
	S=5	-9334.49499295	0.03477539	7632.32
	S=6	-9334.51472471	0.01504363	3301.70
PBE	S=0	-9332.26899171	0.00079261	173.96
	S=1	-9332.23514647	0.03463785	7602.13
	S=2	-9332.25311285	0.01667146	3658.96
	S=3	-9332.26978431	0.00000000	0.00
	S=4	-9332.25069824	0.01908608	4188.91
	S=5	-9332.24598531	0.02379901	5223.28
	S=6	-9332.24768742	0.02209690	4849.71
TPSS0	S=0	-9335.84853042	0.11586387	25429.19
	S=1	-9335.88777593	0.07661836	16815.79
	S=2	-9335.92622945	0.03816483	8376.22
	S=3	-9335.96439429	0.00000000	0.00
	S=4	-9335.92619466	0.03819963	8383.85
	S=5	-9335.92503532	0.03935897	8638.30
	S=6	-9335.95203325	0.01236104	2712.94
wB97	S=0	-9335.98416307	0.12668052	27803.17
	S=1	-9336.04447593	0.06636765	14566.02
	S=2	-9336.02070360	0.09013999	19783.45
	S=3	-9336.11084358	0.00000000	0.00
	S=4	-9336.07656272	0.03428086	7523.78
	S=5	-9336.07442488	0.03641870	7992.98
	S=6	-9336.09898547	0.01185811	2602.56

**Table S24.** Ground state total energy for different spin multiplicities (a.u.) for **Co<sub>4</sub>-R0**.

DFT	Spin	Absolute Energy (a.u.)	Relative Energy (a.u.)	Relative Energy (cm <sup>-1</sup> )
B3LYP	S=0	-10746.65252336	0.09672389	21228.45
	S=1	-10746.72723528	0.02201197	4831.07
	S=2	-10746.71802825	0.03121900	6851.78
	S=3	-10746.74924725	0.00000000	0.00
	S=4	-10746.71739699	0.03185026	6990.33
	S=5	-10746.71514511	0.03410214	7484.56
	S=6	-10746.73409643	0.01515082	3325.22
PBE	S=0	-10743.44729349	0.00156212	342.84
	S=1	-10743.44684147	0.00201414	442.05
	S=2	-10743.43273256	0.01612306	3538.60
	S=3	-10743.44885561	0.00000000	0.00
	S=4	-10743.42996346	0.01889215	4146.35
	S=5	-10743.42465877	0.02419684	5310.60
	S=6	-10743.42479705	0.02405856	5280.24
TPSS0	S=0	-10749.17882817	0.14562564	31961.14
	S=1	-10749.29502766	0.02942615	6458.30
	S=2	-10749.28663330	0.03782051	8300.64
	S=3	-10749.32445381	0.00000000	0.00
	S=4	-10749.28652937	0.03792444	8323.45
	S=5	-10749.28582477	0.03862904	8478.10
	S=6	-10749.31216783	0.01228598	2696.46
wB97	S=0	-10749.13281755	0.12510769	27457.97
	S=1	-10749.16461199	0.09331324	20479.90
	S=2	-10749.13602955	0.12189569	26753.02
	S=3	-10749.25792524	0.00000000	0.00
	S=4	-10749.22413046	0.03379478	7417.10
	S=5	-10749.22210537	0.03581987	7861.55
	S=6	-10749.24613045	0.01179478	2588.66

The ground state of the **Co<sub>4</sub>** is S = 3, as predicted by all DFT calculations, suggesting a ferrimagnetic interaction between Co sites. Some interactions may be ferromagnetic, while others may be antiferromagnetic.

**Table S25.** Löwdin charge and spin population analysis on main atoms, B3LYP, S = 3, **Co<sub>4</sub>-R0**.

Atom	Charge	Spin
Co	0.232219	2.625235
Co	0.232199	2.625218
Co	0.232206	2.625218
Co	-0.134245	-2.313186
O	-0.436451	0.170882
Cl	-0.258600	0.088894
Cl	-0.258609	0.088890
Cl	-0.258595	0.088880
P	0.432571	-0.036839
P	0.432586	-0.036827
P	0.432548	-0.036812
N	-0.073527	0.035450
N	-0.073533	0.035442
N	-0.073525	0.035437

The Mulliken and Loewdin spin population analyses predict about 2.6 unpaired electrons on the Co atoms. It suggests Co(II) and a 3d<sup>7</sup> high-spin configuration (S = 3/2) on each Co(II) atom.

**Table S26.** Ground state total energy for different spin multiplicities (a.u.) for central Co<sub>2</sub> site, using **Co<sub>1</sub>Zn<sub>3</sub>-R0** equivalents of Co<sub>4</sub> molecule.

DFT	Spin	Absolute Energy (a.u.)	Relative Energy (a.u.)	Relative Energy (cm <sup>-1</sup> )
B3LYP	S=1/2	-11936.32057	0.02771359	6082.43

	S=3/2	-11936.34828	0.00000000	0.00
PBE	S=1/2	-11932.90803	0.01852608	4066.01
	S=3/2	-11932.92655	0.00000000	0.00
TPSS0	S=1/2	-11938.83483	0.03671464	8057.94
	S=3/2	-11938.87154	0.00000000	0.00
wB97	S=1/2	-11939.01693	0.03005469	6596.25
	S=3/2	-11939.04699	0.00000000	0.00

**Table S27.** Ground state total energy for different spin multiplicities (a.u.) for side Co1, Co3, and Co4 sites (Co1 = Co3 = Co4 equivalent, due to C<sub>3</sub> symmetry), using **Co<sub>1</sub>Zn<sub>3</sub>-R0** equivalents of Co<sub>4</sub> molecule).

DFT	Spin	Absolute Energy (a.u.)	Relative Energy (a.u.)	Relative Energy (cm <sup>-1</sup> )
B3LYP	S=1/2	-11936.29869	0.03354937	7363.24
	S=3/2	-11936.33224	0.00000000	0.00
PBE	S=1/2	-11932.86996	0.02488929	5462.57
	S=3/2	-11932.89485	0.00000000	0.00
TPSS0	S=1/2	-11938.82203	0.03957435	8685.57
	S=3/2	-11938.86161	0.00000000	0.00
wB97	S=1/2	-11938.99791	0.03435070	7539.11
	S=3/2	-11939.03226	0.00000000	0.00

On-site DFT calculations reveal the 3d<sup>7</sup> high-spin configuration (S = 3/2) on each Co(II) atom.

All magnetic interactions in **3a** were computed to be FM, J<sub>1</sub> = 2.27 and J<sub>2</sub> = 1.36 cm<sup>-1</sup>. The deviation could be explained as illustrated by in Fe<sub>4</sub>S<sub>4</sub> cluster with Fe-Fe distance of ~2.7 Å.<sup>18</sup> We computed separately the Co1 (side) and Co2 (central) of 3a employing *ab initio* calculations. The three side Co are identical, and have significant ZFS. The central Co2 site, has little ZFS, very close to isotropic S = 3/2. At CASSCF+SOC the splitting of the ground S = 3/2 is about 76 cm<sup>-1</sup>, while it gets reduced at CASPT2+SOC level of theory, about 41 cm<sup>-1</sup>. 3a does show slow relaxation of magnetization (see ESI).

A cationic planar delocalized mixed valence  $\text{Co}_4$  cation having  $S = 9/2$  exhibiting single molecular magnet (SMM) behavior, and its charge-neutral analogue with  $S = 4$  ground state showing spin cross over behavior were previously isolated and characterized by magnetic susceptibility measurements.<sup>19-20</sup>

### Hirshfeld surfaces and fingerprint plots to explore Co-Co interactions

Hirshfeld surface analysis was performed in order to illustrate the different intermolecular interactions. Hirshfeld surfaces and 2D fingerprint plots were calculated with the CrystalExplorer 17.5 program.<sup>21</sup>

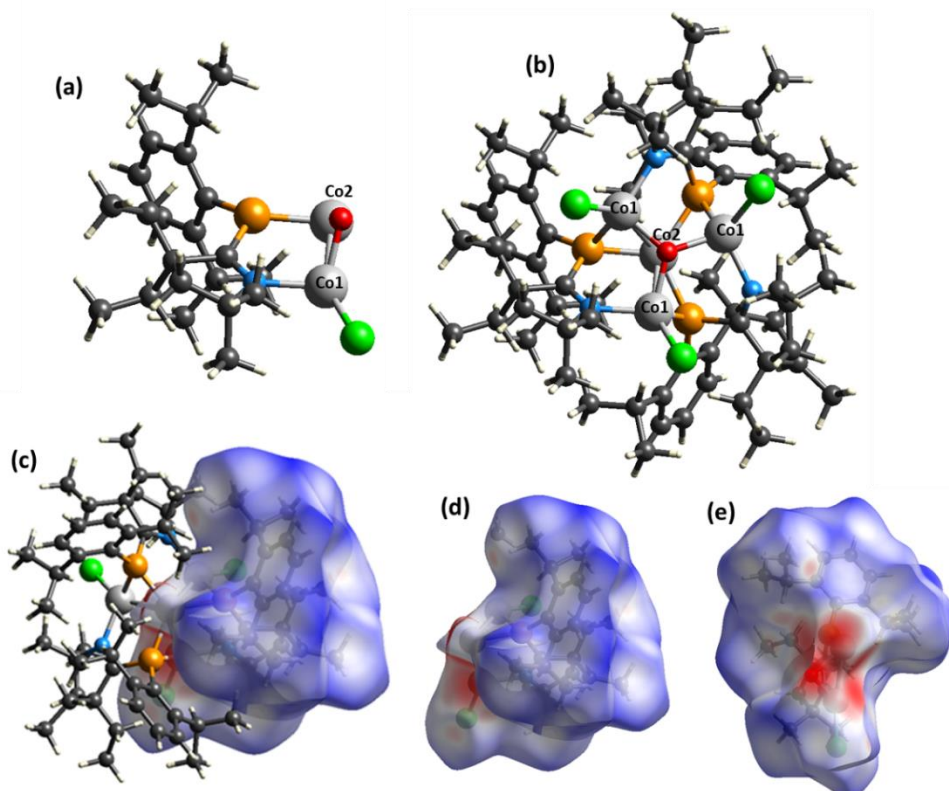


**Figure S44.** (a) Smallest asymmetric fragment of the molecule. (b) Complete structure of the complex – having threefold symmetry. (c) Hirshfeld surface is generated around the smallest asymmetric unit. (d) The external molecular parts of the complex are omitted for better visualization. (e) The red region is having more interaction with the O and other Co atoms. Rotated in a different angle for better visualization.

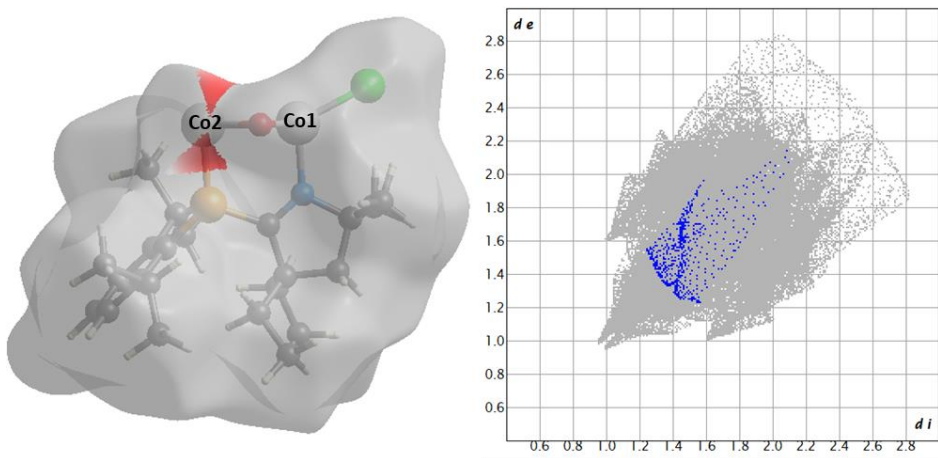


**Figure S45.** Hirshfeld surface of the asymmetric unit of the complex (left) and the fingerprint plot (right) of the Co–Co interaction is represented. The Co1 atom is having no interaction with the Co atom with the neighbouring asymmetric unit. Meanwhile, Co2 is sharing bonds with the next two asymmetric units being at the center of the complex – it is proved by the red coloured region around Co2. 0.5% of the surface area of the Hirshfeld surface is covered in this Co–Co interaction.

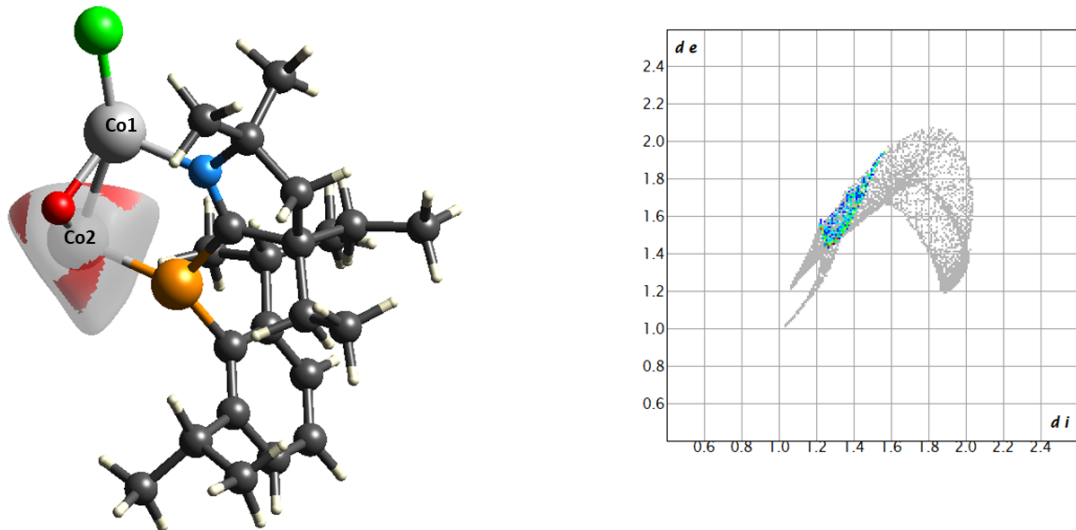


**Figure S46.** Hirshfeld surface (left) is generated around Co2. It is showing red patches having three-fold symmetry which is indicative of this Co atom being at the center position of the complex and forming bond with the other two asymmetric units' Co atoms. Fingerprint plot (right) is showing 7.8% of the surface area of the Hirshfeld surface around Co2 atom is dedicated for the Co–Co interaction.

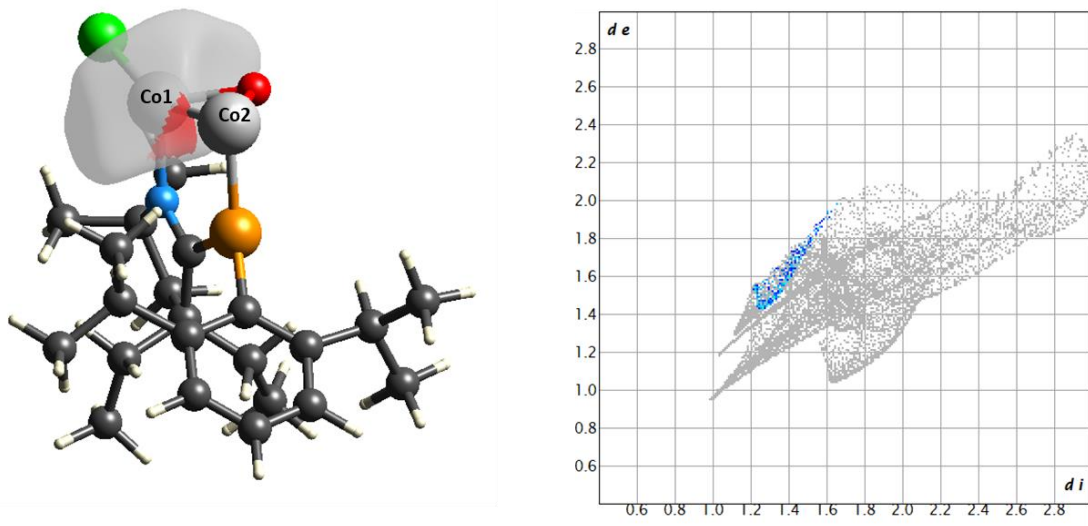


**Figure S47.** Hirshfeld surface (left) is generated around Co1. It is showing red region which is indicative of this Co1 atom forming bond with the central Co2 atom. Fingerprint plot (right) is showing 2.3% of the surface area of the Hirshfeld surface around Co1 atom is utilized for the Co–Co interaction.

## S7. X-ray photoelectron spectroscopy (XPS) data

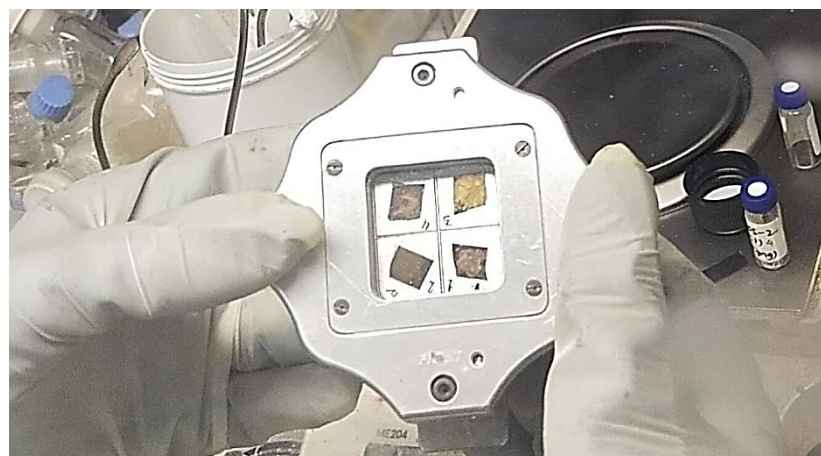


**Figure S48.** Sample preparation for the XPS studies.

### S7.1. XPS data of $\text{[((Dipp)(Et}_2\text{-cAl)}\text{P}(\text{CoCl}))_3\text{CoO}]$ (3a)

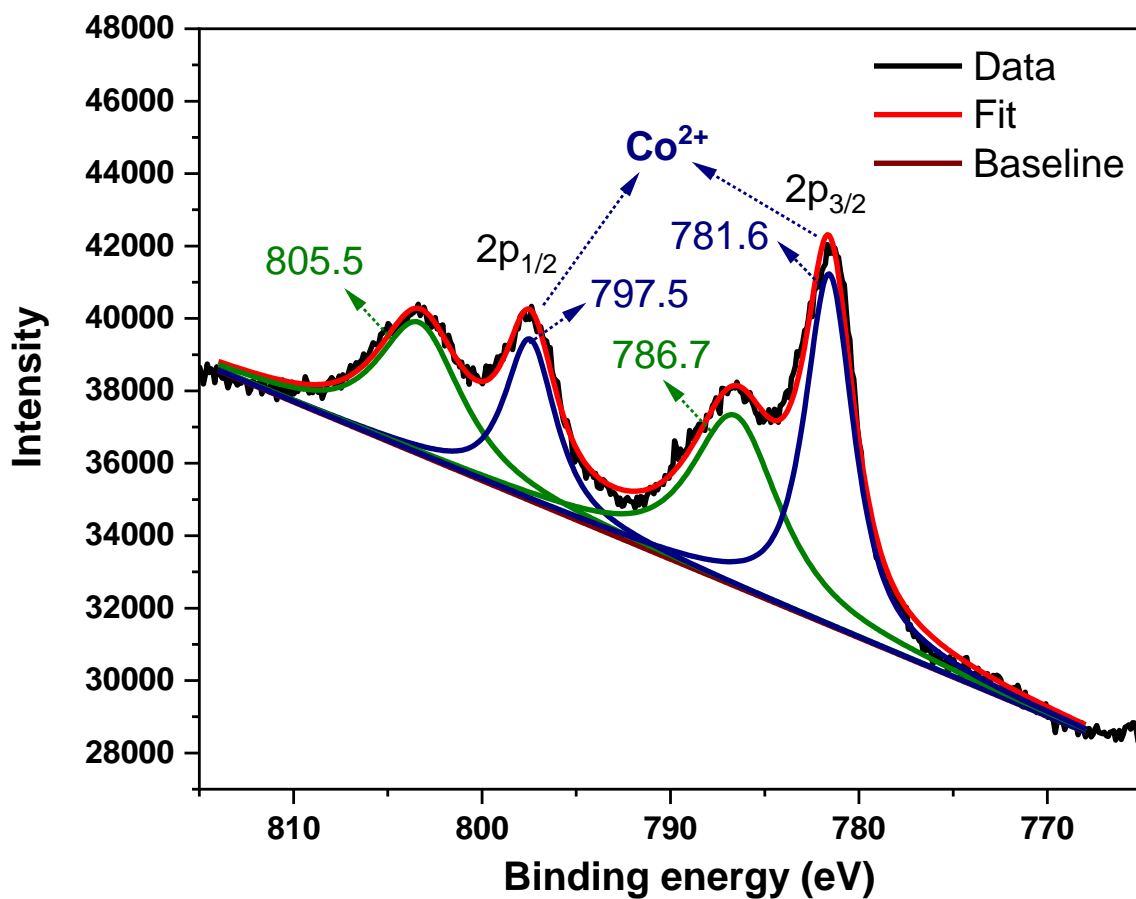


**Figure S49.** Co2p high-depth deconvolution spectra of **3b**.

The high-resolution XPS spectrum of  $\text{[((Dipp)(Et}_2\text{-cAl)}\text{P}(\text{CoCl}))_3\text{CoO}]$  (**3a**) revealed two doublets for the Co 2p region with the 2p<sub>1/2</sub>, and 2p<sub>3/2</sub> components, separated by ~16 eV. The Co 2p<sub>3/2</sub> spectrum features a primary peak at 781.6 eV with a satellite peak at 786.7 eV. The peak at the binding energy 805.5 eV is the satellite peak of 797.5 eV, which corresponds to the Co 2p<sub>1/2</sub> window.<sup>22-25</sup>

## S8. Spectral data

### NMR spectral data of 2a, 2b

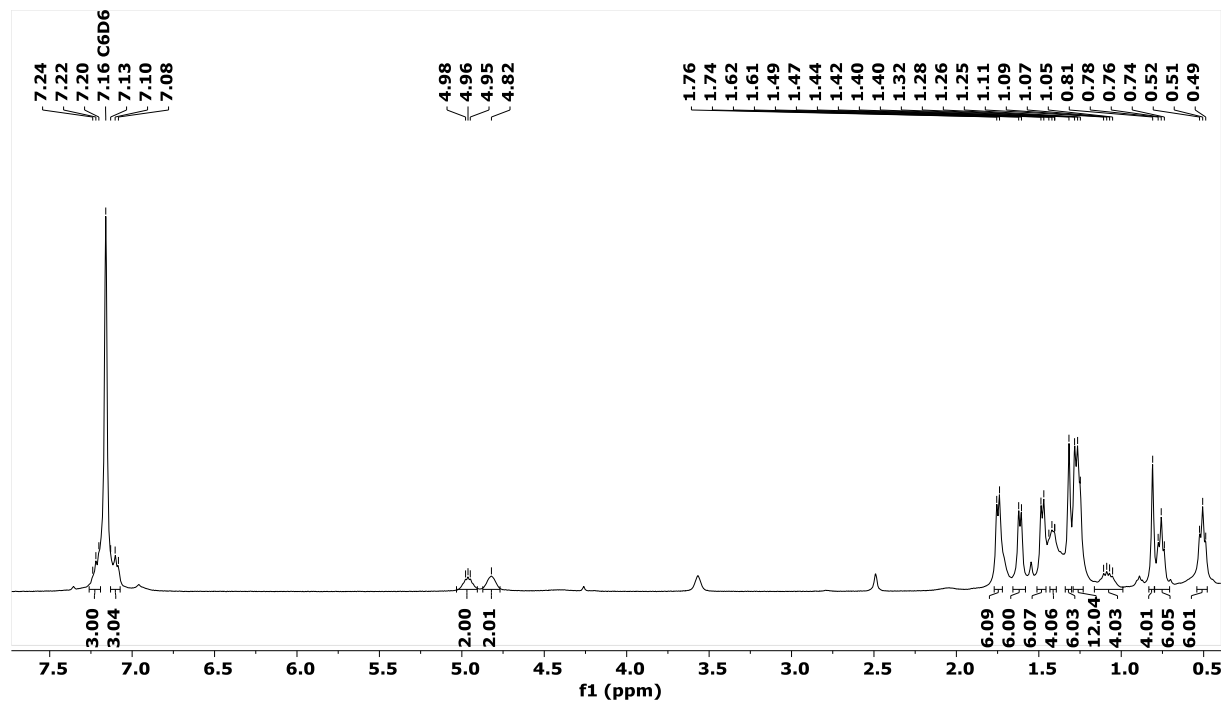


**Figure S50.** <sup>1</sup>H NMR spectrum of compound 2a (400 MHz, C<sub>6</sub>D<sub>6</sub>, 298 K).

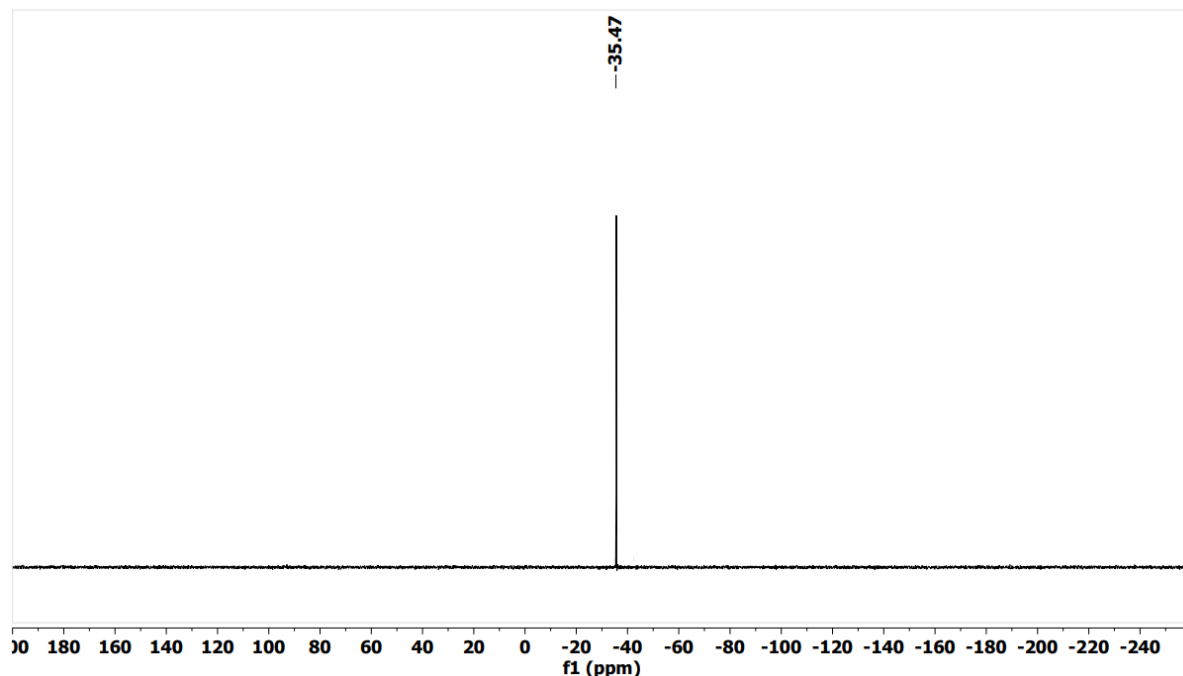


**Figure S51.** <sup>31</sup>P NMR spectrum of compound 2a (162 MHz, C<sub>6</sub>D<sub>6</sub>, 298 K).

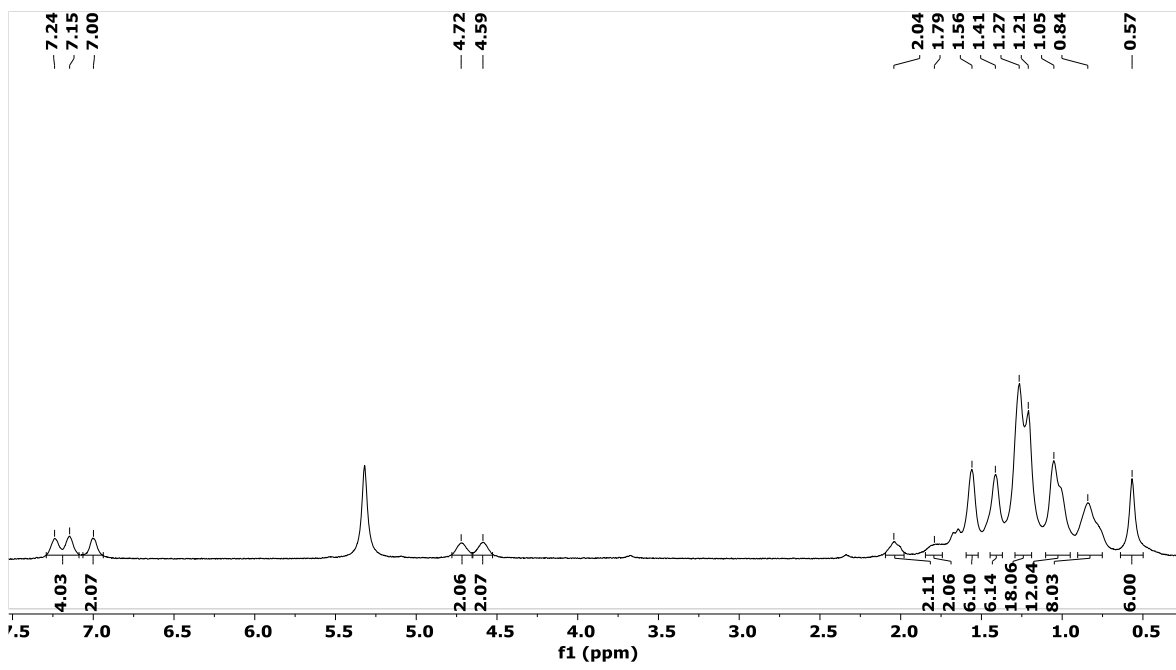


**Figure S52.** <sup>1</sup>H NMR spectrum of compound **2b** (400 MHz, CD<sub>2</sub>Cl<sub>2</sub>, 298 K).

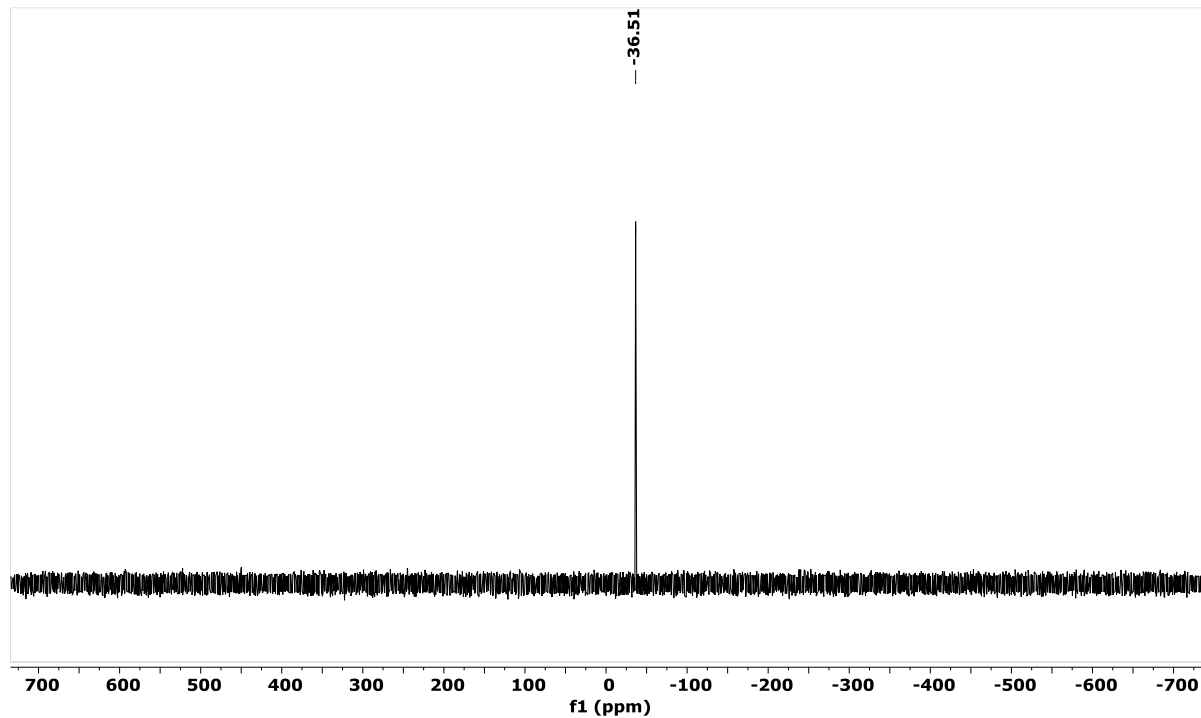


**Figure S53.** <sup>31</sup>P NMR spectrum of compound **2b** (162 MHz, CD<sub>2</sub>Cl<sub>2</sub>, 298 K).

## S9. References

1. V. Lavallo, Y. Canac, C. Präsang, B. Donnadieu and G. Bertrand, *Angew. Chem. Int. Ed.*, 2005, **44**, 5705-5709.
2. S. Roy, K. C. Mondal, S. Kundu, B. Li, C. J. Schürmann, S. Dutta, D. Koley, R. Herbst-Irmer, D. Stalke and H. W. Roesky, *Chem. Eur. J.*, 2017, **23**, 12153-12157.
3. E. Nag, M. Francis, D. Putta and S. Roy, *Chem. Eur. J.*, 2023, **29**, e202302120.
4. Bruker (2021). APEX4, SAINT and SADABS. Bruker AXS Inc., Madison, Wisconsin, USA.
5. G. M. Sheldrick, *Acta Cryst.*, 2015, **71**, 3-8.
6. C. B. Hübschle, G. M. Sheldrick and B. Dittrich, *J. Appl. Cryst.*, 2011, **44**, 1281-1284.
7. Dolomanov, Oleg V, Bourhis, Luc J, R. J. Gildea, H. Judith and H. Puschmann, *J. Appl. Cryst.*, 2009, **42**, 339-341.
8. L. J. Farrugia, *J. Appl. Cryst.*, 2012, **45**, 849-854.
9. Y. Wang, Y. Xie, M. Y. Abraham, R. J. Jr, P. Wei, H. F. III, Paul and G. H. Robinson, *Organometallics*, 2010, **29**, 4778-4780.
10. Y. Wang, Y. Xie, P. Wei, K. R. Bruce, H. F. III, Paul and G. H. Robinson, *J. Am. Chem. Soc.*, 2008, **130**, 14970-14971.
11. J. Abbenseth, F. Wätjen, M. Finger and S. Schneider, *Angew. Chem. Int. Ed.*, 2020, **59**, 23574-23578.
12. (a) C. Lee, W. Yang and R. G. Parr, *Phys. Rev. B*, 1988, **37**, 785-789; (b) A. D. Becke, *J. Chem. Phys.*, 1993, **98**, 5648-5652; (c) P. J. Stephens, F. J. Devlin, C. F. Chabalowski and M. J. Frisch, *J. Phys. Chem.*, 1994, **98**, 11623-11627.
13. (a) A. E. Reed, L. A. Curtiss and F. Weinhold, *Chem. Rev.*, 1988, **88**, 899-926; (b) A. E. Reed, R. B. Weinstock and F. Weinhold, *J. Chem. Phys.*, 1985, **83**, 735-746; (c) K. B. Wiberg, *Tetrahedron*, 1968, **24**, 1083-1096.
14. Gaussian 09, Revision A.02, M. J. Frisch, G. W. Trucks, H. B. Schlegel, G. E. Scuseria, M. A. Robb, J. R. Cheeseman, G. Scalmani, V. Barone, G. A. Petersson, H. Nakatsuji, X. Li, M. Caricato, A. Marenich, J. Bloino, B. G. Janesko, R. Gomperts, B. Mennucci, H. P. Hratchian, J. V. Ortiz, A. F. Izmaylov, J. L. Sonnenberg, D. Williams-Young, F. Ding, F. Lipparini, F. Egidi, J. Goings, B. Peng, A. Petrone, T. Henderson, D. Ranasinghe, V. G. Zakrzewski, J. Gao,

- N. Rega, G. Zheng, W. Liang, M. Hada, M. Ehara, K. Toyota, R. Fukuda, J. Hasegawa, M. Ishida, T. Nakajima, Y. Honda, O. Kitao, H. Nakai, T. Vreven, K. Throssell, J. A. Montgomery, Jr., J. E. Peralta, F. Ogliaro, M. Bearpark, J. J. Heyd, E. Brothers, K. N. Kudin, V. N. Staroverov, T. Keith, R. Kobayashi, J. Normand, K. Raghavachari, A. Rendell, J. C. Burant, S. S. Iyengar, J. Tomasi, M. Cossi, J. M. Millam, M. Klene, C. Adamo, R. Cammi, J. W. Ochterski, R. L. Martin, K. Morokuma, O. Farkas, J. B. Foresman, and D. J. Fox, Gaussian, Inc., Wallingford CT, 2016.
15. O. Back, G. Kuchenbeiser, B. Donnadieu and G. Bertrand, *Angew. Chem. Int. Ed.*, 2009, **48**, 5530-5533.
16. M. Albrecht, P. Maji, C. Häusl, A. Monney and H. MüllerBunz, *Inorg. Chim. Acta.*, 2012, **380**, 90-95.
17. (a) R. F. W. Bader, Clarendon Pr, Oxford, 1990; (b) R. F. W. Bader, *Chem. Rev.*, 1991, **91**, 893-928; (c) R. F. W. Bader, *Acc. Chem. Res.*, 1985, **18**, 9-15; (d) C. F. Matta and R. J. Boyd, Wiley-Vch, Weinheim, 2007; (e) AIMAll (Version 10.05.04), T. A. Keith, TK Gristmill Software, Overland Park KS, USA, 2019.
18. L. Deng, E. Bill, K. Wieghardt and R. H. Holm, *J. Am. Chem. Soc.*, 2009, **131**, 11213.
19. C. Mejuto-Zaera, D. Tzeli, D. Williams-Young, N. M. Tubman, M. Matoušek, J. Brabec, L. Veis, S. S. Xantheas, and W. A. de Jong, *J. Chem. Theory Comput.*, 2022, **18**, 687.
20. K. García-Díez, J. Fernández-Fernández, J. A. Alonso and M. J. López, *Phys. Chem. Chem. Phys.*, 2018, **20**, 21163.
21. P. R. Spackman, M. J. Turner, J. J. McKinnon, S. K. Wolff, D. J. Grimwood, D. Jayatilaka and M. A. Spackman, *J. Appl. Crystallogr.*, 2021, **54**, 1006-1011.
22. R. Benbalagh, F. Rochet, A. Moisset, A. Sodreau, C. Bories, C. Salzemann, C. Petit and M. Petit, *J. Phys. Chem. C*, 2024, **128**, 3408-3422.
23. B. Pradhan, G. S. Kumar, A. Dalui, A. H. Khan, B. Satpati, Q. Ji, L. K. Shrestha, K. Ariga and S. Acharya, *J. Mater. Chem. C*, 2016, **4**, 4967-4977.
24. S. Cobo, J. Heidkamp, P. Jacques, J. Fize, V. Fourmond, L. Guetaz, B. Jousselme, V. Ivanova, H. Dau, S. Palacin, M. Fontecave and V. Artero, *Nat. Mater.*, 2012, **11**, 802-807.
25. Z. Huang, Z. Chen, Z. Chen, C. Lv, M. G. Humphrey and C. Zhang, *Nano Energy*, 2014, **9**, 373-382.